Computer-aided Detection of Malaria Parasites

Luís Filipe Caeiro Margalho Guerra Rosado

U.PORTO

FEUP FACULDADE DE ENGENHARIA
UNIVERSIDADE DO PORTO

Computer-aided Detection of Malaria Parasites

Luís Filipe Caeiro Margalho Guerra Rosado

Programa Doutoral em Engenharia Biomédica

November 9, 2018

Abstract

Malaria is a leading cause of death and disease in many developing countries, where young children and pregnant women are the most affected groups. In 2016, there were an estimated 216 million cases of malaria in 91 countries, which caused approximately 445 000 deaths. Around 90% of those cases occurred in Africa, where the lack of access to malaria diagnosis is largely due to shortage of expertise and equipment.

Microscopy examination has been the pillar of malaria diagnosis, being the recommended procedure when its quality can be maintained. However, the need for trained personnel and adequate equipment limits its availability and accessibility in malaria-endemic areas. These drawbacks are closely related with the increasing interest in the development of computer-aided diagnosis systems, particularly distributed solutions that provide access to complex diagnosis in rural areas. Promising advances have been reported in the area of computer-aided detection of malaria parasites during the past few years. However, the majority of the proposed approaches in the literature are based on two main requirements unsuitable for most malaria-endemic areas: images acquired under well-controlled conditions and the need of proper microscopic equipment. Both criteria are difficult to accomplish in those areas, where this type of equipment and the know-how to maneuver it are scarce or nonexistent.

The search for suitable alternatives for these scenarios has been the main driving force behind this thesis. Consequently, the objectives of this thesis revolved around making contributions in the field of computer-aided detection of malaria parasites using mobile devices. These contributions were envisioned to be the main building blocks for the development of a mobile-based framework supporting the pre-diagnosis of malaria in medically-underserved areas, being simultaneously low cost and easy to use, even for non-experts in microscopy. To achieve that goal, the development of both hardware and software components were explored.

We started by developing a fully automated 3D-printed smartphone microscope with a motorized stage, termed μSmartScope. The developed prototype allows autonomous acquisition of a pre-defined number of images at 1000x magnification, by using a motorized automated stage fully powered and controlled by a smartphone, without the need of manual focus. In order to validate the prototype as a reliable alternative to conventional microscopy, we evaluated the μSmartScope performance in terms of: resolution; field of view; illumination; motorized stage performance (more specifically the mechanical movement precision/resolution and power consumption); and the proposed automated focus procedure.

Furthermore, we also explored the development of computational approaches for the automated detection of malaria parasites in microscopic blood smear images acquired with the μSmartScope. Particularly, we proposed two different image processing methodologies using supervised classification: i) an approach to detect the presence and count the number of malaria parasites in thick blood smears; and ii) an approach to determine the species and life cycle stage of malaria parasites in thin blood smears. The promising results achieved by both methodologies attested the potential of using these approaches as a valid alternative to conventional microscopy examination.

The work presented throughout this thesis clearly demonstrates the potential of using a mobile-based framework to support the pre-diagnosis of malaria, specially in areas with limited access to healthcare services. In addition, new research topics emerged from the conducted work, namely the development of similar frameworks that support the diagnosis of other neglected tropical diseases, such as lymphatic filariasis or Chagas' disease.

Resumo

A malária é uma das principais causas de morte e doença em muitos países em desenvolvimento, onde os grupos mais afetados são crianças pequenas e mulheres grávidas. Em 2016 foram estimados um total de 216 milhões de casos de malária em 91 países, o que provocou aproximadamente 445 000 mortes. Cerca de 90% desses casos ocorreram em África, onde a falta de acesso ao diagnóstico de malária deve-se em grande parte à falta de pessoal especializado e equipamentos.

O exame microscópico tem sido o pilar do diagnóstico de malária, sendo o procedimento recomendado quando sua qualidade pode ser mantida. No entanto, a necessidade de pessoal treinado e equipamento adequado limita a sua disponibilidade e acessibilidade nas áreas endémicas de malária. Essas desvantagens estão intimamente relacionadas com o crescente interesse pelo desenvolvimento de sistemas de diagnóstico assistidos por computador, particularmente soluções distribuídas que fornecem acesso a diagnósticos complexos em áreas rurais. Avanços promissores foram reportados na área de detecção assistida por computador de parasitas da malária nos últimos anos. No entanto, a maioria das abordagens propostas na literatura baseiam-se em dois requisitos que se mostram inadequados para a maioria das áreas endémicas de malária: imagens adquiridas em condições bem controladas e a necessidade de equipamento microscópico apropriado. Assegurar estes critérios na maioria destas regiões torna-se de facto extremamente complicado, dado os condicionalismos respeitantes ao acesso a equipamento necessário e/ou recursos humanos diferenciados.

A busca de alternativas adequadas para esses cenários foi a principal força motriz por detrás desta tese. Consequentemente, os objetivos desta tese concentraram-se em contribuições no campo da detecção assistida por computador de parasitas da malária usando dispositivos móveis. Essas contribuições constituem os componentes principais para o desenvolvimento de uma framework móvel de suporte ao pré-diagnóstico da malária em áreas carenciadas, sendo simultaneamente de baixo custo e fácil de usar, mesmo para utilizadores não especialistas em microscopia. Para alcançar esse objetivo, foi explorado o desenvolvimento tanto de componentes de hardware como de software.

Começámos por desenvolver um microscópio adaptável a smartphones produzido através de impressão 3D (apelidado de μSmartScope), o qual é automatizado através de uma plataforma motorizada. O protótipo desenvolvido permite a aquisição autónoma de um número pré-definido de imagens com ampliação de 1000x, usando uma plataforma automática motorizada que é totalmente alimentada e controlada por um smartphone, sem a necessidade de foco manual. Para validar o protótipo como uma alternativa viável ao microscópio convencional, avaliámos o desempenho do μSmartScope em termos de: resolução; campo de visão; iluminação; desempenho da plataforma motorizada (mais especificamente a precisão/resolução do movimento mecânico e o consumo de energia); e a abordagem de focagem automática proposta.

Além disso, também explorámos o desenvolvimento de abordagens computacionais para a detecção automatizada de parasitas de malária em imagens microscópicas de amostras de sangue adquiridas através do μSmartScope. Em particular, propusémos duas metodologias de processamento de imagem diferentes usando classificação supervisionada: i) uma abordagem para detectar

a presença e contar o número de parasitas de malária em lâminas de gota espessa de sangue; e ii) uma abordagem para determinar as espécies e os estágio de desenvolvimento de parasitas da malária em lâminas de esfregaço de sangue. Os resultados promissores alcançados em ambas as metodologias atestam o potencial de usar essas abordagens como uma alternativa válida ao exame de microscopia convencional.

O trabalho apresentado ao longo desta tese evidencia claramente o potencial de usar uma framework baseada em dispositivos móveis que visa apoiar o pré-diagnóstico da malária, especialmente em áreas com acesso limitado aos serviços de saúde. Além disso, novos tópicos de pesquisa emergiram a partir do trabalho realizado, nomeadamente o desenvolvimento de frameworks semelhantes que apoiem o diagnóstico de outras doenças tropicais neglicenciadas, tais como a filariose linfática ou a doença de Chagas.

Palavras-chave: Malária, Diagnóstico assistido por computador, Processamento e análise de imagem, Aprendizagem computacional, Microscopia, Dispositivos móveis.

Acknowledgements

Finally, I dedicate this thesis to my parents, Joaquim and Margarida, to my sister Célia, and to the love of my life Dora. You are the most important persons in my life and I owe you everything, so I thank you from the bottom of my heart for all your support and patience during this journey.

Luís Rosado

" Scientific knowledge is hard to take, because it removes the reassuring crutches of opinion, ideology, and leaves only what is demonstrably true about the world. And the reason why so many people may be thinking about throwing away those crutches is because, thanks to science and technology, they have begun to know that they don't know so much."

James Burke

Contents

List of Figures

List of Tables

Abbreviations

AC	Accuracy
AGNES	Absence of Gradients and Nernstian Equilibrium Stripping
AI	Artificial Intelligence
ARR	Annular Ring Ratio
AUC	Area under the curve
BFL	Back-Focal Length
CAD	Computer-aided diagnosis
CHT	Circle Hough Transform
CIE	Commission International de l'Élairage
FFF	Fused Filament Fabrication
FOV	Field-of-view
F_1	F_1 score
fps	frames per second
GLMSR	General Linear Model Simple Regression
HSI	Hue, saturation, intensity
INF	Informedness
IQFT	Inverse Quaternion Fourier transform
kNN	K-nearest neighbors
L*a*b*	Lightness, green/red coordinate, blue/yellow coordinate
L*C*h°	Lightness, chroma, hue
mHealth	Mobile health
MPs	Malaria parasites
NN	Neural Networks
NTDs	Neglected tropical diseases
PCA	Principal Component Analysis
QFT	Quaternion Fourier Transform
RBCs	Red blood cells
RDTs	Rapid diagnostic tests
RGB	Red, green, blue
ROC	Receiver operating characteristic
ROI	Region of interest
SE	Sensitivity
SP	Specificity
SVM	Support vector machines
WBCs	White blood cells
WHO	World Health Organization

Part I

Introduction and Theoretical Background

Chapter 1

Introduction

Between 2010 and 2015, malaria mortality rates dropped by an estimated 29% globally and by 31% in the African region due to the scale-up of malaria interventions. Despite this remarkable progress, the global tally of malaria in 2015 was still 212 million new cases and 429,000 deaths, with an estimation that malaria surveillance systems only detected 19% of the cases occurred globally. Most of these deaths occurred in the African region (92%), but it is estimated that nearly half of the world's population is at risk of malaria. This disease is considered endemic in 91 countries [74], and across Africa millions of people still lack access to the tools they need to properly prevent and treat it. Prompt diagnosis can not only prevent the development of severe malaria, but also reduce the length of time that patients carry malaria parasites (MPs) in their blood, which in turn reduces the risk of onward transmission [74].

Since 2010, WHO has recommended that all persons with suspected malaria should undergo malaria diagnostic testing, by either microscopy or rapid diagnostic tests (RDTs). Microscopy examination consists of preparing a blood smear, staining it (most often with Giemsa stain) and examining it through a microscope. This process remains the mainstay of malaria diagnosis in most large health clinics and hospitals. However, microscopy-based diagnosis in rural areas is frequently non-existent or inadequate in terms of quality due to scarce resources (equipment and trained staff). When stained MPs are spotted by the microscopist, the diagnosis of malaria is confirmed by identifying the respective stage, species and infection density [71]. Microscopic examination can be made through the usage of thin and thick blood smears. While the thin smear consists of a single layer of red blood cells (RBCs), the thick smear is 6 to 20 times thicker, allowing for a greater volume of blood to be examined. Thus, thick smears are firstly used to check the presence of MPs, while thin smears are subsequently analyzed for the identification of MP species. The conventional flow for thick and thin blood smear analysis using manual microscopy examination is presented in Figure 1.1.

Malaria diagnosis through RDTs is accomplished by detecting specific malaria antigens in a person's blood. However, the use of the RDT does not eliminate the need for malaria microscopy for two main factors: (i) the RDT may not be able to detect some infections with low parasite density; (ii) the currently approved RDT in the U.S. only detects two different malaria antigens
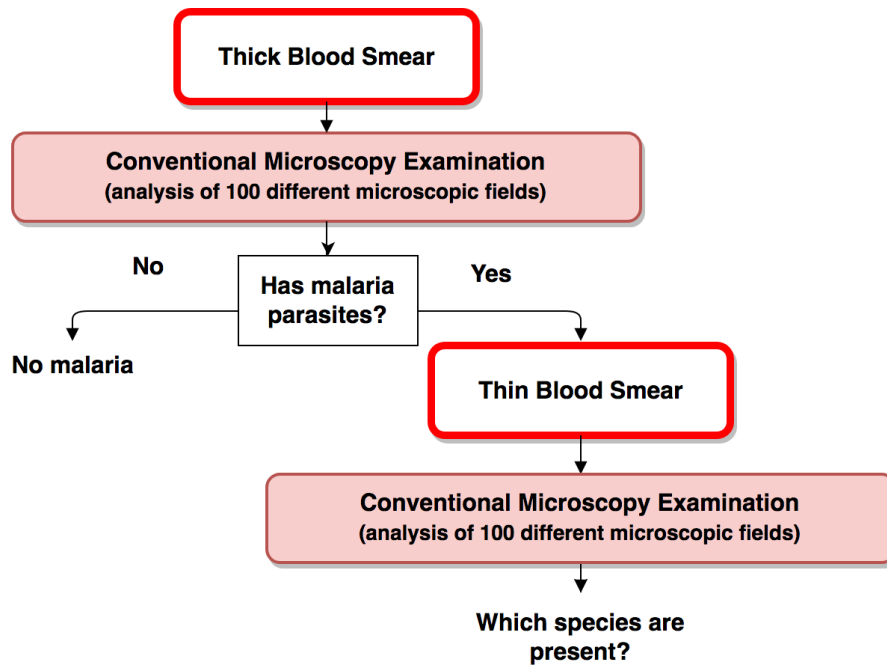
Figure 1.1: Conventional flow for thick and thin blood smear analysis using manual microscopy examination.

(one is specific for *P. falciparum*, and the other is found in all four human species of malaria). Thus, microscopy is further needed to determine the parasite species and to quantify the proportion of RBCs that are infected, which is an important prognostic indicator [10].

1.1   Motivation

A recent report [73] considers that current funding distribution on malaria control commodities (US $1.6 billion in 2014) is not addressing the fundamental weaknesses in health systems of developing countries, suggesting that innovative ways may be required to rapidly expand access to malaria interventions. It is worth underlining that the mobile phone is currently Africa's most important digital technology [6], and just as African telecommunications largely skipped over landline infrastructure and went straight to mobile phones, some experts say African medicine can skip over centralized labs [16]. Moreover, the combination of mobile devices with image processing and artificial intelligence for malaria diagnosis can bring several advantages, like potentially reducing the dependence of manual microscopic examination, which is an exhaustive and time-consuming activity that requires considerable expertise of the laboratory technician.

The development of new microscopic devices, ideally portable and low cost, is also an area that can greatly improve the chances of the successful deployment of computer-aided diagnosis solutions for malaria diagnosis in the field. Considering the high customs taxes and import duties currently in practice in most of the African countries, the easy replicability of these microscopy devices in developing countries is a topic that should also be taken into account. Other requirements

for this type of microscopic devices were equally considered since the beginning of this work, like: i) automating the device as much as possible, thus discarding the need of considerable expertise and train of the technician in terms of maneuvering the microscope; or ii) supplying the energy needed for the illumination and/or any type of automation through the mobile device battery, thus discarding the need of an additional power source.

By achieving and merging some of the described software and hardware innovations, we believe that the lack of highly trained microscopists on malaria diagnosis in rural areas could then be complemented by a significantly less specialized technician that knows how to operate the system and prepare blood smears.

Finally, malaria diagnosis might be just one element of a suite of diagnostic software tests running on this type of system. Several other tests could simultaneously be carried out using the same images, for instance cell counting or detection of other hemoparasites like microfilaria or trypanosoma.

1.2 Objectives

The main driving force behind this thesis has been the search for suitable alternatives to conventional malaria diagnosis through manual microscopy examination. Consequently, the objectives of this thesis revolved around making contributions in the field of computer-aided detection of malaria parasites. To achieve a solution with a realistic chance of being effectively used in the field, we soon realized that we needed to explore the development of both hardware and software components. Conventional microscopes and trained personnel with know-how to maneuver it are often scarce or nonexistent in rural endemic areas, so one of the objectives was to make contributions in the field of cell-phone based systems that provide low-cost alternatives to conventional microscopy.

On the other hand, the lack of trained microscopists that can visually spot malaria parasites on microscopic fields was equally important to address. Thus, another objective was to contribute in the area of computational approaches for the automated detection of malaria parasites in microscopic blood smear images. Particularly, we wanted to address two distinct computer vision challenges for images exclusively acquired with low-cost and accessible tools such as smartphone: i) detection and quantification of malaria parasites in thick blood smears; and ii) the automated species and life cycle stage determination in thin blood smears.

1.3 Contributions

The contributions of this thesis in the field of computer-aided detection of malaria parasites are now summarized:

1. Developed and evaluated a fully automated 3D-printed smartphone microscope with a motorized stage (termed μSmartScope). This prototype was the first proposed smartphone-based alternative to conventional microscopy that allows autonomous acquisition of a pre-defined number of images at 1000x magnification with suitable resolution, by using a

motorized automated stage fully powered and controlled by a smartphone, without any human interaction.

2. Proposed a new automated focus approach that takes advantage of the μSmartScope's motorized automated stage and real time feedback retrieved from the smartphone camera sensor. This methodology was evaluated on different blood smears and smartphone models, which validated that the obtained results were not biased towards a specific specimen type (e.g. amount microscopic structures or staining condition) or specific camera sensor characteristics (e.g. resolution, exposure or white-balancing mode).

3. Proposed a new methodology to detect and count the number of *P.falciparum* trophozoites and WBCs in Giemsa stained thick blood smears. Given the lack of freely available image datasets, a mobile acquired image dataset manually annotated by a specialist was specifically created and used in this study.

4. Proposed a new methodology using supervised classification to analyze microscopic images of malaria-infected thin blood smears. Given the lack of freely available image datasets, a new mobile thin smear malaria parasites (mThinMPs) image database was specifically created to develop and validate this methodology.

5. Proposed a new performance metrics criterion for SVM hyperparameters' selection, which merges the informedness and F_1 score metrics.

The MalariaScope Project

All the contributions described above were achieved in the ambit of the MalariaScope project, a R&D project of Fraunhofer Portugal AICOS that aims to create a mobile-based solution that can provide an effective pre-diagnosis of malaria to be used in medically underserved areas. This project started in the ambit of Fraunhofer Portugal AICOS's ICT for Developing Competence Center, in cooperation with the Research and Development Unit of the Infectious Diseases Department of the Instituto Nacional de Saúde Dr. Ricardo Jorge in Porto, which finished in 2015. Given the encouraging obtained results, these research topics continued to be explored in the ambit of the project "Deus ex Machina: Symbiotic Technology for Societal Efficiency Gains".

1.4   List of Publications

The work conducted in this thesis resulted in the following journal papers:

- Luís Rosado, José M. Correia da Costa, Dirk Elias, and Jaime S. Cardoso. A review of automatic malaria parasites detection and segmentation in microscopic images. *Anti-Infective Agents*, 14(1):11–22, 2016.

- Luís Rosado, José M. Correia da Costa, Dirk Elias, and Jaime S. Cardoso. Mobile-based analysis of malaria-infected thin blood smears: Automated species and life cycle stage determination. *Sensors*, 17(10), 2017.

The following publications in international conferences were also the result of the research work presented throughout this thesis:

- Luís Rosado, José M. Correia da Costa, Dirk Elias, and Jaime S. Cardoso. Automated Detection of Malaria Parasites on Thick Blood Smears via Mobile Devices. *Procedia Computer Science*, 90:138–144, January 2016.

- Luís Rosado, João Oliveira, Maria João M. Vasconcelos, José M. Correia da Costa, Dirk Elias, and Jaime S. Cardoso. μSmartScope: 3d-printed smartphone microscope with motorized automated stage. In *Proceedings of the 10th International Joint Conference on Biomedical Engineering Systems and Technologies - Volume 1: BIODEVICES, (BIOSTEC 2017)*, pages 38–48. INSTICC, SciTePress, 2017.

Furthermore, the developed work also resulted in a book chapter:

- Luís Rosado, Paulo T. Silva, José Faria, João Oliveira, Maria João M. Vasconcelos, José M. Correia da Costa, Dirk Elias, and Jaime S. Cardoso. μSmartScope: Towards a fully automated 3d-printed smartphone microscope with motorized stage. *Communications in Computer and Information Science Book Series*, 881, 2018.

1.5   Document Structure

This thesis is divided into three parts, which comprises a total of six chapters. The document is structured as follow:

The Part I, **Introduction and Theoretical Background**, is composed by two chapters: the current chapter is Chapter 1 and presents the motivations, objectives and main contributions of the thesis; Chapter 2 summarizes the fundamental topics regarding computer-aided detection of malaria parasites, including the literature review.

The Part II, **Methodologies and Results**, is composed by three chapters: Chapter 3 presents the work done in the development and evaluation of a fully automated 3D-printed smartphone microscope with a motorized stage; Chapter 4 focuses on the automated analysis of malaria-infected thick blood smears via mobile devices; Chapter 5 explores new computer vision and machine-learning approaches for the analysis of microscopic images of malaria-infected thin blood smears acquired with mobile devices.

The Part III, **Conclusion**, comprises Chapter 6 where the conclusions and the most relevant topics regarding future work are depicted.

Chapter 2

Fundamentals of Computer-aided Malaria Parasites Detection

A Review of Automatic Malaria Parasites Detection and Segmentation in Microscopic Images

Luís Rosado, José M. Correia da Costa, Dirk Elias and Jaime S. Cardoso

Abstract

Malaria is a leading cause of death and disease in many developing countries, where young children and pregnant women are the most affected groups. In 2012, there were an estimated 207 million cases of malaria, which caused approximately 627 000 malaria deaths. Around 80% of malaria cases occur in Africa, where the lack of access to malaria diagnosis is largely due to a shortage of expertise, being the shortage of equipment the secondary factor. This lack of expertise for malaria diagnosis frequently results on the increase of false positives, since prescription of medication is based only on symptoms. Thus, there is an urgent need of new tools that can facilitate the rapid and easy diagnosis of malaria, especially in areas with limited access to quality healthcare services. The aim of this work is to collect and review image processing and analysis approaches already proposed on the literature for the analysis of malaria infected blood smear images.

Keywords: malaria; computer-aided diagnosis; image analysis; segmentation; feature extraction; classification.

2.1 Introduction

Malaria is one of the most severe public health problems worldwide. It is a leading cause of death and disease in many developing countries, where young children and pregnant women are the groups most affected. In 2012, there were an estimated 207 million cases of malaria, which caused approximately 627 000 deaths. An estimated 3.4 billion people continue to be at risk of malaria, mostly in Africa and south-east Asia.

Around 80% of malaria cases occur in Africa [72]. It is worth taking into account that the number of malaria cases and their geographical distribution are not stable because of several factors, like the increasing prevalence in some areas due to expanding drug resistance; the widespread availability of fake and substandard medicines; global warming and expansion of malaria into favorable areas at higher elevations; and population mobility of different kinds [71].

The increasing interest in the development of computer-aided diagnosis (CAD) systems for malaria diagnosis is closely related with common practical difficulties experienced in under-resourced health facilities of developing countries, such as the excessive workload due to shortage of staff. Image processing approaches are often used in CAD systems to reduce the dependence of manual microscopic examination of blood smears, which is an exhaustive and time consuming activity, simultaneously requiring a considerable expertise of the laboratory technician.

During the last years, several image processing techniques have been proposed for malaria diagnosis using microscopic images, addressing the detection of a wide variety of different malaria parasites, in different growth stages and using images acquired from different types of blood smears. Under the scope of this chapter, various image processing and analysis approaches already proposed on the literature for the detection and segmentation of malaria parasites in blood smear microscopic images were collected and reviewed. This timely review aims to support the increasing interest

in the development of low cost tools that can facilitate the rapid and easy diagnosis of malaria, especially in areas with limited access to quality healthcare services.

This chapter is structured into five sections. Section 2.1 corresponds to Introduction and presents the motivation and objectives of this bibliographic survey. Section 2.2 gives an overview of the malaria disease in terms of parasite stages, species and life cycle stages; Section 2.3 provides an overview about the current malaria diagnosis methodologies, with a focus on the characterization of stained components in thin and thick blood smears; Section 2.4 gives a literature review regarding the analysis of malaria infected blood smears using image processing and analysis; Section 2.5 summarizes and gives a critical appreciation of the review works; Section 2.6 provides the final remarks about the discussed subjects.

2.2 Malaria Disease Characterization

Malaria is caused by a parasite in the blood and can be seen only under a microscope with high magnification. For the visualization of the parasites, a blood film must be made, dried, stained and examined under the microscope. When the microscopist sees stained parasites, the diagnosis of malaria is confirmed by identifying the stage and species of the malaria parasite, as well as the infection density [71].

2.2.1 Malaria Parasites Stages

In the human host, malaria parasites pass through 3 different growth stages that can be detected in the peripheral blood: the trophozoite stage, the schizont stage and the gametocyte stage. Trophozoites are often called the ring stage, being the most commonly seen stage, appear incomplete in thick films, and can vary from small to quite large within the host cell. Usually, trophozoites have one chromatin dot, but two are common for the *P.falciparum* species. The cytoplasm takes different shapes, from a well-defined, fine ring to forms that are irregular or bizarre, sometimes called 'amoeboid' [72]. The schizont stage begins when the trophozoite has reached its full capacity and the parasite starts to divide into daughter cells called merozoites. Several more divisions of the chromatin follow, which mark the growth of the schizont, until there are many chromatin bodies, each with its accompanying cytoplasm. The number of chromatin and merozoite divisions helps to identify the species. These clearly delineated new parasites are now ready to leave the host cell to invade new red blood cells [71]. Gametocytes are round or banana-shaped, depending on the species. The way in which the parasite takes up the stain helps to identify the sex of the parasite in thin films, being difficult to differentiate between male and female in thick films [31].

2.2.2 Malaria Parasites Species

Four species of Plasmodium can infect and be transmitted by humans: the *P.falciparum*, *P.vivax*, *P.ovale* and *P.malariae*. *P.falciparum* is the commonest species in the tropical parts of the world

and can evolve rapidly to severe illness and death if not recognized and treated with effective medicines [71]. It is the species responsible for most cases of severe malaria and death. *P.vivax* is the commonest species in the cooler parts of the tropics, being the largest of the human malaria parasites and the cause of much illness and absenteeism from work and school [71]. *P.ovale* is considered a rare species, but relatively common in West Africa and other parts of the African continent. Because of morphological similarities, *P.ovale* is sometimes mistaken for *P.vivax* by less experienced microscopists [71]. Moreover, the existence of a new genotype for *P.ovale* has been recently hypothesized [58]. *P.malariae* is found worldwide and causes a chronic infection that in some cases can last a lifetime. In some chronically infected patients, *P.malariae* can cause serious complications such as the nephrotic syndrome [9]. As a final note, *P.knowlesi* is a malaria parasite that is found in nature in macaques, and naturally acquired human infections were thought to be extremely rare, however a large focus of human infections was reported in 2004 [55].

2.3 Malaria Diagnosis Characterization

Malaria infection can be suspected based on the patient's symptoms, travel history or physical findings at examination. However, for a definitive diagnosis, laboratory tests must be made to prove the presence of the malaria parasites. The microscopy examination remains the gold standard for laboratory confirmation of malaria, which consists in preparing a blood smear, staining it (most often with the Giemsa stain) and examining it through a microscope [9]. The importance of reliable malaria diagnoses cannot be overstated, since false negatives can be potentially fatal, and false positives increase the drug resistance of the patients, leading consequently to unnecessary economic burden [47]. Laboratory diagnosis of malaria can be made through microscopic examination of two kinds of blood smears, thin and thick, taken most often from a finger prick. Thick blood smears are 20-40 times more sensitive in detecting malaria parasites because the blood is more concentrated, which allows for a greater volume of blood to be examined. The thick smear is approximately 6-20 times as thick as a single layer of red blood cells, which results in a larger volume of blood being examined. However, thick smears are more difficult to read, so thin smears aid in parasite species identification and quantification [9], [47].

2.3.1 Image Characteristics

The images used on the reviewed works can be divided in two different groups according to their characteristics: full view images (FV) and manually cropped sub-images (CS). FV consists on images corresponding to the entire microscopic field of view (see Figures 2.1 and 2.2). CS consists on cropped patches of the FV images, corresponding to regions of interest manually cropped (see Figures 2.3 and 2.4).
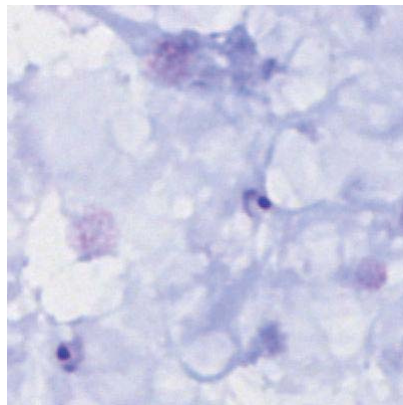
Figure 2.1: Illustrative example of a thick smear full view image (from [17]).
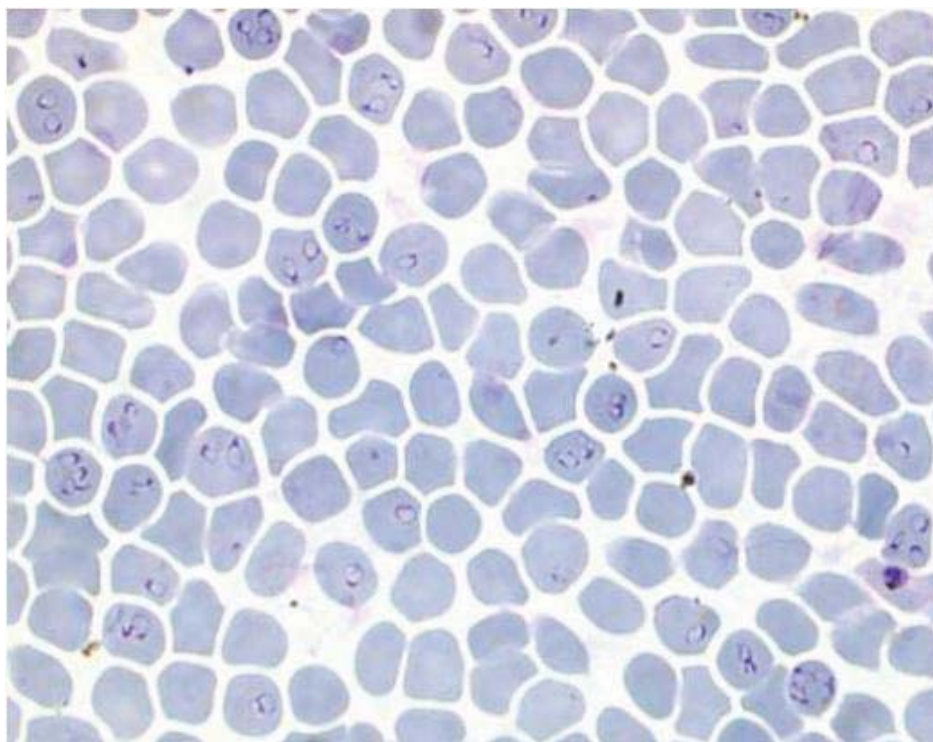
Figure 2.2: Illustrative example of a thin smear full view image (from [60]).

Moreover, the vast majority of the proposed approaches found on literature use high quality equipment in the acquisition process, particularly commercial cameras that are specifically customized for the acquisition of microscopic images, for instance easily attached to microscopes. The exception is [47], which uses a smartphone built-in camera to acquire images (see Figure 2.5).
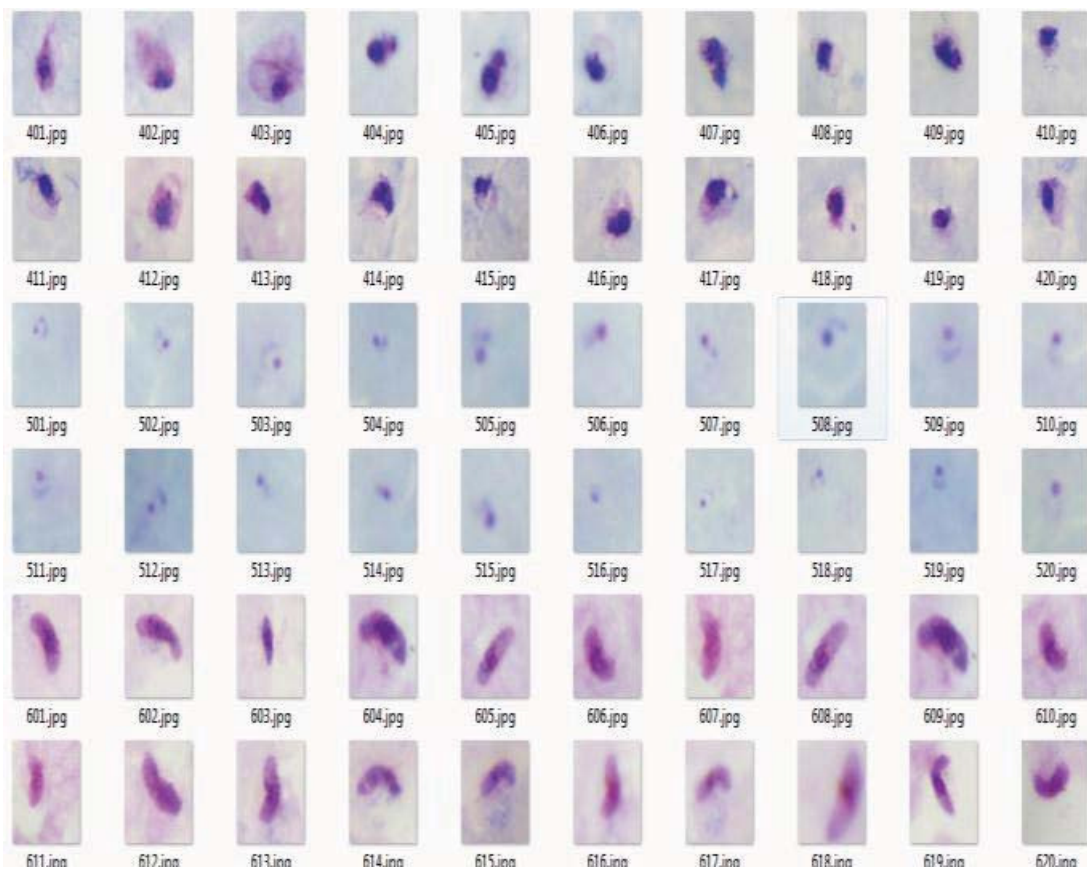
Figure 2.3: Illustrative examples of thick smear cropped sub-images (from [46]).
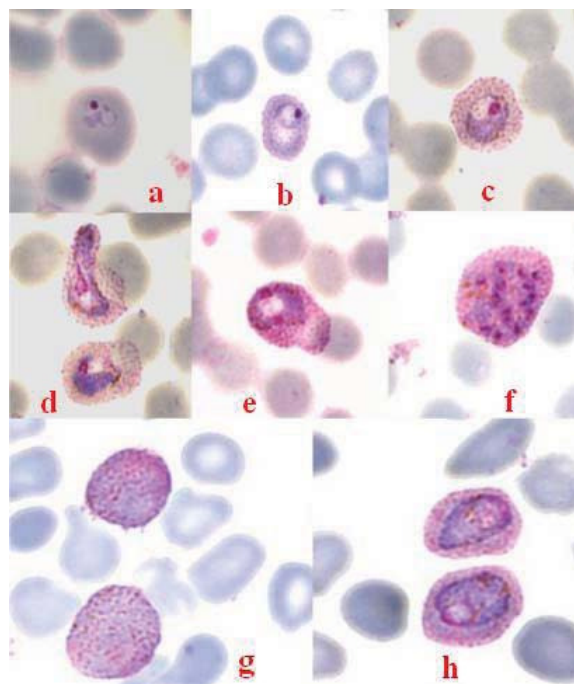
Figure 2.4: Illustrative examples of thin smear cropped sub-images (from [39]).
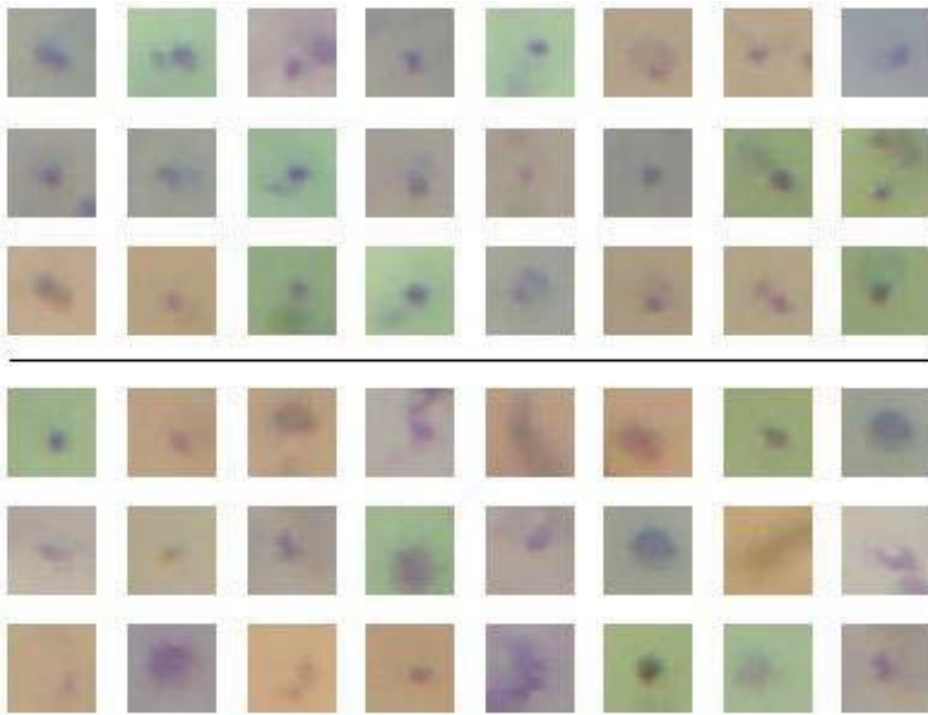
Figure 2.5: Illustrative examples of thin smear cropped sub-images acquired with mobile devices, with positive cases at the top and negative cases at the bottom (from [47]).

2.3.2 Performance Metrics

The classification results of the reviewed works are usually presented in terms of two metrics ordinarily used for this purpose: 1) Sensitivity (SE), i.e. the percentage of structures correctly classified as positive cases of malaria parasites; and 2) Specificity (SP), i.e. the percentage of structures correctly classified as negative cases of malaria parasites.

2.4 Literature Review

This section critically reviews the main studies found in the literature regarding the analysis of malaria infected blood smears using image processing and analysis. Since typical approaches usually comprise four different image processing and analysis tasks, the reviewed works were divided into the following sub-sections: 1) Segmentation; 2) Feature Extraction; 3) Feature Selection; and 4) Classification. For each sub-section, the methods proposed to date for malaria parasites (MPs) stained components analysis, both on thin and thick blood smears, were separately reviewed.

2.4.1 Segmentation

Image segmentation is the process that partitions a digital image into disjoint (non-overlapping) regions, each of which typically corresponds to one object. Once isolated, these objects can be

measured and classified, as discussed in the following sub-sections. This sub-section groups and reviews the methods proposed on the literature for the segmentation of malaria-stained components on thin and thick blood smears.

2.4.1.1 Thresholding

Thresholding is an essential region-based image segmentation technique that is particularly useful for scenes containing solid objects resting on a contrasting background. All pixels at or above/below the threshold are assigned to the foreground and all pixels below/above the threshold are assigned to the background [75].

Thin Blood Films

In [37], the authors suggest a scheme based on HSV color space that segments red blood cells (RBCs) and identifies the RBCs infected with MPs. The RBCs segmentation is achieved by dividing the entire hue range of 360° into six segments and finding the dominant color type to be the representative of the background. Each segment is centered on a color type, which is defined according to the follow degree values: 0° for red; 60° for yellow; 120° for green; 180° for cyan; 240° for blue; and 300° for magenta. The authors state a SE and SP of 83% and 98%, respectively, however this method uses images taken from Leishman-stained blood smears, while the gold standard recommended by WHO for malaria diagnosis is the usage of Giemsa staining. Furthermore, they assume that the dominant color in these images is representative of the background, which might not be true in images highly populated of RBCs (see Figure 2.3).

Another segmentation approach proposed in [31] for RBCs on thin blood smears is based on the Annular Ring Ratio (ARR) transform. This transform consists in obtaining a ratio transformed image by calculating the ratio between the average intensities of a dilated image using annular concentric ring structuring element and an eroded image using a disk shaped structuring element. The ARR transform method mainly aims at locating the center of each cell present in the image. It is worth taking into account that this segmentation methodology uses fixed parameter values defined manually, such as the radius of the annular ring and disk, which can substantially vary depending on the image resolution. The authors in [30] used a modified ARR transform method for the detection of stained cells through the direct application of the ratio transform on grayscale images, eliminating the morphological dilation and erosion. A threshold-based peak detection algorithm is then used to determine the coordinates of each stained component. This approach results in locating all the stained components in the image, with the drawback of picking up artifacts and other noises present in the image.

For blood cells components segmentation in thin smears, [4] uses the Otsu's Method, a well-known histogram shape-based image thresholding routine. This method assumes that the input image has two classes of pixels, and calculates the threshold that minimizes the intra-class variance. A hole filling process in then applied, due to the biconcave nature of the RBCs. Using the knowledge that MPs cytoplasm appear lighter while MPs nucleus appear darker than the cytoplasm of the

RBCs, the authors state that is possible to confirm that it is actually an infected cell by dividing it into 3 different regions (MPs nucleous, MPs cytoplasm and RBCs cytoplasm) using multiple thresholding. However, how this multiple thresholding segmentation is achieved is not explained in the paper, and one should also take into account that possible artifacts could also be separated into 3 different regions.

In [22], *P.vivax* parasites from Leishman-stained thin blood film are segmented using divergence based threshold selection. The proposed modified fuzzy divergence method is based on Cauchy membership function, and applied to the C channel in the CMYK color space, which was the color channel that delivered the best results. However, it is not clear if this approach can be also applied to Giemsa stained thin blood films.

A methodology based on phase spectrum is used in [19] for malaria parasite detection in thin blood films. The method uses the Quaternion Fourier Transform (QFT) to obtain the amplitude spectrum and phase spectrum for blood smear images. Afterward, the reconstructed image is obtained using the Inverse Quaternion Fourier transform (IQFT) on a constant amplitude spectrum and the original phase spectrum. The authors concluded that the most sensitive channels for MPs detection were the B and G channels from the RGB space, as well as the I channel from the HSI space.

The proposed automated method in [61] for parasite detection and identification on thin blood film comprises two different segmentation steps: The foreground-background segmentation and the stained pixels segmentation. The proposed segmentation is performed using morphological area top-hats (using the average cell area value) and morphological double thresholding. For the stained pixels segmentation, the authors modeled the stained and unstained pixel distributions with RGB space histograms and used the probability density function to determine whether a pixel on the input image is stained or not. This work also comprises significant pre-processing effort, like the granulometry-based cell size estimation, which considers the peak index of the granulometry distribution as the average cell area. It also addresses problems like the non-uniform illumination, which is removed using a pre-recorded illumination image, or using a morphological closing operation with a structuring element with size of 5 times the average cell area. Despite this work being only focused on thin blood films, the authors highlighted the importance of future work to investigate the automatic analysis of thick films, since they are more sensitive for malaria parasites density estimation.

In [38], the authors combined the binary images from Otsu's method with the edge detection images from Canny's method for RBCs segmentation, followed by a hole filling process. This work also proposes a pre-processing step based on the estimation of the image illumination, which is then subtracted from the original image.

Thick Blood Films

For non-background objects detection on thick blood films, i.e. MPs, white blood cells (WBCs) and possible Giemsa stain-derived artifacts, the authors in [29] used adaptive threshold found according

to information of the V-Value histogram. However this methodology needs further validation since it was only tested on 20 microscopic images.

The G and B channels of the RGB color space were identified in [17] as very good features to identify objects containing chromatin in Giemsa stained blood films, being not only considered highly discriminative but also almost independent of differences in illumination and staining intensity. They transformed the color input image into a monochrome image $I(x,y)$, that highlights objects containing chromatin: $I(x,y) = arctan(I_{GREEN}(x,y)/I_{BLUE}(x,y))$. The authors also used a black-top-hat morphological operator to separate MPs from both leukocytes and platelets, with a non-flat paraboloid structuring element of radius of 9 and a slope of 1 pixel. It should be taken into account that these fixed parameters might not be suitable for images with different pixel resolutions. The black-top-hat operator is followed by a thresholding operation with a fixed threshold, which according to the authors is reliable given the independence of the G and B channels with regard to illumination and staining intensity. However, the authors do not define the value of this fixed threshold on the publication.

A dark stretching technique is applied in [23] for contrast enhancement of MPs-infected thick blood smear images. The dark stretching is a process that uses an auto scaling method, being the dark areas stretched and the bright areas compressed. The authors state that the dark areas correspond to the MPs in the infected images. To segment the MPs, they use a single threshold value on the stretched image. However, the thresholds have been chosen empirically, and different thresholds had to be applied for different images in order to achieve good segmentation results.

2.4.1.2 Boundary-based Segmentation

Boundary-based techniques seek to extract object boundaries directly, based on identifying the edge pixels located at the boundaries in the image [75].

Thin Blood Films

An improved Circle Hough Transform (CHT) was used in [80] to detect RBCs, based on the consideration that RBCs have a circular pattern. The authors highlighted that CHT has the advantage of handling the segmentation for highly overlapping and oval cells, and noted that the RBCs are much more noticeable in the green channel of the RGB color space. However, RBCs might present shapes significantly different from the expected circular/oval pattern, which might difficult the detection using this approach.

Thick Blood Films

A combination of Absence of Gradients and Nernstian Equilibrium Stripping (AGNES), and Morphological Gradient techniques is used in [78] for the detection of *P.vivax* parasites in thick blood films. A morphological gradient method is first applied in order to enhance the borders of the objects present in the image. This is followed by a threshold detection stage using the K-Median method. The AGNES and K-Median techniques were then used to assign the remaining number of

pixels to each region, using as starting points the image regions previously identified as objects and background. These techniques were locally applied on rectangular sectors corresponding to 20% of the input image, a percentage defined experimentally. According to the authors, this approach might induce the appearance of objects that are not part of the original image in the border of the defined rectangular sectors.

2.4.1.3 Clustering methods

Clustering is a machine learning technique that can be used for segmentation purposes when applied as an indicator of the similarity of different image regions, based on a set of measurements that describes those regions.

Thin Blood Films

The application of 3 different clustering algorithms to segment blood cell images is studied in [42]: Mean-shift, K-means and Fuzzy C-means. The authors support that K-means clustering algorithm achieves best results for blood cell images segmentation, and they used a Median-cut algorithm after applying the K-means in order to reduce the number of regions to an optimum level. However, this approach needs further validation since it only used 5 cropped sub-images.

A segmentation approach using k-means clustering is also proposed in [1] for the detection of *P.vivax* parasites. Different color components of RGB, HSI and C-Y color models have been analyzed, and the S component of C-Y color model has proven to be the best, with segmentation accuracy and F-score of 99.46% and 0.9370, respectively.

In [32], the authors used the b*-color channel from the CIE L*a*b* color space for k-means clustering as an unsupervised segmentation approach to identify malaria parasite tissues. They used 118 Leishman-stained microscopic images with reported results of 76% and 60% for SE and SP, respectively. It is worth noting that these results refer to classifying the images as infected/not infected, thus not giving information about the precise number of correctly identified MPs in each image.

2.4.1.4 Classifier-based methods

Classifier-based methods for segmentation rely on the usage of two-class models for segmentation purposes.

Thin Blood Films

In [60], a Bayesian pixel classifier has been employed in order to differentiate between the stained and non-stained pixels. The class conditional probability density functions of the stained and the non-stained classes were estimated using the non-parametric histogram method,

2.4.2   Feature Extraction

The primary objectives of feature extraction are reducing the computational complexity of the subsequent process and facilitating a reliable and accurate recognition for unknown novel data, being the last objective particularly important for computer vision and pattern recognition systems. Moreover, the in-depth understanding of the domain-specific knowledge gained by human experts on the problem being addressed can be of extreme importance for the design of a reliable and effective feature extraction engine [27].

2.4.2.1   Binary Objects Measures

A binary object can be described in terms of its size (e.g. area, perimeter), pose (e.g. centroid, orientation), shape measures (e.g. thinness ratio, rectangularity, circularity, Euler number, moments, elongation), shape descriptors (e.g. differential chain code, fourier descriptors, media axis transform, graph representation) or distance to other objects (e.g. Euclidean distance, city-block distance, chessboard distance) [75].

Thin Blood Films

In [37], the infected RBCs detection in thin blood smears is based on relative ratios between chromatin dots and RBCs terms of area and centroids distances. For the same purpose, the work in [61] uses shape measurements like compactness and moments of inertia.

Thick Blood Films

The segmented non-background objects are distinguished in [29] according to size, and the MPs species *P.falciparum* and *P.vivax* are distinguish according to the chromatin size. However, this methodology was tested only on 20 images and the thresholds were defined in number of pixels, thus not suitable for images with different pixel resolutions.

2.4.2.2   Gray-Level Objects Measures

Gray-level objects measures consist on measurements derived from the intensity distribution of the object. There are 3 main categories of gray-level object measurements: Intensity measures (e.g. integrated and average optical intensity, contrast) histogram measures (e.g. mean, standard deviation, skew, entropy, energy) and texture measures (e.g. statistical texture measures, power spectrum features) [75].

Thin Blood Films

For detection and differentiation between WBCs and *P.falciparum* gamecocytes, the authors in [30] start by finding the centroids of each detected stained component. The proposed algorithm considers as candidates the neighborhood of the listed centroid coordinates within the diameter of

the WBCs. The candidates are marked as WBCs if the neighborhood region presents low mean intensity and less variance, and as gametocyte of *P.falciparum* if the region has high eccentricities (variance) and average intensity.

The authors in [80] observed that nucleated components result in distinctively high intensity values in the B channel of the RGB color space, while the same nucleated components in the G channel exhibit very low intensity values. Therefore, they proposed an intensity measure based on the differences between the B and the G color intensity channels, in order to stretch the contrast for visual perception and emphasize nucleated objects.

The methodology proposed by [4] aims to detect 3 regions inside the infected RBCs, particularly the MPs nucleous, MPs cytoplasm and RBCs cytoplasm. Features of those regions are then extracted for classification purposes, based on area ratios and range of intensities of each region.

In another work [60], the following gray-level measures were extracted for further MP/non-MP classification in thin blood films: Hu moments, relative shape measurements, histogram and color auto-correlogram. According to the authors, the last two features are the most effective for MPs classification.

The color histogram is used in [61] after quantization into 32 colors, as well as the local area granulometry for each RGB channel. It worth noting that the features were normalized (for zero mean, 1 variance) first on the training set, being the mean and standard deviation calculated and then used for the normalization of the testing set.

The authors in [38] extracted four different features: 1) Gradient; 2) Flat texture (determined by computing the difference between the original image and the filtered image using median filter); 3) Color histogram; and 4) Area granulometry.

Thick Blood Films

In order to differentiate MPs from artifacts in thick blood films, the authors in [17] extracted 174 different features. The features were grouped in 3 main groups: 1) Statistical moment features - 4 central moments (mean, variance, skewness, and kurtosis), Hu's set of 7 invariant moments [26], 49 Zernike moments of orders up to 12 [33]; 2) Texture features: Haralick's 13 co-occurance matrix features [24]; Unser's 18 sum and difference histogram features [66]; Chen's 16 statistical geometrical features [12]; 5 features proposed by Young et al. [77] that describe the distribution of chromatin in the ROI; 3) Color features: 60 features representing a 60-bin histogram of the hue channel of the ROI; 2 features described by Kovalev et al. [34] that represent cyan shifts in the ROI. The following features were extracted in the work presented in [46]: mean; standard deviation; kurtosis; skewness; entropy of the histograms of R,G and B channels from RGB space, H channel from HSV space, and H channel of HSI space.

In another recent work, 3 groups of features were extracted in [78] for each RGB channel: 1) Color features: standard deviation, 7 Hough moments of color and color range; 2) Texture features based on the co-occurrence matrix (in 4 directions): homogeneity, contrast, GLMSR (General Linear Model Simple Regression), standard deviation, second angular moment and correlation; 3) Texture features based on the Wavelet transform: energy, mean and standard deviation. Four

wavelet families were used (Haar; biorthogonal 1,3; Daubechies 2; and Daubechies 8) considering 2 decomposition levels, being applied in each level a low and high pass filter.

In [47], the authors extract two types of features: 1) Connected component features: Perimeter; Moment of Inertia; Elongation; Jaggedness; and Maximum λ (consists in the maximum child gray level minus the current gray level); 2) Moment features: the moment m_{00}, the central moments, u_{11}, u_{20}, u_{02} and Hu moments h_0, h_1, h_2.

2.4.3   Feature Selection

In order to build a good classification model, the reduction of the number of attributes used on the classification process may not only have positive impact in terms of the processing time, but also in terms of the classification results. Feature selection techniques play an important role in this context, and they can be organized into three categories: filter methods, wrapper methods and embedded methods [20].

Filter Methods rank each feature according to some univariate searching function and select the highest-ranking features, where the scoring should reflect the discriminative power of each feature. Some of the most common univariate filter methods includes Bayesian Network, Information Gain, Signal-to-Ratio, Euclidean Distance or Correlation Squares (R^2) [20]. Filter methods are usually very efficient and fast to compute, but comprise some significant drawbacks like the redundancy of the selected features, which can carry the same information. Another important disadvantage of the filter methods is the fact that this selection does not consider some important relationships between features, since features can receive a low score by the ranker algorithm when used by itself, but be very useful when combined with other features.

Opposite to filter techniques that consider the ranking of each feature independently, Wrapper and Embedded Methods are specific to a given machine-learning algorithm. In the Wrapper Method, a search is conducted using a specific classifier in order to find the subset of features with which the classification algorithm performs the best. For instance, using forward selection, the Wrapper Method estimates the accuracy of adding each unselected feature to the feature subset, and the feature that most improves the accuracy is selected. These methods typically terminate when the estimated accuracy of adding any feature is less than the estimated accuracy of the feature set already selected [15].

Thick Blood Films

An optimal feature subset was chosen in [17], based on the 174 previously extracted features for MPs detection. The features were first normalized to have zero mean and a standard deviation of one. The authors proposed a 2-step feature selection methodology: an univariate ranking is first applied in order to keep only the 60 features that have the highest univariate discriminative power, and then a genetic algorithm is used for automatic selection of an even smaller feature subset.

Another example of feature selection for MPs detection is referred in [78], where the Principal Component Analysis (PCA) was used to identify features that are redundant and do not carry new information, thus also involving feature transformation.

2.4.4   Classification

In machine learning and statistics, classification is the problem of identifying to which of a set of categories (sub-populations) a new observation belongs, on the basis of a training set of data containing observations (or instances) whose category membership is known. In the terminology of machine learning, classification is considered an instance of supervised learning, i.e. learning where a training set of correctly identified observations is available [3].

2.4.4.1   Naïve Bayes Classifier

The Naïve Bayes classifier assumes that the presence (or absence) of a particular feature of a class is unrelated to the presence (or absence) of any other feature, meaning that it assumes the independency of variables given the class. In spite of its naive design and apparently over-simplified assumptions, Naïve Bayes can often outperform more sophisticated classification methods applied in many complex real word situations. An advantage of the Naïve Bayes classifier is that it requires a small amount of training data to estimate the parameters of the model [28].

Thin Blood Films

In [4], the classification model for the identification of infected RBCs achieved a SE of 92.59% and a SP of 99.65% using a Bayes Decision Rule classifier. However, only 60 images were used for training and 20 for testing.

2.4.4.2   K-Nearest Neighbor

One of the most fundamental and simple classification methods is K-nearest neighbor (kNN), being often used when there is little or no prior knowledge about the distribution of the data. Nearest neighbor algorithm is based on the principle that the instances within a dataset will generally exist in close proximity to other instances with similar properties [2].

Thin Blood Films

For detection of MPs in thin films, in [60] the authors proposed a distance weighted kNN classifier trained with the extracted features, and a detailed performance comparison is presented. The authors state that the proposed method achieved 74% of SE and 98% of SP.

The authors in [61] proposed an automated method for MPs detection and identification on thin blood film, where three classifiers were tested: the kNN classifier achieved 72.4% of SE and 97.6% of SP; the Fisher Linear Discriminant achieved 71.5% of SE and 93.9% of SP; and the Back Propagation Neural Network achieved $70.5 \pm 1.7\%$ of SE and $96.6 \pm 0.4\%$ of SP. Furthermore, the

authors proposed and compared three different classification models for species and life-cycle-stage identification: The first model (20-class) performs detection, species, and life-cycle-stage recognition in a single classification, simultaneously considering non-parasite classes. The second and third models perform a binary detection beforehand followed by a single 16-class classification or two 4-class classifications for identification, respectively. The 20-class model was considered the most favorable model.

In another recent work, the authors in [38] tested five different classifiers, and stated that the kNN outperformed others with 80% of SE and 95.5% of SP.

2.4.4.3 Support Vector Machines

A support vector machine (SVM) constructs a hyperplane or set of hyperplanes in a high-or infinite-dimensional space, which can be used for classification. Intuitively, a good separation is achieved by the hyperplane that has the largest distance to the nearest training data point of any class (so-called functional margin), since in general the larger the margin the lower the generalization error of the classifier [25].

Thin Blood Films

For MPs classification, the authors in [17] used a SVM with a radial basis function kernel with gamma G = 0.125, and a cost factor of C = 1.0. The stated results showed a SE of 97% combined with 0.8 false-positive detection per image.

2.4.4.4 Neural Networks

Neural Networks (NN) are based on the way biological nervous systems process information and are applied to a large number of real world problems. They are especially well suited to problems that people are good at solving, but the algorithm solution is too complex to be defined. The most common NN model is the multilayer perceptron, which is a feed-forward artificial NN that maps sets of input data onto a set of appropriate output, using three or more layers of neurons with nonlinear activation functions [65].

Thick Blood Films

A NN with 5 neurons in the output later was used in [78], of which three neurons represent the parasites of interest (gametocytes of *P.falciparum*, squizonts of *P.vivax* and gametocytes of *P.vivax*), and the two remaining neurons correspond to sediments and WBCs.

2.4.4.5 Genetic Programming

Genetic programming is an evolutionary algorithm-based methodology inspired by biological evolution to find computer programs that perform a user-defined task. Essentially genetic programming is a set of instructions and a fitness function to measure how well a computer has performed a task.

It is a specialization of genetic algorithms where each individual is a computer program, being a machine learning technique used to optimize a population of computer programs according to a fitness landscape determined by a program's ability to perform a given computational task [48].

Thick Blood Films

In [46], the classification was made using Genetic Programming to identify parasites and also to detect type and phase of the parasite. Two different classification models were considered using a dataset of 180 thick blood film sub-images cropped manually: a first model (two classes) with an accuracy of 95.49% for non-parasites and 95.58% for parasites, and a second model (six classes) with an average accuracy of 90.25% for non-parasites, 82.25% for *P.vivax* trophozoites, 75.83% for *P.vivax* schizonts, 81.75% for *P.vivax* gametocytes, 90.75% for *P.falciparum* trophozoites and 86.75% for *P.falciparum* gametocytes.

2.4.4.6 Extremely Randomized Trees

Extremely Randomized Trees is a tree-based ensemble method for classification that consists of randomizing strongly both attribute and cut-point choice while splitting a tree node. In the extreme case, it builds totally randomized trees whose structures are independent of the output values of the learning sample. The strength of the randomization can be tuned to problem specifics by the appropriate choice of a parameter [21].

Thick Blood Films

The authors in [47] used a Extremely Randomized Trees classifier with an ensemble of 250 trees and a maximum tree depth of 5. The authors stated that this classifier has the advantages of being fast and memory-efficient, which might be useful in situations where classification must be carried out for instance on a mobile device with limited computational resources. The authors stated an area under the curve (AUC) of 0.97 for the receiver operating characteristic (ROC) curve.

2.5 Summation and Critical Appreciation

The proposed methodologies were divided in two main groups: MPs in thick blood films (see Table 2.1) and MPs in thin blood films (see Table 2.2).

Malaria parasites detection and segmentation techniques in microscopic images are, in general, still in need of improvement and further testing. Most of the methodologies reviewed in this work were tested with a limited number of images, and more studies with significantly larger datasets for the evaluation of the proposed approaches are needed. Despite promising results reported during the past years, the great majority of the computer-aided methods found on the literature for malaria diagnosis are based on images acquired under well controlled conditions and with proper microscopic equipment. However, one should take into account that 80% of malaria cases occur in Africa, where this type of equipment is scarce or even nonexistent in common healthcare facilities.

Table 2.1: Proposed approaches for the detection and/or segmentation of malaria parasites in thick blood films.

Author	Year	Segmentation	Features	Classifier	#Images	SE / SP (%)
(Kaewkamnerd et al., 2011)	2011	Adaptive Thresholding	• Hue histogram • Chromatin size	-	20 (FV)	- / -
(Elter et al., 2011)	2011	Thresholding	• 60 statistical moment features • 52 texture features • 62 color features	SVM	256 (FV)	97 / -
(Yunda et al., 2012)	2012	AGNES + Morphological gradient techniques	• 27 color features • 72 co-occurrence matrix texture features • 62 Wavelet transform texture features	Neural Network	248 (FV)	- / -
(Purnama et al., 2013)	2013	-	• Mean and standard deviation • Kurtosis • Skewness • Entropy of the histograms of: (i) R, G and B channels from RGB space; (ii) H channel from HSV space; (iii) H channel of HIS space	Genetic Programing	180 (CS)	96 / 96
(Quinn et al., 2014)	2014	-	• Connected component features (Perimeter; Moment of Inertia; Elongation; Jaggedness; and Maximum λ) • Moment features (moment m_{00}, the central moments, u_{11}, u_{20}, u_{02} and Hu moments h_0, h_1, h_2)	Extremely Randomized Trees	2703 (M)	*ROC AUC = 0.97

#Images indicates the number of images used to validate the proposed approach; SE and SP indicates the reported sensitivity and specificity of the proposed approach, respectively; AGNES stands for "Absence of gradients and Nernstian equilibrium stripping"; FV stands for full view images; CS stands for manually cropped sub-images; M stands for mobile acquired images.

Table 2.2: Proposed approaches for the detection and/or segmentation of malaria parasites in thin blood films.

Author	Year	Segmentation	Features	Classifier	#Images	SE / SP (%)
(Tek et al., 2006)	2006	Bayesian pixel classifier	• Histogram • Hu moments • Relative shape measurements • Color auto-correlogram	kNN	260 (FV)	74 / 98
(Makkapati et al., 2009)	2009	Thresholding	• Area ratios • Centroids distances between RBCs measurements and chromatin dots	-	- (FV)	83 / 98
(Mandal et al., 2010)	2010	Normalized cut	-	-	37 (CS)	- / -
(Zou et al., 2010)	2010	Circle Hough transform	-	-	- (FV)	- / -
(Tek et al., 2010)	2010	Thresholding	• Color histogram • Local granulometry • Shape measurements (e.g. compactness, moments of inertia)	kNN	630 (FV)	72 / 98
(Kareem et al., 2011)	2011	Thresholding	-	-	- (FV)	- / -
(Muda et al., 2011)	2011	K-means clustering + Median-cut	-	-	- 5 (CS)	- / -
(Anggraini et al., 2011)	2011	Otsu's method	• Range of intensity of infected and normal RBCs • Area ratios	Bayes Classifier	80 (FV)	93 / 99
(Ghosh et al., 2011)	2011	Fuzzy divergence	-	-	150 (CS)	- / -
(Fang et al., 2011)	2011	Thresholding	-	-	100 (FV)	87 / 97
(Kareem et al., 2012)	2012	Thresholding	• Gradient • Flat texture	-	200 (FV)	- / -
(Malihi et al.,2013)	2013	Otsu's method + Canny's method	• Color Histogram • Area Granulometry	kNN	363 (FV)	80 / 96
(Abdul et al., 2013)	2013	K-means clustering	-	-	100 (CS)	94 / 96
(Khan et al., 2014)	2014	K-means clustering	• b* color channel from the CIE L*a*b* color space.	-	118 (FV)	76 / 60

#Images indicates the number of images used to validate the proposed approach; SE and SP indicates the reported sensitivity and specificity of the proposed approach, respectively; kNN stands for the k-Nearest Neighbor; FV stands for full view images; CS stands for manually cropped sub-images.

Furthermore, the analysis of thin blood smears is much more addressed in the literature when compared with thick blood smears. This is probably because the image processing tasks required on thick blood smears analysis are considerably more challenging, given the fact that thin blood smears consist on a single layer of blood elements. Thus, several additional image artifacts are avoided in thin blood smear analysis, like the overlap of blood elements or the recurrent appearance of unfocused structures caused by the location of those structures in different focal planes. Thick blood smears are considered 20-40 times more sensitive in detecting malaria parasites, and therefore should be equally addressed, despite the additional image processing challenges.

2.6   Conclusion

This work collects and reviews various image processing and analysis approaches already proposed on the literature for the detection and segmentation of malaria parasites in blood smear microscopic images. This timely review aims to support the increasing interest in the development of image processing-based systems to be used in rural areas of developing countries, which might be the next future trend in malaria computer-aided diagnosis.

The development of new microscopic devices, ideally portable and low cost, is an area that can greatly improve the chances of the successful deployment of computer vision CAD solutions for malaria diagnosis in the field. Taking into account the high customs taxes and import duties currently in practice in most of the African countries, the easy replicability of these microscopy devices in third world countries should also be an issue to address. Several others additional requirements for this type of microscopic devices can be equally considered, like automating the device as much as possible, discarding the need of considerable expertise and train of the technician in terms of maneuvering the microscope, or supplying the energy needed for the illumination and/or any type of automation through the mobile device battery, thus discarding the need of an additional power source.

The mobile phone is currently Africa's most important digital technology, and is boosting African health as it emerges as a platform for diagnosis and treatment. In 2000, few Africans had a phone, but today about three-quarters do [79]. Just as African telecommunications largely skipped over landline infrastructure and went straight to mobile phones, some experts say African medicine can skip over centralized labs [16]. Considering the recent significant improvements of the new generation of mobile devices in terms of image acquisition and processing power, if a reliable automatic diagnostic performance is ensured through the usage of those devices, one would dramatically reduce the effort in the exhaustive and time consuming activity of microscopic examination.

Moreover, the lack of highly trained microscopists on malaria diagnosis in rural areas could then be complemented by a significantly less specialized technician that knows how to operate the system and prepare blood smears. The usage of mobile devices in the system architecture can also bring significant improvements in terms of portability and data transmission. Finally, malaria diagnosis might be just one element of a suite of diagnostic software tests running on this type of

system. Several other tests could simultaneously be carried out using the same images, for instance cell counting or detection of other hemoparasites like microfilaria or trypanosoma.

2.7   *AI-powered Microscopes for Malaria Parasites Detection[1]

In the past years, a few companies showed to be actively working on microscopic solutions powered with Artificial Intelligence (AI) for malaria diagnosis. One of the most relevant solutions in this area is the *EasyScan GO* microscope, which resulted from a joint effort between Motic (microscope manufacturer) and Global Good (a partnership between Intellectual Ventures and Bill Gates). The *EasyScan GO* system has the following characteristics [41, 40]: i) accepts standard field-prepared, Giemsa slides; ii) scans around 300 FOVs (at multiple focal planes) on 0.1 μL of blood, taking 20 minutes; iii) has a resolution of 11.36 pixels/μm and each FOV is 1280x960 pixels; iv) the automated analysis runs on a computer that should be connected to the microscope. Field tests of an early prototype showed that the developed machine learning algorithm has a SE of 91.6% and 94.1% SP for *P.falciparum* detection on thick smears, using a database of 1452 thick blood samples. This results are detailed in a recent publication [40] that cites one of our previous works [50], being reported the usage of similar approaches like adaptive thresholding and classification with SVM, which are merged at a later stage with CNN classification. Despite being a remarkable promising solution, it currently only covers the automated detection of *P.falciparum* detection on thick smears. Additionally, the current size of the overall solution might compromise its portability, which may prove as a barrier if constant displacements are required (see Figure 2.6).

Figure 2.6: EasyScan GO solution: (Left) A researcher inserts a cassette with a blood smear into the EasyScan GO; (Right) Transport case (from [41]).

Another solution that is worth to mention is the *SightDx Parasight Platform* by Sight Diagnostics [18], a desktop system for computerized malaria diagnostics. This system requires a sample preparation different from the gold standard, particularly by using a patented technology that creates a monolayer of cells. Another difference from the gold standard is the usage of DNA and RNA fluorescent dyes. In detail, the *SightDx Parasight Platform* has the following characteristics: i)

---

[1]Note: This section is not present in the published version of the article, since most of these data was only made available by the referred companies after its publication.

usage of 3 different LED light sources (370 nm, 475 nm and 530 nm); ii) total scan time per sample of 4 minutes, with approximately 800 images scanned per sample; ii) the results are processed by a machine-learning algorithm that performs feature extraction by a computer vision SVM classifier to determine parasitemia levels and species, based on a dataset of over 2500 positive and negative patient samples. A recent multisite trial [18] compared the device to PCR, being reported SE and SP above 99% for malaria and species identification on around 450 samples. In terms of parasite counts, an average Pearson correlation coefficient of 0.84 with trained microscopists was also reported. However, it should be noted that the system currently only detects *P.falciparum* and *P.vivax* species. Additionally, the usage of a sample preparation approach different from the gold standard might difficult the interpretability and validation of the automated results by microscopists on the field, since the visual characteristics of the images produced by the *SightDx Parasight Platform* are significantly different from the typical images obtained through standard brightfield microscopy (see Figure 2.7).
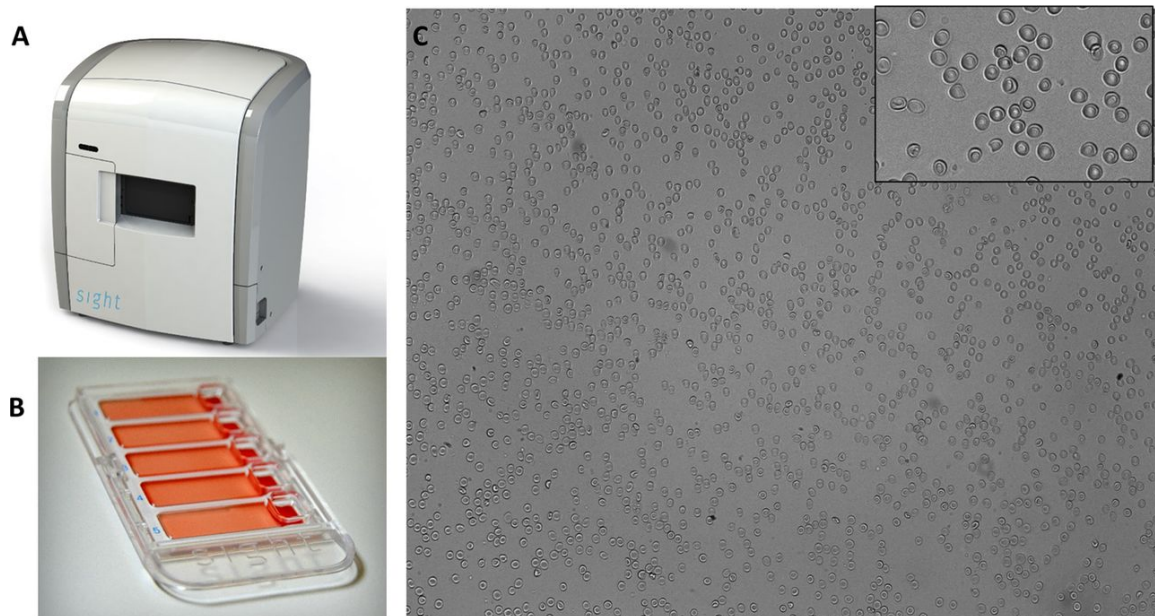
Figure 2.7: SightDx Parasight Platform: (**A**) Desktop scanning device; (**B**) Loading cartridge, which holds five patient samples; (**C**) Image of the monolayer at x20 (from [18]).

Part II

Methodologies and Results

Chapter 3

μSmartScope: Towards a Fully Automated 3D-printed Smartphone Microscope with Motorized Stage

Luís Rosado, Paulo T. Silva, José Faria, João Oliveira, Maria João M. Vasconcelos, Dirk Elias, José M. Correia da Costa and Jaime S. Cardoso

Scientific contributions presented in this chapter were also published in:

μSmartScope: 3D-printed smartphone microscope with motorized automated stage

Luís Rosado, João Oliveira, Maria João M. Vasconcelos, José M. Correia da Costa, Dirk Elias and Jaime S. Cardoso

Abstract

Microscopic examination is the reference diagnostic method for several neglected tropical diseases. However, its quality and availability in rural endemic areas is often limited by the lack of trained personnel and adequate equipment. These drawbacks are closely related with the increasing interest in the development of computer-aided diagnosis systems, particularly distributed solutions that provide access to complex diagnosis in rural areas. In this work we present our most recent advances towards the development of a fully automated 3D-printed smartphone microscope with a motorized stage, termed μSmartScope. The developed prototype allows autonomous acquisition of a pre-defined number of images at 1000x magnification, by using a motorized automated stage fully powered and controlled by a smartphone, without the need of manual focus. In order to validate the prototype as a reliable alternative to conventional microscopy, we evaluated the μSmartScope performance in terms of: resolution; field of view; illumination; motorized stage performance (mechanical movement precision/resolution and power consumption); and automated focus. These results showed similar performances when compared with conventional microscopy, plus the advantage of being low-cost and easy to use, even for non-experts in microscopy. To extract these results, smears infected with blood parasites responsible for the most relevant neglected tropical diseases were used. The acquired images showed that it was possible to detect those agents through images acquired via the μSmartScope, which clearly illustrate the huge potential of this device, specially in developing countries with limited access to healthcare services.

Keywords: microscopy; mobile devices; motorized microscope stage; developing countries, mobile health.

3.1   Introduction

Neglected tropical diseases (NTDs) are a group of parasitic infectious diseases that affect over 1.5 billion of the world's poorest population, including 875 million children [63]. The gold standard for detection of several NTDs is microscopic examination, particularly via the visualization of different types of human biological products, like blood smears (e.g Malaria, Lymphatic filariasis, African Trypanosomiasis), stool smears (e.g. intestinal helminths), and urine smears (e.g. Schistosomiasis) [67]. Unfortunately, reliable identification of these parasitic infections requires not only proper microscopic equipment, but also high-standard expertise for subsequent microscopic analysis. These requirements represents the most common practical difficulties experienced in rural health facilities, being closely related with the increasing interest of mobile health (mHealth) and computer-aided diagnosis solutions for those particular scenarios.

The mobile phone is currently Africa's most important digital technology. In the year 2000 few Africans had a mobile phone, but today about three-quarters do [79]. So it becomes natural that mHealth is starting to play an important role when it comes to health in Africa, particularly through the usage of solutions that allow skipping over centralized laboratories [16]. For instance,

the usage of advanced computer vision approaches coupled to the increasing processing capabilities of mobile devices is already showing promising results in the area of malaria diagnosis [50, 51]. Moreover, considering the paramount importance of microscopic examination for NTDs detection, the development of new portable microscopic devices is an area that can greatly improve the chances of the successful deployment of innovative solutions for NTDs diagnosis in underserved areas [49]. To achieve that purpose, the constant advances and increasing possibilities coming from additive manufacturing should certainly be taken into account, since 3D-printing currently allows faster and cheaper prototyping.

In this chapter we report our most recent advances towards the development of a fully automated 3D-printed smartphone microscope with a motorized stage, termed *μ*SmartScope [52]. The usage of this prototype can be resumed as follow: the process starts by placing the smartphone in the *μ*SmartScope along with the smear, and have a set of magnified images acquired autonomously by the smartphone camera sensor. This collection of images is then analyzed, either automatically through computer vision approaches, or manually by a specialist on a remote location. It is worth mentioning that we took into account several particularities of the African reality during the design of this device, like the high customs taxes and import duties currently in practice in many African countries; this motivated us to favor solutions easily replicable in developing countries. Several other additional requirements were equally considered, like automating the device as much as possible, discarding the need of considerable expertise and train of the technician in terms of maneuvering the microscope, or supplying the energy needed for the illumination and/or any type of automation through the mobile device battery, thus discarding the need of an additional power source.

This chapter is structured as follow: Section 3.1 corresponds to Introduction and presents the motivation and objectives of this work; Section 3.2 summarizes the related work found on the literature; Section 3.3 gives overview of the *μ*SmartScope, with focus for the Optics and Illumination modules; Section 3.4 details the Motorized Automated stage module; Section 3.5 describes the Automated Focus procedure; In Section 3.6 the Results and Discussion are presented; and finally the Conclusions and Future Work are drawn in Section 3.7.

3.2   Related Work

Some research has been made in the last years to develop cell-phone based systems that provide low-cost alternatives to conventional microscopy. The microscopy designs of the proposed systems can be separated in three different areas: lensless, on-lens and attachment-based approaches.

The lensless approaches are based on the principles of holographic microscopy, i.e. the microscopic images are reconstructed from the holograms captured by the cell-phone. This approach has the advantage of not requiring any lenses or optical component as well as obtaining images with large field-of-view (FOV). However, acceptable resolutions are only obtained for small magnifications ($\sim$40x magnification, NA= 0.65 objective) and processing power is needed to reconstruct the image [64, 45].

On-lens approaches usually employ a refractive element directly attached to the smartphone camera at the focus, or a ball lens mounted in front of the camera lens [5, 14]. Despite being a low-cost alternative, the ball lens produces a spherical focal plane, which creates aberrations and reduces drastically the usable FOV. Moreover, magnification and radius of the ball lens are inversely linked, so in order to achieve 1000x magnification we need a ball lens with radius of 0.15 mm [14], which can turn the mounting and alignment process with the camera lens really challenging.

The attachment-based approaches covers the majority of the solutions already reported on the literature, which requires coupling additional hardware to the cell-phone, such as commercial lenses or illumination modules [56, 59, 45]. This approach usually takes advantage of complex optical elements that allow achieving suitable resolutions at high magnifications (e.g. ∼1000x), which increases the overall cost of the system, but is currently a requirement for the microscopic examination of several neglected diseases. With high magnifications also emerges the limitation of having a small FOV, thus requiring the development of mechanisms to move the smears in order to cover a large area of the specimen. Moreover, it was verified that the majority of reported works are designed for a unique cell-phone model, which can greatly compromise the adoption of the proposed solution.

In this work, we present a 3D-printed microscope that can easily be attached to a wide range of mobile devices models. To the best of our knowledge, this is the first proposed smartphone-based alternative to conventional microscopy that allows autonomous acquisition of a pre-defined number of images at 1000x magnification with suitable resolution, by using a motorized automated stage, fully powered and controlled by a smartphone, without the need of human interaction.

3.3 μSmartScope Overview

Considering that developing a cheap and easily replicable alternative to conventional microscopes was one of the main goals of this work, the μSmartScope was prototyped using Fused Filament Fabrication (FFF) technology. The FFF is a 3D printing technology for rapid prototyping, which works by laying down consecutive layers of material in very precise positions, in our case Polylactic Acid (PLA) termoplastic. Layer by layer, a desired model is built from a digital file. Despite the great advantages of this technology, 3D printing has limitations like any other fabrication process, such as being sensitive to environmental variables like temperature, humidity or dust. Thus, we took those variables into consideration during the design and printing process, for instance by accounting the expected dimensional contraction during the cooling process or checking the absence of any superficial humidity/dust on the filament, which showed to have a significant impact in the quality and dimensional accuracy of the printed pieces.

As previously reported [52], the μSmartScope can be divided in 3 major modules (see Figures 3.1 and 3.2): i) Optics ; ii) Illumination; and iii) Motorized Automated Stage (termed μStage). By analyzing the results previously reported, it becomes clear that the μStage module was the bottleneck of the system. The previous mechanical design had a significant unpredictable behavior due to small irregularities of the 3D printed parts, and it was significantly slower than human

technicians in autonomously focusing microscopic fields. Thus, a major refactor was made to the μStage module, which consequently had a pronounced impact on the overall performance of the μSmartScope. Due to these pronounced modifications, we opted to dedicate a separate section on this work to μStage module (see Section 3.4). On the other hand, the Optics and Illumination modules suffered only minor improvements when compared to the previously reported version [52], so we following summarized these two modules under this section.

Figure 3.1: The μSmartScope prototype, with smartphone attached and microscopic slide inserted.
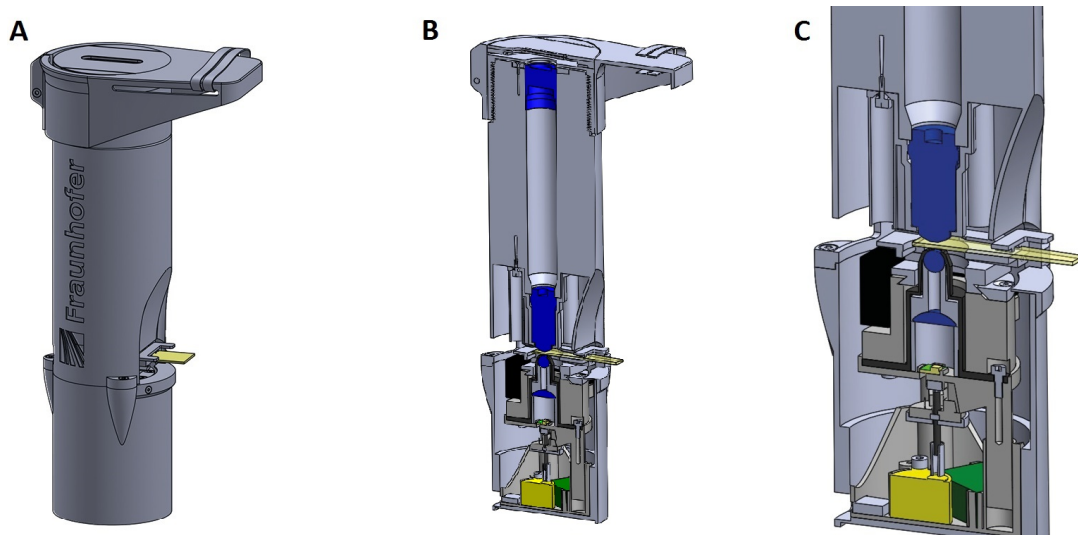
Figure 3.2: μSmartScope render models: (**A**) External view with microscope slide inserted (at yellow); (**B**) Cut view with optical and electrical components highlighted; (**C**) Detail of the cut view.

3.3.1 Optics Module

The selected commercial lenses used to construct the µSmartScope were supplied by Bresser, a vendor that showed a good price-quality relation for the required optics (see Figure 3.3). Particularly, we used the Planachromat 100x oil-immersion objective (Bresser #5941500) and the Wide Angle 10x Eyepiece (Bresser #5941700).
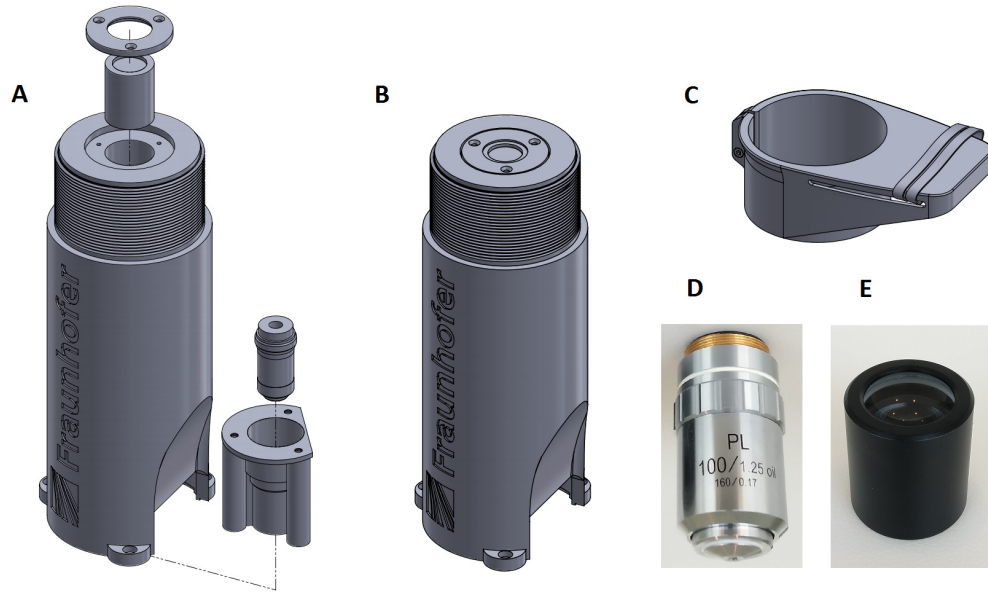
Figure 3.3: Optics module: (**A**) Exploded view; (**B**) Assembled view; (**C**) Smartphone holder; (**D**) Planachromat 100x oil-immersion objective lens; (**E**) Wide angle 10x eyepiece lens.

3.3.2 Illumination Module

To allow a uniform illumination of a microsocpic slide, using just a LED is usually not enough because most of the light is lost to parts of the specimen that are not being analyzed. To counter that, a light condenser is normally used in conventional microscopes. The condenser is a lens (or multiple lenses) that concentrates the light from the illumination source and focus it in the part of the specimen that is being analyzed by the amplification device. This device, in turn, magnifies the light beam, allowing an uniform illumination. Since all support materials for the optical components of the µSmartScope are 3D-printed, the minimum resolution of the 3D-printer was taken into consideration during the design of the illumination module.

Several topologies of condensers can be used with their pros and cons. One of the cheapest options with acceptable performance is the Abbe condenser, which uses a plano-convex lens to pre-concentrate the light into a smaller ball or half-ball lens that, in turn, provides the final concentration of light. This arrangement guarantees a good result by using cheaper individual lenses instead of an expensive, custom made, one. To design our condenser we selected a 20.4 x 25 mm plano-convex lens (Edmund Optics #43483) and a 10 mm N-BK7 Ball Lens (Edmund Optics #32748). In order

to calculate the Back-Focal Length (BFL), i.e. distance on the optical axis between last active optical surface and the specimen plane, we used the following equation [14]:

$$BFL = \frac{1}{2} \cdot \frac{r \cdot (2 - n)}{(n - 1)}, \tag{3.1}$$

where $r = 5mm$ is the radius of the ball lens and $n = 1.517$ is the Index of Refraction of the N-BK7 optical material. This gives a $BFL = 2.34mm$, as shown in Figure 3.4.
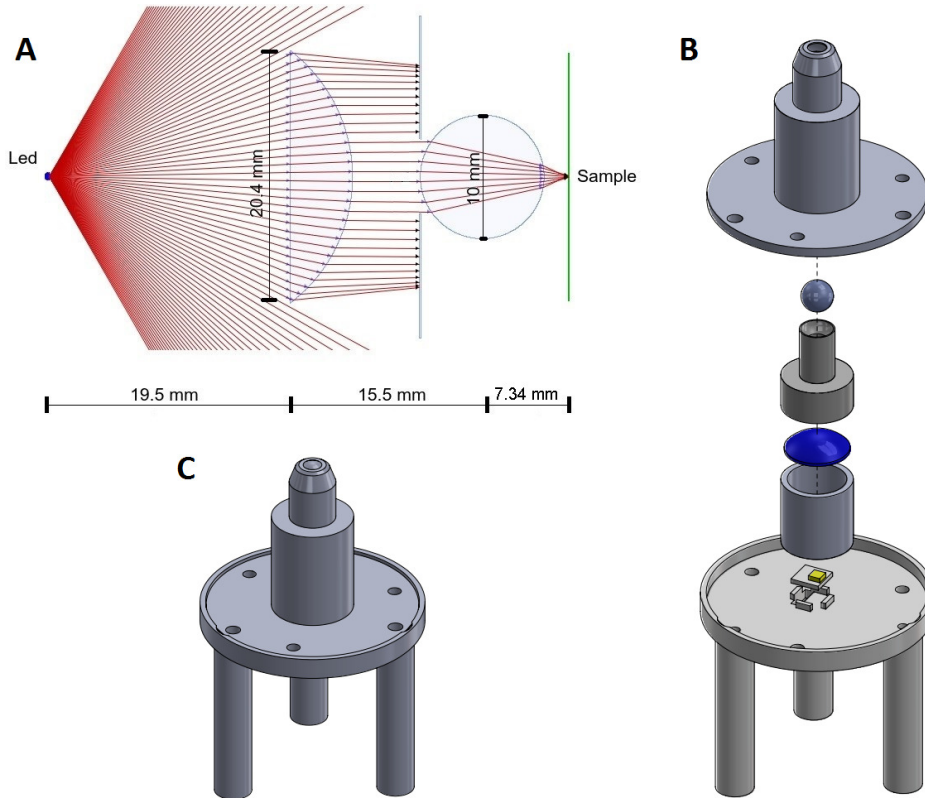
Figure 3.4: Illumination module: (**A**) Schematic of the developed light condenser generated with OpticalRayTracer® optics design software; (**B**) Exploded view of the light condenser with lenses (at blue) and LED light (at yellow); (**C**) Assembled view of the light condenser.

Despite the distances defined on Figure 3.4 being strictly respected, during the design we also had to ensure that the center of the ball lens was both carefully aligned with the center of the plano-convex lens and with the center of the objective lens.

3.4   µStage Module

The microscopic examination of blood smears usually requires the visual analysis of different microscopic fields (i.e. positions) of the specimen. The minimum number of required microscopic fields directly depends on the target disease and used optical magnification, i.e. depends on the size of the target structures. For instance, the World Health Organization (WHO) recomends the analysis of 100 different microscopic fields of a blood sample to perform a malaria microscopy

test [70]. It should be noted that this process is manually performed by trained staff and can be extenuating, requiring that the operator takes regular breaks in order to ensure maximum attention.

The approach proposed on this work aims to improve this process by performing the microscopic slide movement autonomously and on-demand using a smartphone. The μStage was developed for that specific purpose (see Figure 3.5), which consists on a motorized stage designed to be as cheap as possible, being powered through the USB-OTG connection of the smartphone. In order ensure its flexibility, most of the μStage structure is modular and can be adapted without major refactors of the entire module. It is worth noting that during the design of the μStage we tried to minimize the usage of mechanical components and give priority to 3D-print as many parts as possible, in order to reduce costs and ensure an easy replication of the prototype.
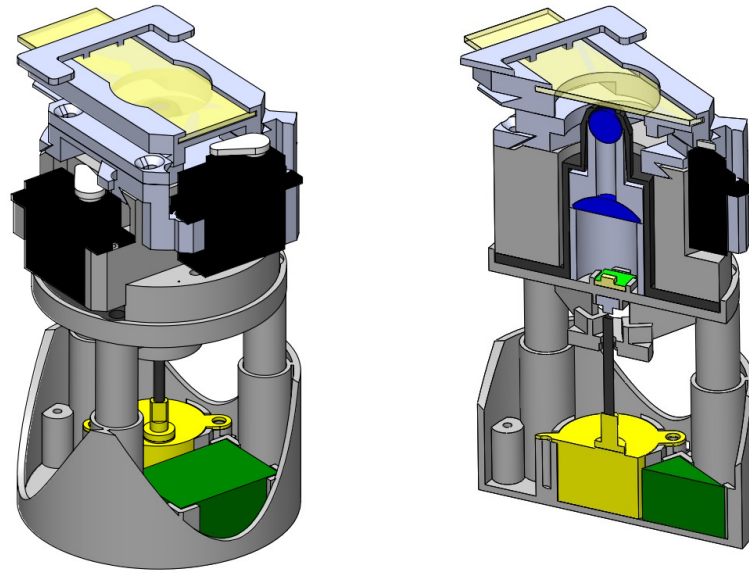
Figure 3.5: μStage module: External view (on the left) and cut view (on the right), with detail of servo motors (at black), step motor (at yellow), electronics (at green) and optics (at blue).

Regarding the μStage mechanical structure, it can be divided in two main functional submodules (see Figure 3.6): i) the **XY-plane Submodule**, responsible to move the stage on the XY plane (i.e. to obtain different microscopic fields); and ii) the **Z-axis Submodule**, responsible to move the stage in the Z axis (i.e. find the focus point of the specimen in a fixed position on the XY plane).

3.4.1   XY-plane Submodule

Composed by 2 parts that slide perpendicularly between each other on the XY plane (see Figure 3.6.A). This submodule moves the μStage to different XY positions, in order to obtain distinct microscopic fields of the specimen. Two servo motors are used to provide the movement, together with small elastic bands that ensure the movement in both ways. It should be noted that this arrangement is not linear, since the servo movement is provided in a 90° arc. Nevertheless, it allows the acquisition of different microscopic fields, particularly by moving one of the servos while the other remains static. Taking into account that repositioning to a specific microscopic field location

with high precision is usually not required in microscopic blood smear analysis, this module is not required to perform high precision and resolution displacements. Covering a high number of distinct microscopic fields from different XY positions is by far much more important, in order to obtain a reliable overview of the specimen.
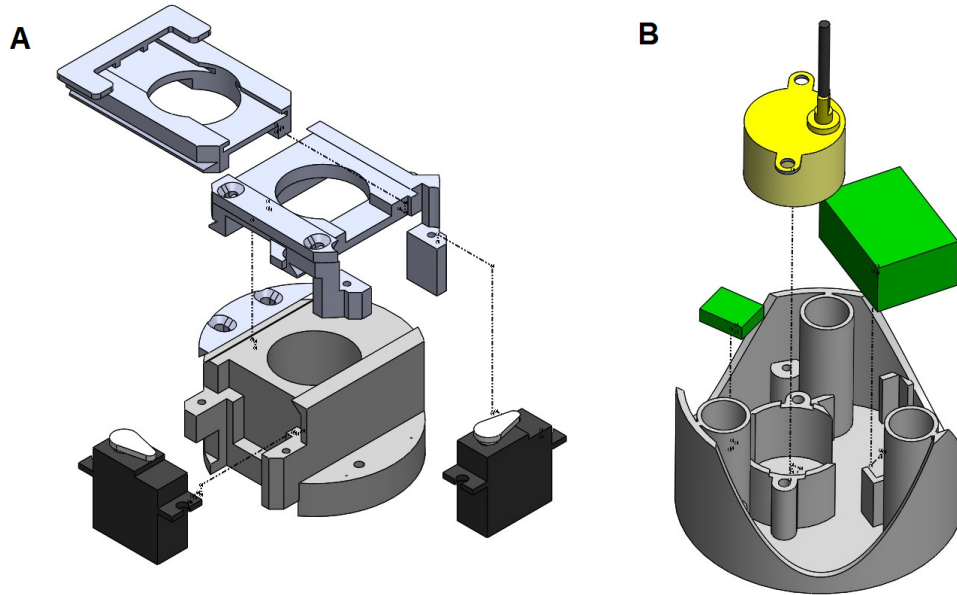
Figure 3.6: μStage functional submodules: (**A**) Exploded view of the XY-plane submodule, with servo motors (at black); (**B**) Exploded view of the Z-axis submodule, with step motor (at yellow) and electronics (at green).

3.4.2 Z-axis Submodule

Composed by 3 tubular structures that slide against their negatives in the base part (see Figure 3.6.B). This submodule allows the vertical movement of the μStage, in order to find the Z-axis position that corresponds to the focus point of the specimen. A simple stepper motor is used to provide the vertical movement, being the rotary movement of the stepper engine translated to linear motion through a threaded rod and a nut fixed in this part. Moreover, the base part of this submodule is also used to fix the electronic board, the Z-axis actuator and the μUSB connector.

The correct calibration and parameterization of the 3D-printer is evidently important for all μSmartScope printed components, but particularly crucial for this submodule. Obtaining the required gap between each tubular structure and the corresponding negative is mandatory to achieve precise Z-axis displacements. Being the μStage the bottleneck of the previously reported version, two major mechanical changes were made in order to improve the performance of the Z-axis submodule in terms of precision and stability:

- **M2 threaded rod**: The previous version of the μStage used a M3 threaded rod with a coarse thread. After extensive testing, we concluded that a higher resolution in the Z-axis movement was required in order to reach the ideal Z position where the specimen is completely focused.

For that purpose, we switched to a M2 threaded rod with coarse thread, which theoretically improves the resolution from 0.5 mm to 0.4 mm per revolution. The usage of a M3 rod with fine pitch was discarded due to its low availability and prohibitive cost. It is worth noting that the usage of the M2 thread brings the disadvantage of a lower shaft diameter, so we ensured through calculations that the µStage would not fail under the expected load stress.

- **Buckling cover**: A good mechanical design practice known to improve the stability of sliding mechanisms was incorporated, which consists on ensuring that each tubular stem should have more than the double of its diameter inside of the outer stem at its maximum Z position [8]. Consequently, the tubular structures that slide against their negative in the base part were redesigned accordingly.

3.4.3 Electronics

The power board was designed to power the 3 actuators (one stepper and two servos) and the illumination LED, using exclusively the power from a USB connection with 5V and 500 mA. It should be noted that most of the currently available smartphone models have USB-OTG interface in order to allow the connection of USB peripherals. To be fully compatible with the µSmartScope, the used smartphone model needs to support this power standard, otherwise it will not be capable of powering the µStage. An image of the developed PCB can be observed in Figure 3.7, and the electronic system is composed by:

- **Stepper motor**: The used stepper motor is a 28BYJ-48 5V, which is the cheapest stepper motor found in common electronic stores. This was a major point in choosing the motor, since the replication of the µSmartScope should be easy and cheap in any part of the world. It is controlled by a DRV8836 from Texas Instruments with current limited to 200 mA, and capable of 512 steps per full rotation. Since we are using a standard M2 threaded rod, we have a theoretical resolution of around 0.78 μm. Furthermore, a simple push-button switch is placed in the Z axis to provide a way to locate the position when the device is turned on.
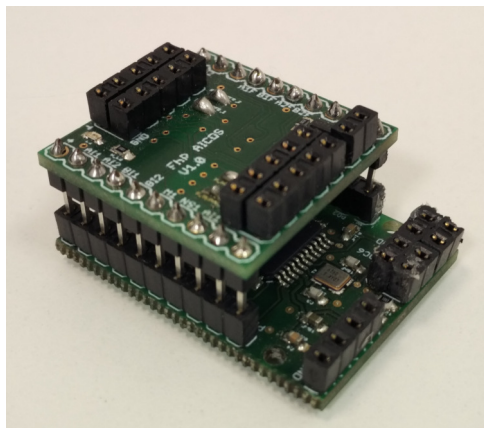
Figure 3.7: Prototype PCB to control the µStage. [52]

- **Two servo motors**: The used servo motors are the Hitec HS-55 5V, which is the cheapest
  micro servo motor found in common electronic stores. Controlled directly by PWM output
  and limited to 200 mA, their rotation is directly used to generate the linear movement. The
  servo head has a size of 13 mm meaning that this is our maximum displacement. Using the
  90° travel with 2.5° per step, we have 36 steps available while we only need 10 per axis;

- **Illumination**: Since the illumination depends of the specimen under analysis, the control
  board provides an output based in a power Mosfet capable of providing 150 mA at 5V. This
  power can be controlled by changing the PWM duty cycle of the output.

- **Control**: An ATMega32u4 is used to control all the logic of the system, which contains
  native USB communications and plenty of GPIO ports and PWM support. The native USB
  connection is seen as a serial port in the smartphone using the *USB serial for Android*
  library [68]. Moreover, an API for Android was developed to allow interaction with the
  stage. This API was made to be as simple as possible to integrate in any app, providing every
  function needed to fully control the stage (i.e. stepping in X, Y and Z axes, as well as control
  the LED light).

3.5 Automated Focus

The traditional focusing method in microscopy is usually achieved by manually adjusting the
vertical position of the microscope stage, with the objective of obtaining a focused microscopic
field. However, for screening processes that requires the analysis of a huge amount of microscopic
fields per specimen, this process clearly becomes a cumbersome task. As an illustrative example,
for the analysis of malaria-infected blood smears, it is recommended the analysis of 100 distinct
microscopic fields for a single specimen. The specialist is even advised to rest regularly, so human
errors can be avoided and high performance rates ensured. To tackle this problem, our solution takes
advantage of the developed motorized automated stage (see Section 3.4) and real time feedback
retrieved from the smartphone camera sensor. But in order to obtain a fully automated solution,
we soon realized that we had to develop an automated focus approach that ensures autonomous
acquisition of focused microscopic fields.

Automated focus is a long standing topic in the literature, and several focus algorithms have
been proposed [35, 54]. However, the search for the proper algorithm still remains an open topic,
since it can highly depends on the visual characteristics of the specimen and characteristics of the
camera sensor. Generally, an autofocus system includes three main components: i) **Focus Region
Selection**; ii) **Focus Measurement**; and iii) **Focus Point Search Logic**. In this section we present
a detailed description of those components in our approach, with the final goal of obtaining focused
microscopic images from malaria-infected thin and thick blood smears without human interaction.
As a side note, we opted to use these two types of specimen preparation because they represent
quite well two different extreme scenarios in microscopy analysis: the thin usually presents dense

concentration of visible structures in each microscopic field (see Figure 3.8.A), while the thick smear presents a low number of visible structures (see Figure 3.8.B).

3.5.1 Focus Region Selection

Due to lens constrains, it is not possible to obtain maximal focus in the whole area of the microscopic field. Therefore, a square region in the center of the preview image was defined, which generally is the place where distortion interference is lower (see Figure 3.8). This square region will be used by the focus algorithm to extract the metrics and make decisions accordingly.
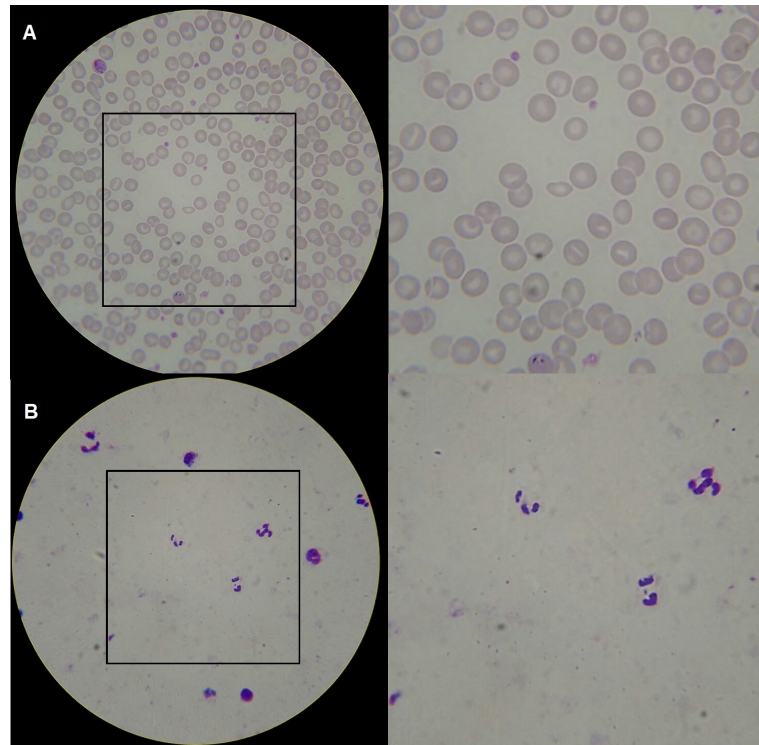
Figure 3.8: Focused image obtained using the μSmartScope, and respective central square resulting from focus region selection: (**A**) Thin blood smear; (**B**) Thick blood smear.

3.5.2 Focus Measurement

Taking into consideration several works on the literature targeting the automatic focus for microscopic devices using image processing, in this work we tested and compared a wide range of focus metrics already proposed that were considered highly relevant for automatic focusing. In detail, we tested: derivative-based as the Brenner gradient and the Tenenbaum gradient; statistics based, like the normalized variance; histogram-based, as entropy; and intuitive algorithms, like thresholded content [57, 36].

After this comparative analysis, the Tenenbaum gradient [62] standard deviation ($TENG^{STD}$) and sum ($TENG^{SUM}$) were considered the most discriminative focus metrics, i.e. the metrics that allows better differentiation of the ideal focus point. The Tenenbaum gradient is obtained

by convolving the previously selected central square of the image with Sobel operators, and by summing the square of gradient vector components:

$$TENG = (G_x(i,j)^2 + G_y(i,j)^2), \tag{3.2}$$

where G_x and G_y are the horizontal and vertical gradients computed by convolving the focus region image with the Sobel operators.

Despite the remarkable discriminative power of $TENG^{STD}$ and $TENG^{SUM}$ metrics, in this work we started by testing the previous proposed automated focus approach [52] not only on a wide range of smartphone models, but also on different thin and thick blood smears. After extensive testing, we concluded that improvements to the previously proposed approach were required, mainly because the order of magnitude of the $TENG^{STD}$ and $TENG^{SUM}$ metrics presented a significant variation for different smartphone-specimen combinations. We concluded that this pronounced variation was being cause by two main factor: i) images of the same specimen captured with different smartphone models may present different image characteristics (e.g. high variation in image contrast and/or color representation) due to the different camera sensor specifications; and ii) microscopy specimen preparation greatly depends on good-quality reagents and proper human skills, which can lead to huge intensity variations of the stained components.

Despite this shifting behavior, we noticed however that the relative variation of both metrics was considerably more homogeneous when compared with the respective absolute values. So instead of using directly the $TENG^{STD}$ and $TENG^{SUM}$ metrics values, we used the following slope gradients:

$$SLOPE_{ij}^{STD} = \frac{(TENG_i^{STD} - TENG_j^{STD})}{i - j}, \tag{3.3}$$

$$SLOPE_{ij}^{SUM} = \frac{(TENG_i^{SUM} - TENG_j^{SUM})}{i - j}, \tag{3.4}$$

where i and j are two different Z-axis positions, with $i, j = \{0, 1, ..., Z^{MAX}\}$, being Z^{MAX} the highest Z-axis position reachable by the μStage.

3.5.3   Focus Point Search Logic

The focus point search logic aims to identify the Z-axis position where the specimen is ideally focused. In order to simplify the explanation and abstract the vertical displacement of the μStage from SI units, a scale from 0 to 7000 was create to represent the possible Z-axis coordinates. In fact, each unit on this scale represents the minimum step allowed by the stepper motor, so taking into account that the stepper motor allows 512 steps per revolution, we can state that the μStage is surely over the specimen focus point after $\sim$13,67 revolutions. The proposed approach can be divided in two main phases, the Rough phase and the Precise phase, according to the following steps:

1. The algorithm starts in the Rough phase, where the goal is to detect a pronounced increase of the focus metrics $SLOPE_{ij}^{STD}$ and $SLOPE_{ij}^{SUM}$, which corresponds to the beginning of the visualization of the microscopic structures. At the beginning of the Rough phase, the μStage is on the bottom Z-axis position ($Z^{Pos} = 0$), which from now on will be called the reset position (Z^{Reset}).

2. While the μStage is on Z^{Reset}, the user inserts the microscopic slide and gives an order through the mobile application to start the image acquisition process. The μStage starts autonomously ascending in the Z-axis to a specific Z position ($Z^{Pos} = 5000$), which from now on will be called the initial position ($Z^{Initial}$). The μStage is surely below the focus point at $Z^{Initial}$, so no focus metrics are computed until this position is reached.

3. When the $Z^{Initial}$ is reached, the μStage starts ascending on specific intervals ($Z_{Step}^{Interval} = 2$). For each $Z_{Step}^{Interval}$, the image preview obtained with the smartphone camera sensor is used to compute the $SLOPE_{ij}^{STD}$ and $SLOPE_{ij}^{SUM}$ focus metrics. It should be noted that in the Rough phase we use a frame rate of 20 frames per second (fps).

4. The transition from the Rough phase to the Precise phase occurs when the following condition is verified: $SLOPE_{ij}^{STD} > 20$ and $SLOPE_{ij}^{SUM} > 20$.

5. When the Precise phase is reached, the μStage keeps ascending with the same $Z_{Step}^{Interval}$, but we decrease the frame rate to 4 fps. This adjustment is directly related with the vibration caused by each mechanical step, which consequently causes motion blur on the image preview. By guaranteeing more time between the mechanical movement and the analysis of the preview image, we ensure that the vibration dissipates and the computation of the focus metrics is not affected by that artifact.

6. During the Precise phase, the $TENG^{STD}$ is computed on the preview image for each $Z_{Step}^{Interval}$. If the $TENG^{STD}$ of the current Z position has the highest value found on the Precise phase, this position is considered the best candidate to focus point. When that happens, an image is captured with 5 Megapixels and saved on the smartphone memory. In the event of an higher $TENG^{STD}$ value for a posterior Z position, a new image is captured and the best candidate to focus point is updated.

7. The focus point search logic ends with successful state when a candidate to focus point was found and: i) the $TENG^{STD}$ presents always lower value in the following 20 $Z_{Step}^{Interval}$ positions; or ii) the $TENG^{STD}$ has a value lower than half of the best candidate $TENG^{STD}$ in any of the following $Z_{Step}^{Interval}$ positions;

8. The focus point search logic ends with fail state if the maximum Z-axis position ($Z^{Pos} = 7000$) is reached without a single candidate to focus point. In the event of fail state, a reset procedure

takes place: i) the μStage descends to the Z^{Reset} position; ii) the μStage moves to a different position in the XY plane; and iii) the focus point search logic described above is restarted. After extensive testing, we noticed that the most common cause for the occurrence of a fail state is usually the low number of microscopic structures in that specific XY position.

The behavior of the proposed focus point search logic is illustrated on Figure 3.9, where is depicted the variation of the $SLOPE_{ij}^{STD}$ and $SLOPE_{ij}^{SUM}$ while the μStage is ascending in the vertical axis.
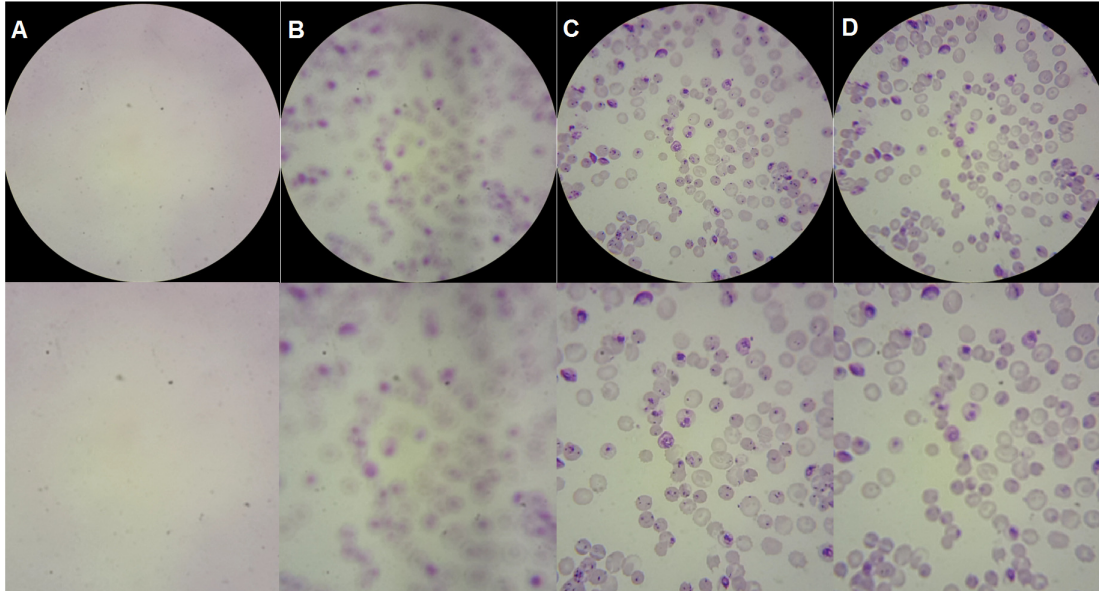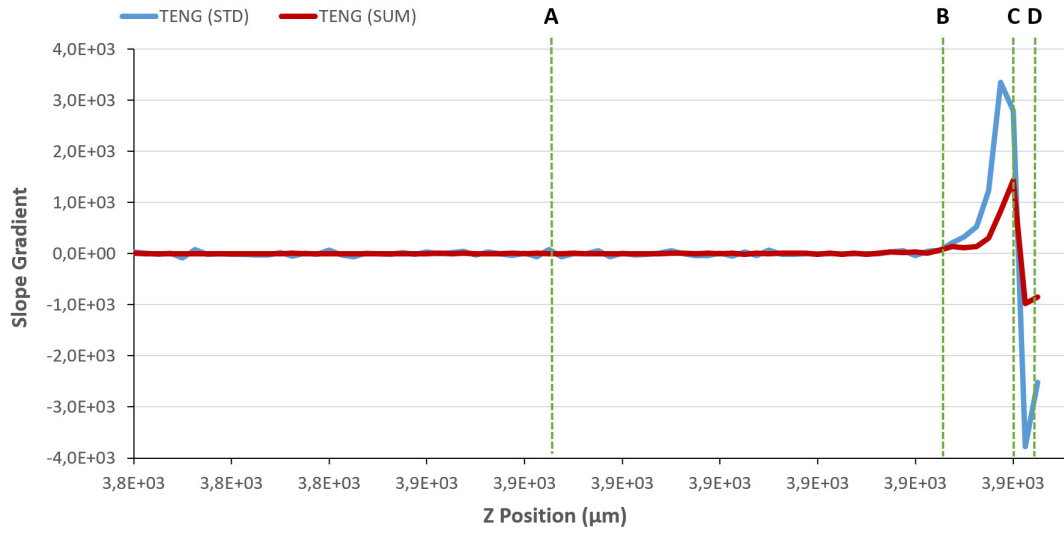
Figure 3.9: Variation of the Tenenbaum focus metrics while the μStage is ascending in the vertical axis. Illustrative examples of preview images obtained by the smartphone camera at different Z positions are presented: (**A**) During the Rough phase; (**B**) Entering the Precise phase; (**C**) Focus point; (**D**) Stopping condition after focus point detected.

3.6 Results and Discussion

In this section we start by presenting the obtained results in terms of resolution, field of view and illumination of the images acquired using the μSmartScope. Moreover, we also evaluated the μStage performance regarding the precision and resolution of the mechanical movement, as well as the power consumption. We finish this section with a detailed analysis of the proposed automated focus approach, covering the usage of a wide range of smartphone models and different thin and thick blood smears.

3.6.1 Resolution

The magnified images of the smears obtained with the μSmartScope must have an appropriate resolution over a sufficiently large area, so a conclusive decision about the presence of a specific infectious agent can be made. The 1951 USAF resolution test chart is a resolution test pattern conforming to MIL-STD-150A standard, set by US Air Force in 1951. It is still widely accepted to test the resolving power of optical imaging systems such as microscopes, cameras and image scanners. One example is the READY OPTICS USAF 1951 Microscope Resolution Target, which is a target embedded in a standard microscope slide, suitable for oiled objectives and oiled condensers. In terms of resolution, the target allows to check a minimum spacing between lines of 0.197 nm.

Microscopic images of the READY OPTICS USAF 1951 Microscope Resolution Target with 1000x magnification were acquired the μSmartScope and with the Bresser Microscope-5102000-Erudit DLX (see Figure 3.10). Both systems use similar objectives and eyepieces, so the main goal is to evaluate image resolution of the μSmartScope.
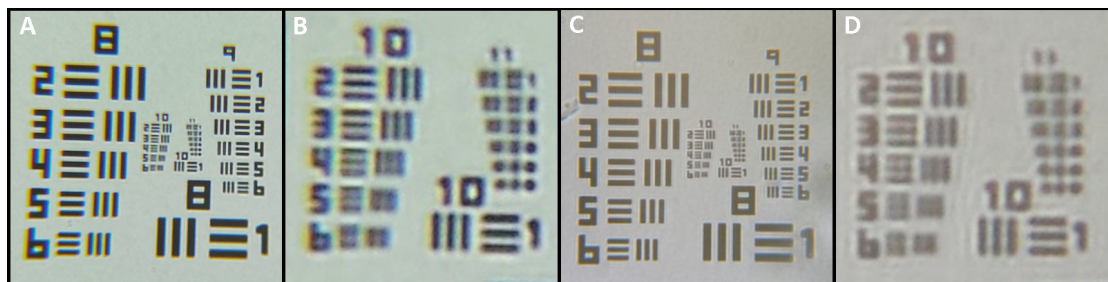
Figure 3.10: Images of READY OPTICS USAF 1951 microscope resolution target: (**A**) Acquired using Bresser Microscope-5102000-Erudit DL; (**B**) Detail of Group 10 using the Microscope; (**C**) Acquired using the μSmartScope; (**D**) Detail of Group 10 using the μSmartScope. [52]

To determine the resolution of the μSmartScope and compare it to the resolution of the Bresser commercial microscope, the images acquired with the separate systems were converted to grayscale and the analysis focused on Group 10, which was the smallest resolvable group. In order to determine the smallest resolvable Element of Group 10 in both horizontal and vertical orientations, the images were firstly converted to grayscale and a line for each of the 6 bars of that Element were drawn. Each line starts and ends in a background pixel, and intersects perpendicularly the respective bar. All pixel values of each line were used to calculate the Michelson contrast, which

was assigned to the respective bar. In both directions of each Element, the bar with minimum
Michelson contrast was selected for analysis purposes (see Figure 3.11).
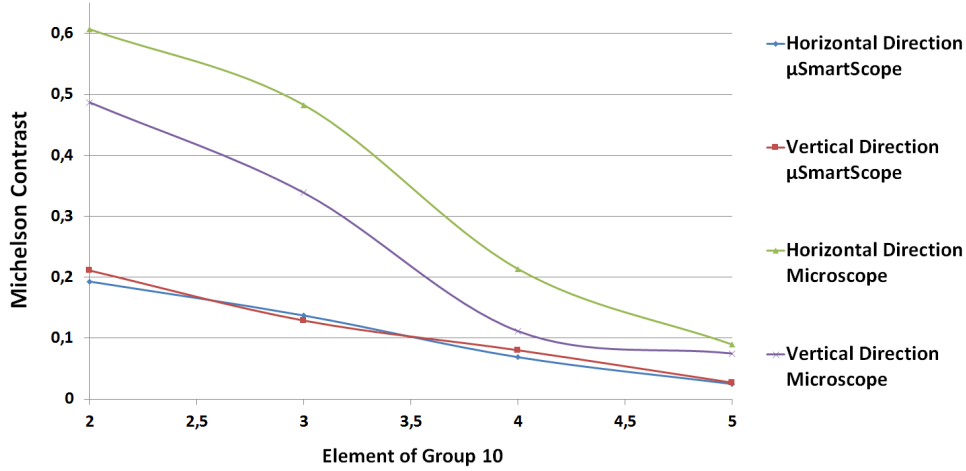
Figure 3.11: Minimum Michelson contrast for USAF Resolution Target Elements of Group 10. [52]

It was defined that an Element is considered resolvable on a particular direction if the minimum
Michelson contrast was ≥ 0.1. Thus, Element 3 was defined as the minimum resolvable Element
for the μSmartScope, which gives a minimum resolution of 0.388 μm on both directions. For the
Bresser commercial microscope, Element 4 was selected as the minimum, which corresponds to a
resolution of 0.345 μm for both directions. Although the μSmartScope presents a slightly lower
resolution, it is clear on Figure 3.11 that both directions have a more homogenous behavior in terms
of resolution, while in the Bresser microscope there is an evident discrepancy between the resolving
power on different directions. The lower values of Michelson contrast for the μSmartScope might
be caused by the limitation in terms of the maximum power rate of the smartphone, since both the
illumination and motorized automated stage must be powered by USB-OTG. Thus the power that
feeds the LED is limited, which diminishes the intensity of the LED and consequently the image
contrast.

3.6.2 Field of View

Resolution and field of view are inversely linked in standard laboratory microscopes. In order to
obtain microscopic fields with both high magnification and resolution, the usage of objectives with
higher numerical aperture is required, which results in smaller Field of Views (FOV) [45]. To
determine the FOV of the μSmartScope, images of the READY OPTICS USAF 1951 Microscope
Resolution Target were acquired and used to estimate the microns to pixels (μm/pixel) relationship.
The exact distances between bars of a specific Element is given by the specifications of the resolution
target, particularly Element 2 and 3 of Group 8 corresponds to 1.740 μm and 1.550 μm, respectively.
By measuring the number of pixels between bars of this 2 Elements on the acquired image, a
relationship of 0.085 μm/pixel was obtained for Element 2 and 0.084 μm/pixel for Element 3. So
we considered the average value, i.e. a relationship of 0.0845 μm/pixel. Furthermore, the number

of pixels for the vertical and horizontal axis that passes through the center of the visible optical circle of the acquired image were determined. These values were then combined with the previously calculated μm/pixel relationship, in order to estimate the FOV of the visible optical circle, which resulted in a FOV of 214.38 μm and 206.87 μm for the vertical and horizontal axis, respectively.

3.6.3 Illumination

In order to evaluate the uniformity of the illumination of the LED coupled to the proposed condenser, an image was acquired with a blank microscope slide (see Figure 3.12.A). A diagonal line scan starting on the top right corner of the image was defined, in order to evaluate the variation of the pixels intensity along this line. Particularly, a total of 200 pixel boxes were considered along the scan line, being each box equally spaced and with a size of 10x10 pixels. The mean and standard deviation of the pixels intensity was computed for each box, as depicted in Fig 3.12.B and 3.12.C. This results demonstrate that the proposed illumination set up ensures substantially uniform illumination with low noise, being the small intensity variations probably caused by dust particles on the lenses or components floating in the immersion oil.
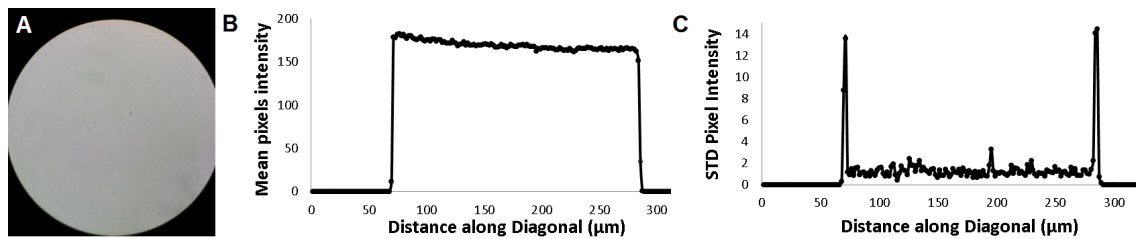
Figure 3.12: μSmartScope illumination uniformity analysis: (**A**) Original image; (**B**) Mean pixel intensity of the 10x10 pixel boxes on the diagonal direction; (**C**) Standard deviation of the 10x10 pixel boxes on the diagonal direction. [52]

3.6.4 μStage Performance

The μStage performance was evaluated in terms of precision and resolution of the mechanical movement, particularly in terms of the horizontal (XY plane) and vertical (Z axis) directions independently. Moreover, an analysis of the power consumption of the μStage is also presented.

3.6.4.1 Precision and Resolution

Before analyzing the mechanical movement of the μStage, it should be taken into account the design option of minimizing the usage of mechanical components and give priority to 3D-printed parts, in order to reduce costs and ensure an easy replication of the prototype. Despite the referred advantages, we were aware that using moving parts fully 3D printed might lead to a potential losses in the movement precision, for instance caused by plastic imperfections and/or particles in the sliding portions. Thus, the goal of this section is to measure and assess if the precision and resolution in the mechanical movement offered by the μStage is comparable with conventional

microscopy analysis. In Figure 3.13 we present the results for the mechanical movement of the μStage in the XY plane and Z axis. Particularly, for each direction we performed 100 steps and the respective displacement was measured using a digital caliper (Mitutoyo Absolute) with resolution of 0.01 mm ± 0.02 mm.
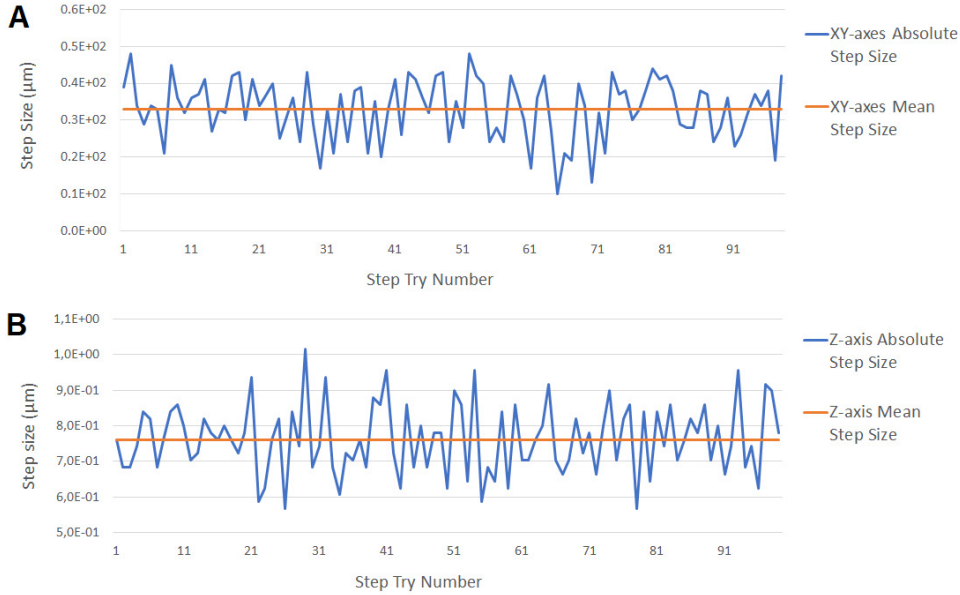
Figure 3.13: Measured step size values after 100 repetitions: (**A**) XY plane; (**B**) Z axis.

For the displacement in the XY plane, a clear variation of the step size is depict in Fig 3.13.A. This behavior is probably caused by two main factors: i) the non-linear movement of the servo; and ii) imperfections on the sliding parts that are a consequence of the 3D printing process. Nevertheless, we obtained an average displacement of 330 μm with a standard deviation of 81 μm, a result that attests the suitability of the μStage XY-plane movement for microscopy analysis purposes. As referred before, repositioning to a specific XY position with high precision is usually not required in conventional microscopy analysis, being much more important the coverage of a high number of different XY positions. Please note that the obtained XY μStage displacement is marginally higher than the FOV determined in section 3.6.2, which means that we are obtaining a new microscopic field every time we take a XY step.

Regarding the displacement in the Z axis, it should be taken into account that our caliper is not able to measure such small steps. To estimate the average step size, one full revolution of the motor was considered (which corresponds to 512 steps), and the respective displacement was measured 100 times. This distance was then divided by the number of steps, in order to estimate the travel of a single step. As we can see in Fig 3.13.B, the steps are less dispersed, but some variability is still verified. Each step corresponds to an average of 0.763 ± 0.098 μm, which gives an indication that our steps in the Z axis are within the theoretical values. By comparing these results with the previously reported performance of 0.98 ± 0.18 μm [52], it becomes clear the major impact of the mechanical improvements performed in this work.

3.6.4.2   Power Consumption

In order to ensure that we never go over the maximum power rate of the smartphone, the whole system power consumption is always under 400 mA at 5V. This is achieved by allowing only one actuator moving at any given time. In Table 3.1, the power consumption of the system can be observed together with the autonomy for two different smartphone models. The profile tested was as close as possible to the real one, i.e. the smartphone was continuously acquiring focused microscopic fields at different XY positions, with the screen turned off and in flight mode until it shut down due to low battery.

It is worth noting that we are currently using the smartphone battery to simultaneously power the actuators of the μStage, the LED light, acquire data continuously with the camera sensor and process each acquired frame for the automatic focus of the smear. Considering the current battery capacity of smartphones, this obviously represents a huge burden in terms of power consumption, and it is clear that the current autonomy of the system is low for a day of continuous use. As an alternative, we envision the usage of a power bank coupled to a OTG splitter cable, which we aim to include in the next version of the μSmartScope system.

Table 3.1: Power consumption test results. [52]

Smartphone	Average Current (mA)	Average Power Consumption (W)	Autonomy (min)
Samsung Galaxy S5	208.64	1.043	164
LG Nexus 5	201.34	1.006	149

3.6.5   Automated Focus

In order to evaluate the proposed automated focus approach, we used 9 different blood smears and 5 different smartphone models, which gave a total of 45 different smartphone-specimen combinations. The automated focus test procedure consisted on the acquisition of 100 images for each smartphone-specimen combination, i.e. 4500 focused images were acquired without any human interaction. Two different types of specimens were used: 5 thin blood smears and 4 thick blood smears. As mentioned before, we opted to use these two different types of specimen preparations because they represent quite well two different extreme scenarios we might encounter: the thin blood smears usually presents dense concentration of visible structures in each microscopic field, while the thick blood smears have a low number of visible structures. The average image acquisition time per smartphone-specimen combination is depict on Tables 3.2 and 3.3.

Table 3.2: Average seconds per image for different smartphone models and thin blood smears, calculated over 100 automated focus attempts for each combination.

Thin blood smears	Seconds per image (average time over 100 automated focus attempts)				
	Asus Zenfone 2	HTC One M8	Motorola Moto G5	LG Nexus 5	Samsung Galaxy S6
Slide #1	11.30	8.50	8.39	9.04	7.46
Slide #2	10.76	7.39	8.11	7.37	6.58
Slide #3	10.45	7.25	8.12	7.77	6.99
Slide #4	11.85	7.15	7.95	8.14	7.16
Slide #5	9.21	7.74	7.99	8.11	6.86

Table 3.3: Average seconds per image for different smartphone models and thick blood smears, calculated over 100 automated focus attempts for each combination.

Thick blood smears	Seconds per image (average time over 100 automated focus attempts)				
	Asus Zenfone 2	HTC One M8	Motorola Moto G5	LG Nexus 5	Samsung Galaxy S6
Slide #1	17.09	18.19	8.76	16.54	23.93
Slide #2	16.49	12.60	13.56	11.49	8.80
Slide #3	13.85	15.24	8.81	10.15	6.64
Slide #4	13.24	9.77	14.64	11.68	8.21

These results corresponds to an average of 8.31 ± 1.41 and 12.98 ± 4.20 seconds per image, for thin and thick blood smears, respectively. Taken into account that on a previous work we reported a performance of 80 seconds per image [52], this major performance boost clearly illustrates the benefits of the mechanical and software improvements proposed on this work.

Particularly, by testing the μSmartScope on such a wide range of smartphone-specimen combinations, we validated that our results were not biased towards a specific specimen type (e.g. amount microscopic structures or staining condition) or specific camera sensor characteristics (e.g. resolution, exposure or white-balancing mode). This good adaptability to different smartphone-specimen combinations conditions is illustrated on Figures 3.14 and 3.15.
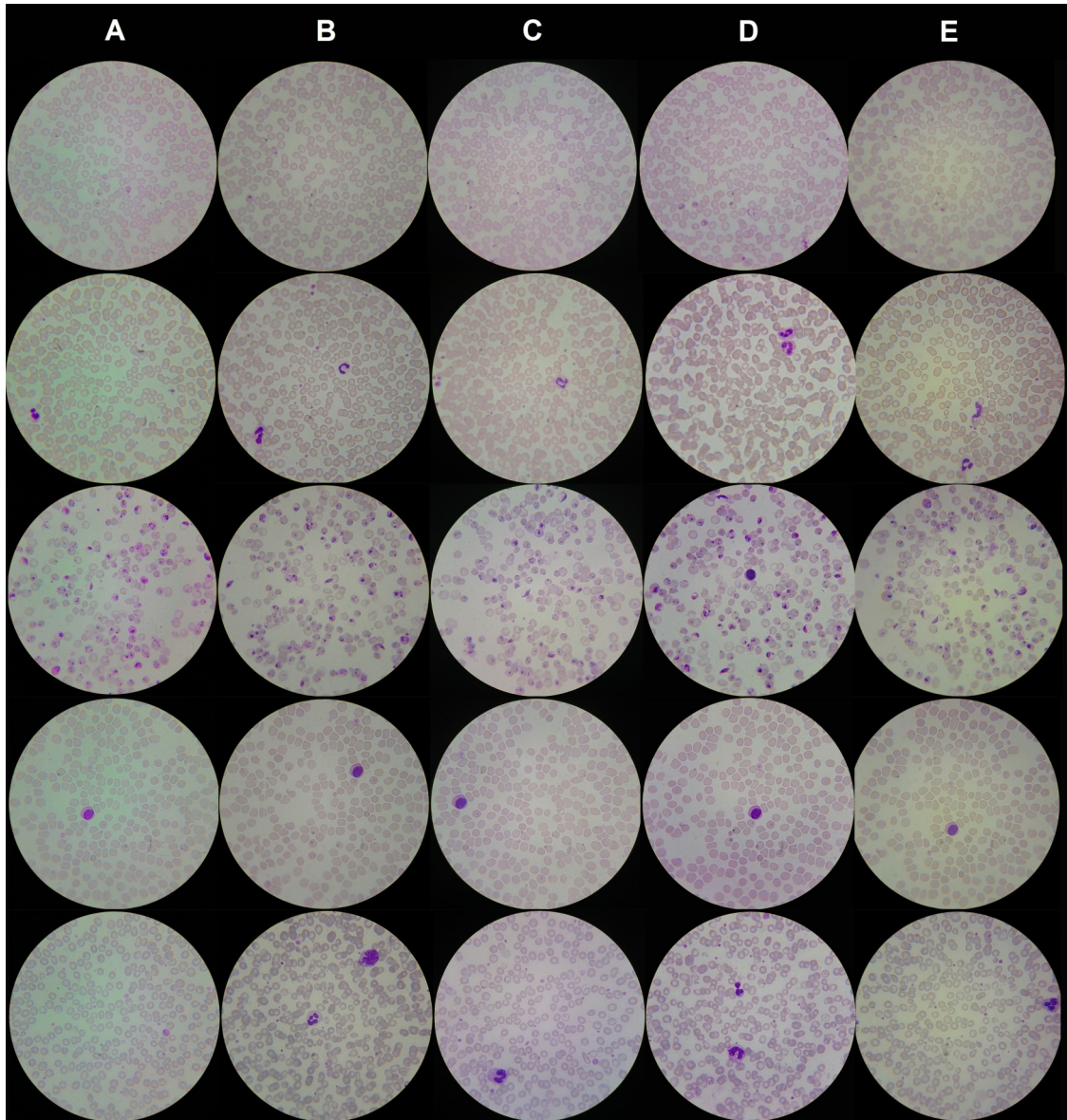
Figure 3.14: Illustrative examples of focused images autonomously acquired with the μSmartScope and different smartphone models for 5 different malaria-infected thin blood smears: (**A**) Asus Zenfone 2; (**B**) HTC One M8; (**C**) Motorola Moto G5; (**D**) LG Nexus 5; (**E**) Samsung Galaxy 6.

3.6.6 Applicability Examples

The μSmartScope was used to acquire microscopic images of reference blood smears with different parasites, which are responsible for the most relevant NTDs that can be detected through microscopic examination (see Fig 3.16). Particularly, the following smears were used: thick blood smear infected with malaria parasites (*P.falciparum* species); thin blood smear infected with malaria parasites (*P.ovale* and *P.malariae* species); thin blood smear infected with Chagas parasites (*Trypanosome cruzi* species); and thick blood smear infected with Lymphatic Filariasis parasites (*Brugia malayi* and *Wuchereria bancrofti* species).
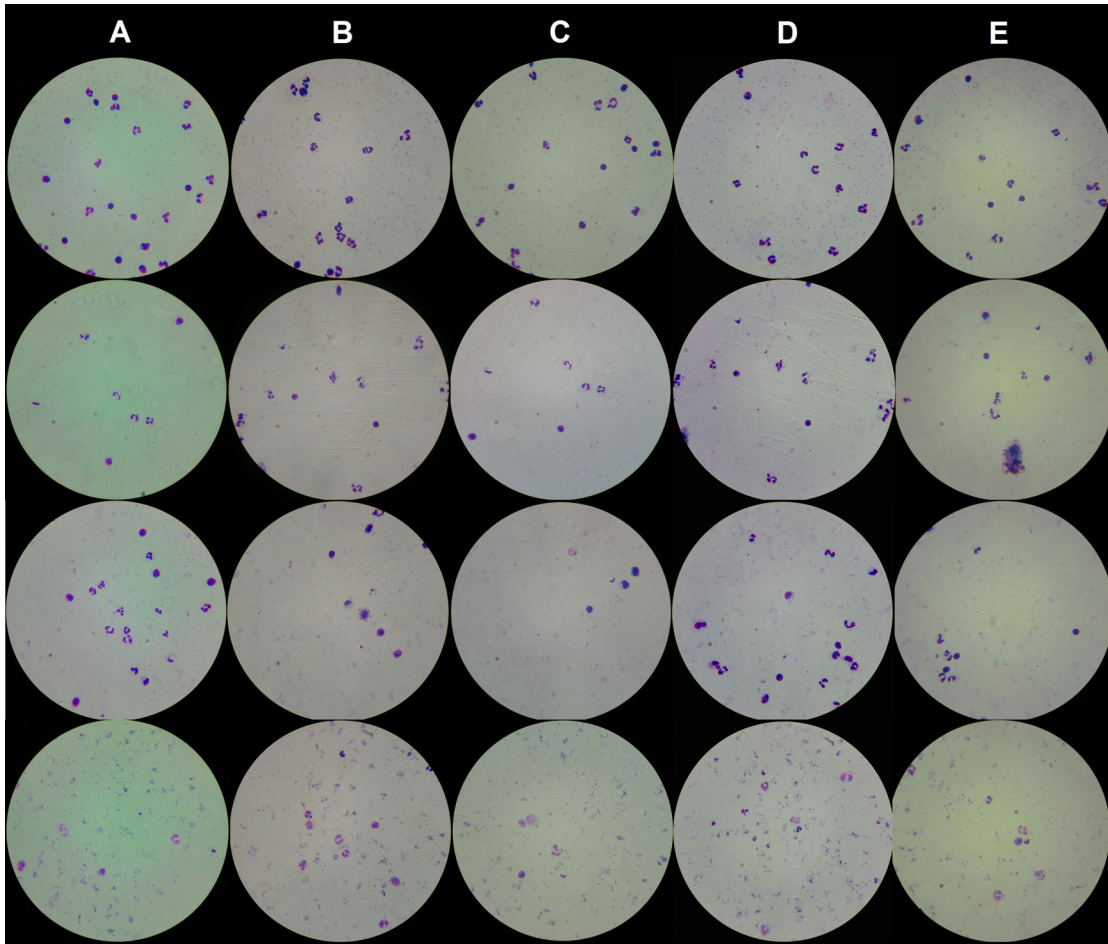
Figure 3.15: Illustrative examples of focused images autonomously acquired with the *μ*SmartScope and different smartphone models for 4 different malaria-infected thick blood smears: (**A**) Asus Zenfone 2; (**B**) HTC One M8; (**C**) Motorola Moto G5; (**D**) LG Nexus 5; (**E**) Samsung Galaxy 6.

Furthermore, to highlight the versatility of the developed system, a liquid-based Pap smear with high grade squamous lesions was also tested, which is associated with precancerous changes and high risk of cervical cancer. For the analysis of this smear, a magnification of 400x is required, so we had to adapt the optical set up of the *μ*SmartScope, which consisted in the simple procedure of changing the Bresser Planachromat 100x oil-immersion objective for the Bresser Planachromat 40x (Bresser #5941540).

To finalize, considering the acquired images and the feedback received by the specialists that helped us collect the smears, we can state that very promising results were obtained. For all the tested smears, the detection of the considered blood parasites and the precancerous cells on the cervix was considered possible through images acquired via the *μ*SmartScope.
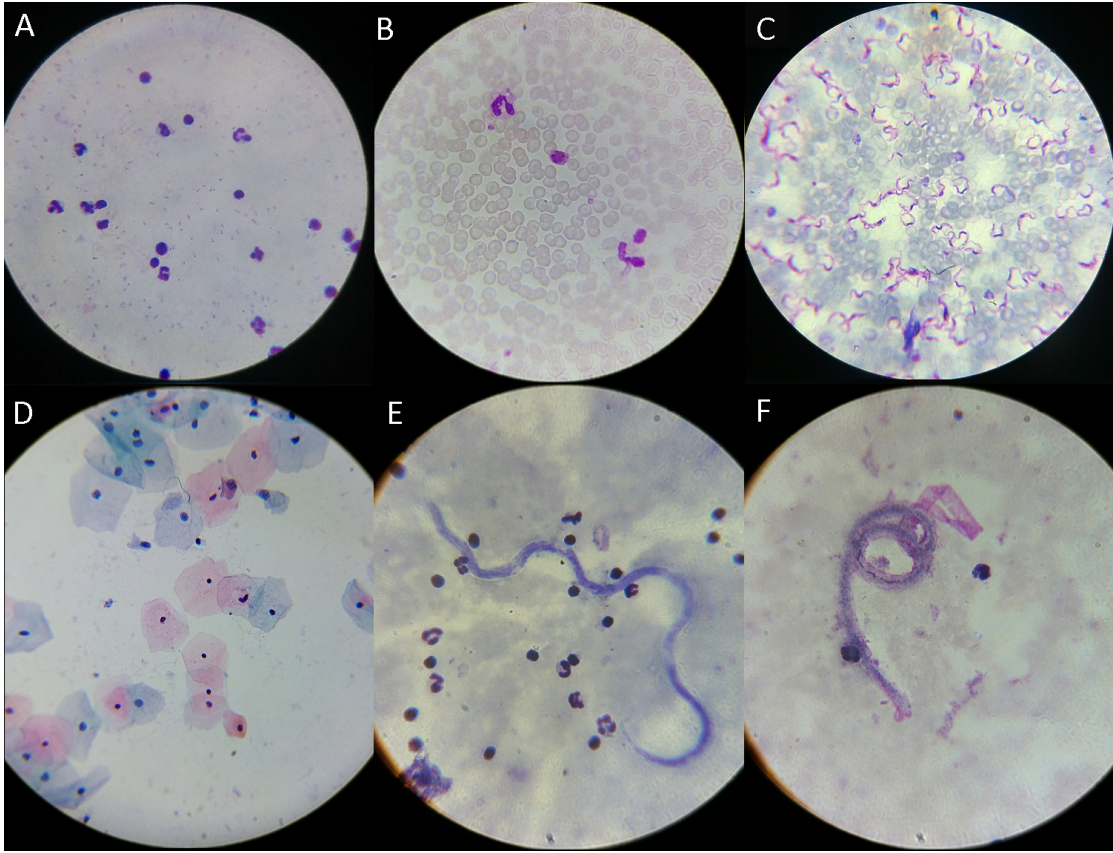
Figure 3.16: Images of different smears acquired with the μSmartScope: (**A**) Thick blood smear infected with malaria parasites (*P.falciparum* species); (**B**) Thin blood smear infected with malaria parasites (*P.ovale* and *P.malariae* species); (**C**) Thin blood smear infected with Chagas parasites (*Trypanosome cruzi* species); (**D**) Liquid-based Pap smear with high grade squamous lesions; (**E**) Thick blood smear infected with Lymphatic Filariasis parasites (*Brugia malayi* species); (**F**) Thick blood smear infected with Lymphatic Filariasis parasites (*Wuchereria bancrofti* species). Images (A), (B) and (C) were acquires with a LG Nexus 5, while images (D), (E) and (F) with a Samsung Galaxy S5. All images were acquired with magnification of 1000x, except image d) which has magnification of 400x. [52]

3.7 Conclusions and Future Work

In this chapter we report our most recent advances towards the development of a fully automated 3D-printed smartphone microscope with a motorized stage (μSmartScope). This prototype is the first proposed smartphone-based alternative to conventional microscopy that allows autonomous acquisition of a pre-defined number of images at 1000x magnification with suitable resolution, by using a motorized automated stage fully powered and controlled by a smartphone, without any human interaction.

All the components of the proposed device are described and properly evaluated. In terms of the optical module, a minimum resolution of 0.388 μm was determined, with a FOV of 214.38 μm and 206.87 μm for the vertical and horizontal axis that passes through the center of the visible optical circle, respectively. Regarding the illumination module, the LED light coupled to the proposed

condenser demonstrated to achieve an uniform illumination suitable for brightfield microscopy. The developed motorized automated stage (μStage) achieved an average resolution of 330 ± 81 μm for the XY plane steps and an average resolution of 0.763 ± 0.098 μm for the Z-axis steps, results that validates its effective usage for microscopy analysis. Moreover, the proposed automated focus approach was evaluated on 9 different blood smears and 5 different smartphone models, achieving an average performance time of 8.31 ± 1.41 and 12.98 ± 4.20 seconds per image, for thin and thick blood smears, respectively.

Several smears infected by different blood parasites responsible for the most relevant neglected tropical diseases were used to test the device. The acquired images showed that it was possible to detect those agents through images acquired via the μSmartScope, which clearly illustrate the huge potential of this device, specially in developing countries with limited access to healthcare services. As future work, we want to test the performance and assess the practical usefulness of the μSmartScope on field trials. Particularly, the μSmartScope will represent a component of a mobile-based framework for malaria parasites detection currently being developed. Thus, we aim to integrate this prototype into the referred framework, with the ultimate goal of creating a system that: (i) provides an effective pre-diagnosis of malaria in medically-underserved areas; (ii) is low cost and mobile based; (iii) is easy to use, even for non-experts in microscopy.

Chapter 4

Automated Detection of Malaria Parasites on Thick Blood Smears via Mobile Devices

Luís Rosado, José M. Correia da Costa, Dirk Elias and Jaime S. Cardoso

Abstract

An estimated number of 214 million cases of malaria were detected in 2015, which caused approximately 438 000 deaths. Around 90% of those cases occurred in Africa, where the lack of access to malaria diagnosis is largely due to shortage of expertise and equipment. Thus, the importance to develop new tools that facilitate the rapid and easy diagnosis of malaria for areas with limited access to healthcare services cannot be overstated. This chapter presents an image processing and analysis methodology using supervised classification to assess the presence of *P.falciparum* trophozoites and white blood cells in Giemsa stained thick blood smears. The main differential factor is the usage of microscopic images exclusively acquired with low cost and accessible tools such as smartphones, being used a dataset of 194 images manually annotated by an experienced parasilogist. Using a SVM classifier and a total of 314 image features extracted for each candidate, the automatic detection of trophozoites detection achieved a sensitivity of 80.5% and a specificity of 93.8%, while the white blood cells achieved 98.2% of sensitivity and 72.1% specificity.

Keywords: image analysis; malaria; computer-aided diagnosis; microscopy; mobile devices.

4.1   Introduction

Malaria is a leading cause of death and disease in many developing countries [73]. In 2015, there were an estimated 214 million cases of malaria, which caused approximately 438 000 deaths. Around 90% of malaria cases occurred in Africa, where the lack of access to malaria diagnosis is largely due to a shortage of expertise, being the shortage of equipment the secondary factor. In a recent report [73], the WHO considers that the current funding distribution on malaria control commodities (US$ 1.6 billion in 2014) is not addressing the fundamental weaknesses in health systems of developing countries, suggesting that innovative ways may be required to rapidly expand access to malaria interventions. It worth underlining that the mobile phone is currently Africa's most important digital technology [6], and just as African telecommunications largely skipped over landline infrastructure and went straight to mobile phones, some experts say African medicine can skip over centralized labs [16]. Moreover, the combination of mobile devices with image processing for malaria diagnosis can bring several advantages, like potentially reduce the dependence of manual microscopic examination, which is an exhaustive and time consuming activity, simultaneously requiring a considerable expertise of the laboratory technician. Microscopy examination remains the gold standard for laboratory confirmation of malaria [9], which can be made through microscopic examination of thin and thick blood smears. While the thin smear consists in a single layer of red blood cells, the thick smear is 6-20 times thicker, allowing for a greater volume of blood to be examined. Thus, thick smears are firstly used to check the presence of malaria parasites (MPs), while thin smears are subsequently analyzed for the identification of MPs species.

This chapter presents an image processing and analysis methodology using supervised classification to assess the presence of *P.falciparum* trophozoites and White Blood Cells (WBCs) in Giemsa stained thick blood smears, using microscopic images acquired exclusively with smartphones.

4.2   Related Work

Image processing approaches have been proposed in order to identify parasites in malaria-infected thick blood smears [29, 17, 78, 46, 47]. *Kaewkamnerd et al., 2011*, used an adaptive threshold computed from the V-Value histogram using only 20 images, thus requiring further validation. *Elter et al., 2011*, have used a SVM classifier with a RBF kernel to identify objects containing chromatin, with reported sensitivity of 97%. Also, co-occurrence matrix and wavelet transform have been used by *Yunda et al., 2012*, for detection of *P.vivax* in thick blood films, combined with the usage of Neural Networks. In a different approach, *Purnama et al., 2013*, used Genetic Programming to detect different species and stages, with reported accuracy of 96% using 180 manually cropped sub-images. More recently, *Quinn et al., 2014*, have extracted moment and connected component features for classification with Extremely Randomized Trees with stated results of AUC=0.97 for the ROC curve, being the only work found that uses smartphone-acquired images. Indeed, promising results for malaria diagnosis. Nevertheless, most of these methodologies are based on two criteria: i) images acquired under well controlled conditions; ii) the need of proper microscopic equipment. Both criteria are difficult to accomplish in endemic areas of Malaria, where this type of equipment is scarce or nonexistent in healthcare facilities. In alternative, here, we present a different methodology approach for image processing on malaria-infected thick blood smears by using images exclusively acquired with low cost and accessible tools such as smartphone (see Fig. 1). The list of image features used in this work merges the outcomes of an extensive review of all the significant features proposed on the literature for MPs and WBCs detection [49], with new proposed features.
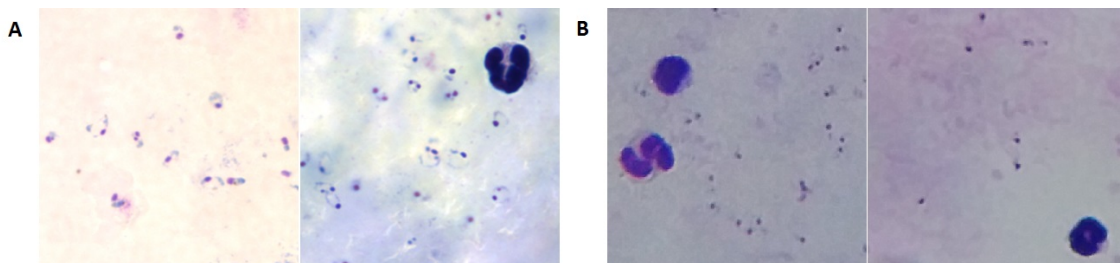
Figure 4.1: Cropped microscopic sub-images of *P.falciparum* trophozoites and WBCs on thick blood smear acquired with: (**A**) proper microscopic equipment [9]; (**B**) smartphone coupled to a Optical Magnification Prototype (see Section 3).

4.3 Mobile-based Framework for Malaria Parasites Detection: An Overview

The work reported in this chapter represents only a component of a mobile-based framework for MPs detection currently being developed, which is composed by 3 main components (see Fig. 4.2):

1) Optical Magnification Prototype: a cheap alternative to the current microscopes, that can easily be adapted to a smartphone and used in the field. This gadget guarantees the required 1000x magnification, and the smartphone camera is used to capture images. Moreover, it uses a self-powered motorized automated stage system, in order to move the blood smear and allow the automatic capture of several snapshots of the sample;

2) Image Processing and Analysis: consist on the automated detection of MPs in blood smears through computer-aided methods. Four species of *Plasmodium* can infect and be transmitted by humans, passing through 3 different growth stages. Thus, there are 12 different species-stage combinations, for each we aim to develop image processing modules to identify and count the respective MPs.

3) Smartphone Application: envisioned to be used by technical personnel without specialized knowledge in malaria diagnosis. The user collects and prepares a blood sample of the patient, introducing it in a slot of 1). Using the companion mobile application, installed in the smartphone that is coupled to 1), the user can take pictures of the blood smear using the smartphone's camera, being subsequently analyzed by 2), so the correct procedures and medication can be administered.
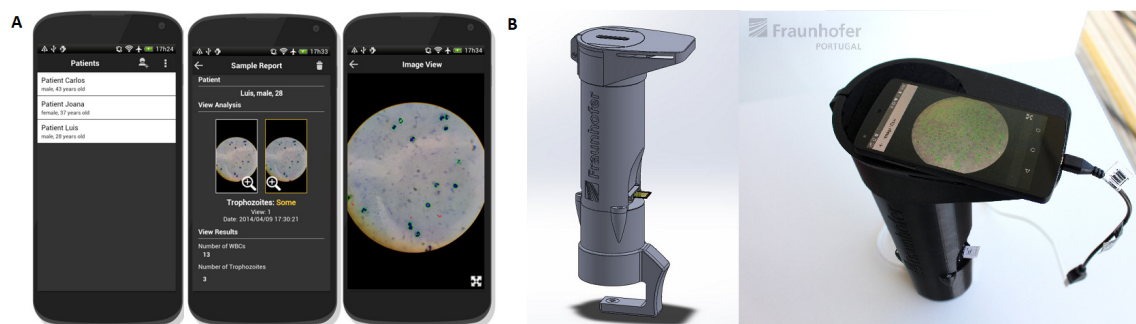
Figure 4.2: Mobile-based Framework for Malaria Parasites Detection: (**A**) Smartphone Application; (**B**) Optical Magnification Prototype.

4.4 Methodology

The proposed methodology can be divided into 3 main block: **Optical Circle Detection**; **WBCs Detection**; and **Trophozoites Detection**. For the Optical Circle Detection, the image was firstly converted to grayscale and a median filter with large window factor was applied to eliminate

the inner structures. The optical circle segmentation was performed using the Otsu's Method, a well-known histogram shape-based image thresholding routine. The remaining inner structures inside the optical circle were removed using a flood fill algorithm (see Fig. 4.4.B).

A dataset of microscopic images acquired from 6 different thick blood smears infected with *P.falciparum* was used for development and testing of the proposed approach. The images were acquired using the Optical Magnification Prototype (see Section 3), coupled to a smartphone. Two different smartphones were used, a HTC One S and a LG Nexus 5, with image resolutions ranging from 1456x2592 to 1944x2592 pixels. A total of 194 images were manually annotated by an experienced parasilogist from the Infectious Diseases Department of Instituto Nacional de Saúde Dr. Ricardo Jorge, with 352 identified trophozoites and 1935 white blood cells (see Fig. 4.3).
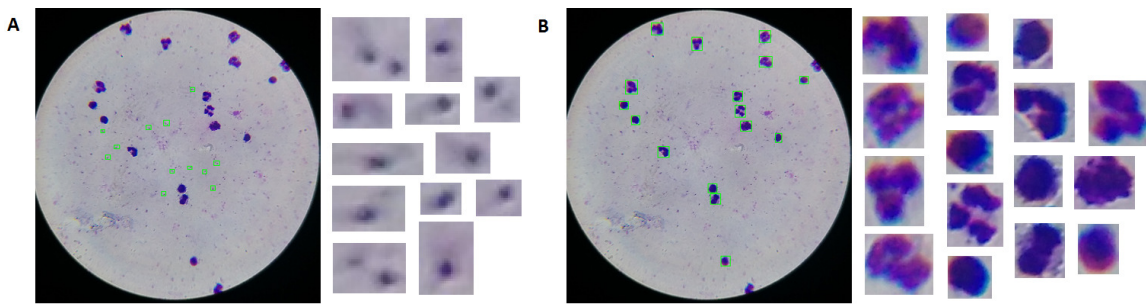
Figure 4.3: Microscopic Image Dataset: (**A**) Trophozoites manual annotation; (**B**) White Blood Cells manual annotation.

4.4.1   WBCs Detection

There are several types of WBCs, with different morphological characteristics, but every WBCs has a nucleous surrounded by cytoplasm. When a thick smear is prepared, the cytoplasm membrane is destroyed, thus being only visible the WBCs nucleus. The WBCs detection is divided into 2 main tasks:

1) WBCs Nuclei Candidates Segmentation: segment all the elements on the image that are possible candidates of WBCs nucleus, which stain blue to almost black with Giemsa stain. To detect the WBCs candidates, a pre-processing technique called mean shift filtering was firstly applied, using a spatial window radius of 5 and a color window radius of 15 [69]. This edge-preserving smoothing method showed to facilitate the segmentation, as it preserves the edges of the WBCs while the color inside the WBCs nuclei becomes more homogeneous. An adaptive thresholding is then applied to segment the WBCs candidates. Considering an original image I_L, the corresponding segmented I_S obtained by adaptive thresholding is given by Eq. 4.1. T_L is the mean intensity value of the square region centered on the pixel location (x,y) with a side value of R_S minus the constant C. In the proposed approach, it is used C=40 and R_S is given by Eq. 4.2, with a value for the division factor D_F=150. Furthermore, the Optical Diameter value represents the maximum diameter of the optical circle mask obtained previously. Since the microscopic images for malaria diagnosis will

have a fixed magnification of 1000x, using the Optical Diameter as a metric reference turns this adaptive segmentation approach independent of the image resolution. Finally, the optical circle mask is subtracted and the final WBCs candidates mask is obtained (see Fig. 4.4.C).

$$I_S(x,y) = \begin{cases} 0 & \text{if } I_L(x,y) > T_L(x,y) \\ 255 & \text{otherwise} \end{cases} \quad (4.1) \qquad R_S = \frac{\text{Optical Diameter}}{D_F} \quad (4.2)$$
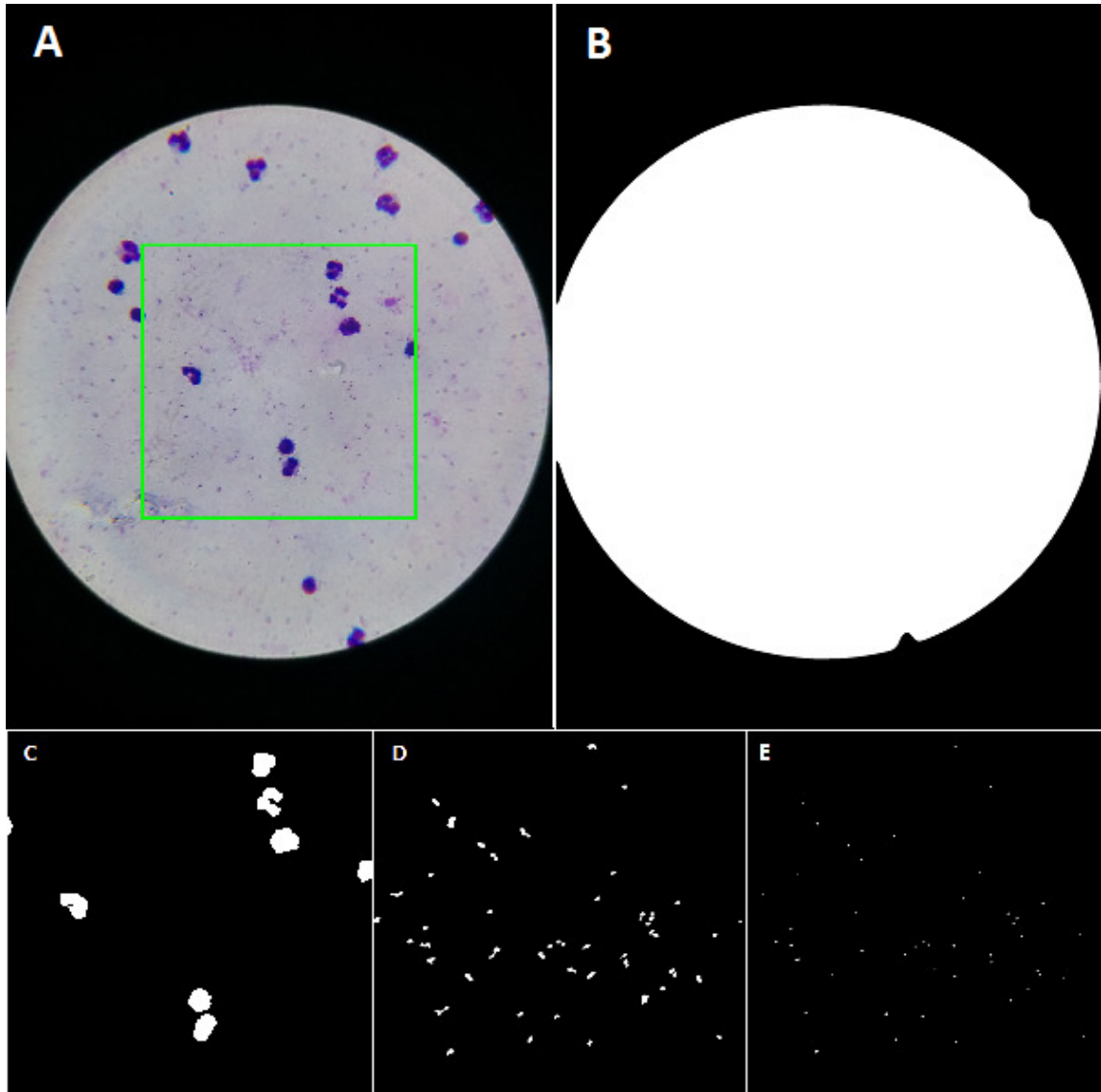
Figure 4.4: Segmentation Results: (**A**) Original image with region of interest (ROI) at green; (**B**) Optical Circle segmentation mask; (**C**) WBCs candidates segmentation mask of ROI; (**D**) Trophozoites candidates segmentation mask of ROI; (**E**) Chromatin dots candidates segmentation mask of ROI.

It should also be taken into account that WBCs nucleus can be composed by a single lobe or multiple detached lobes (see Fig. 4.3). To address the issue of detached lobes belonging to the same WBCs, the WBCs-candidates with size below the Optical Diameter are labelled as lobe-candidates.

Through the expansion of the bounding box of every candidate, if the bounding box of the lobe-candidate intersects with the bounding box of either another lobe-candidate or a WBCs-candidate, the bounding boxes are merged and the enclosing objects are labelled as a single WBCs candidate. Otherwise, the lobe-candidates are discarded from classification consideration. It worth noting that lobe-candidates may intersect with several neighbouring bounding-boxes, so the Jaccard index was used as the tie-breaking criterion;

2) WBCs Nuclei Candidates Feature Extraction and Classification: For each WBC candidate, a total of 152 image features were extracted, grouped into 3 major groups: Geometry; Color; and Texture features (see Table 4.1). Moreover, for machine-learning training purposes, each candidate was labelled according to the manual annotation, i.e. labelled as WBC if the overlap coefficient (also known as Szymkiewicz-Simpson coefficient) between the region of interest of the candidate and the manual annotation is higher than 0.75. A two-class SVM classifier [11] with a RBF kernel was used to create a classification model, using a grid-search approach to obtain the best γ and C parameters.

Table 4.1: Summary of the extracted image features.

Group	Family	Channels	Features
Geometry		Binary	Maximum Diameter [a], Minimum Diameter [a], Perimeter [a], Eccentricity, Convex Hull Area [a], Area [a], Elongation Bounding Box Area [a], Solidity, Extent, Circularity, Elliptical Symmetry, Principal Axis Ratio, Radial Variance, Asymmetry Indexes/ Ratios, Compactness Index, Irregularity Indexes, Bounding Box Ratio, Lengthening Index, Equivalent Diameter [a], Asymmetry Celebi.
Color		C* and h° (from L*C*h°)	Mean [b], Standard Deviation [b], L1 Norm [b], L2 Norm [b] Entropy [b], Energy [b], Skewness [b], Kurtosis. [b]
Texture	Discrete Fourier Transform	Grayscale	Mean, Standard Deviation, Maximum, Minimum.
	Gray Level Run Length Matrix	Grayscale	Short run emphasis [c], long run emphasis [c], run percentage [c], long run high grey level emphasis [c], low grey level runs emphasis [c], high grey level runs emphasis [c], short run low grey level emphasis [c], short run high grey level emphasis [c], grey level non-uniformity [c], long run low grey level emphasis [c].
	Gray Level Co-occurrence Matrix	R, G, B (from RGB)	Energy [c], Entropy [c], Contrast [c], Correlation [c], Maximum probability [c], Dissimilarity [c], Homogeneity [c].
	Laplacian	Grayscale	Mean, Standard deviation, Maximum, Minimum.

[a] Feature divided by D_{circle}, in order make it independent of image size; [b] feature computed independently for each channel, as well as for the grayscale masks that result by folding and subtracting the region of interest of each channel according the major and minor axis of inertia; [c] feature computed for the following directions: 0°, 45°, 90° and 135°.

4.4.2 Trophozoites Detection

Trophozoites are composed by a cytoplasm and one or two small chromatin dots. Using Giemsa stain, the cytoplasm usually stains blue and takes different shapes, from a well-defined, fine ring to forms that are irregular or bizarre, sometimes called 'amoeboid' [71] (see Fig. 4.1). The Trophozoites Detection is divided into 3 main tasks:

1) Trophozoites Cytoplasm Candidates Segmentation: The adaptive thresholding approach explained previously for the WBCs segmentation was adapted for the segmentation of trophozoites' cytoplasm. Since the expect dimensions and stain contrast of trophozoites' cytoplasm is significantly lower when compared to WBCs, the thresholding parameters were adapted through experimental testing ($C=6$, $D_F=40$). An area filtering process is then applied using Eq. 4.2, with $D_F=25$ and $D_F=4$ for minimum and maximum area, respectively;

2) Chromatin Dots Candidates Segmentation: The chromatin dot is a part of the parasite nucleus, usually round in shape and stains red with Giemsa stain. It usually appears in the acquired images as a sharp small dot, so the algorithm consists on creating a local differences mask. The original image is blurred using a median blur filter with a window size calculated using Eq. 4.2 with $D_F=80$. The small structures will disappear with the blurring process, among them the chromatin dots. The original image is then subtracted to the blurred image, and a 3-channel local differences mask is obtained. To binarize this mask, the maximum value in each pixel position along the 3-channels is selected, and the adaptive thresholding explained previously is applied with $C=10$ and $D_F=80$. To obtain the final chromatin dots mask, an area filtering process is then applied using Eq. 4.2, with $D_F=125$ and $D_F=25$ for minimum and maximum area, respectively. This mask is then used to filter the trophozoites' cytoplasm candidates mask, being only considered for further processing the cytoplasm candidates with at least one chromatin dot inside (see Fig. 4.4.D and 4.4.E);

3) Trophozoites Candidates Feature Extraction and Classification: Each trophozoite candidate will be composed by a trophozoites' cytoplasm candidate and at least one chromatin dot candidate. A total of 314 features are extracted for each trophozoite candidate: the 152 image features referred on Section 4.4.1, extracted independently for the correspondent trophozoite' cytoplasm and for the chromatin dots candidates; 10 ratios between specific cytoplasm and chromatin features (area, maximum and minimum diameter, perimeter, convex hull area, bounding box area, relative difference of C* and h channels mean values, difference of the coefficient of variation of C* and h channels). Moreover, the same approach referred on Section 4.4.1 was applied for candidates labeling and machine learning classification.

4.5 Results

The classification results are presented in terms of three metrics: 1) Sensitivity, i.e. the percentage of candidates correctly classified as WBC/MP; 2) Specificity, i.e. the percentage of candidates

correctly classified as Non-WBC/Non-MP; and 3) Accuracy, i.e. the percentage of candidates correctly classified overall. In Table 4.2 the results for WBCs and *P.falciparum* trophozoites candidates after segmentation and filtering are depicted, while in Table 4.3 are detailed the results after machine-learning classification using candidate region-wise 10-fold cross-validation.

Table 4.2: Results for WBCs and *P.falciparum* trophozoites candidates after segmentation and filtering.

	Manual Annotations	True Positives	False Positives	False Negatives
WBCs	1935	1850	265	85
Trophozoites	352	277	1566	75

Table 4.3: Results for WBCs and *P.falciparum* trophozoites detection after machine-learning classification.

	SVM Params	True Positives	True Negatives	False Positives	False Negatives	Sensitivity	Specificity	Accuracy
WBCs	γ=0.2 C=1.0	1817	191	74	33	98.2%	72.1%	94.9%
Trophozoites	γ=0.03 C=0.025	223	1469	97	54	80.5%	93.8%	91.8%

The suggested methodology was implemented in C++ using the OpenCV library. In terms of performance, the registered average computational time was 4,59 seconds running on an Intel® Core™ i7-4790 CPU with 3.60GHz (with OS Ubuntu 14.04 LTS). The implemented C++ code was also deployed on a Samsung Galaxy 5 (CPU Quad-core 2.5 GHz Krait 400 running on Android OS 5.0), with an average time of 44 seconds. Moreover, the memory allocation of the proposed methodology was also analyzed using the Valgrind profiling tool, with maximum memory peaks detected always below 100MB for the images used in this study.

4.6   Conclusions and Future Work

In this work, a methodology to assess the presence of *P.falciparum* trophozoites and WBCs in Giemsa stained thick blood smears is presented. The great majority of the proposed methodologies to date are based on images acquired under well controlled conditions and with proper microscopic equipment, so the main differential factor of this work is the usage of microscopic images exclusively acquired with smartphones coupled to a low cost optical magnification device, as well as the consequent customization of the proposed methodology for images with such characteristics. Given the lack of freely available image datasets, a mobile acquired image dataset manually annotated by a specialist was specifically created and used in this study. Moreover, a wide variety of image features were used to characterize the candidates in terms of geometry, texture and color, merging significant features referred on previous works, with some never used before for this purpose. In terms of

results, the automatic detection of WBCs in thick blood smears achieved 98.2% of sensitivity and 72.1% specificity, while the *P.falciparum* trophozoites detection achieved a sensitivity of 80.5% and a specificity of 93.8%.

It should be noted that this work represents only a component of a mobile-based framework for malaria parasites detection currently being developed. As future work in terms of image processing, we aim to develop methodologies for the analysis of thin blood smears images acquired exclusively with smartphones, in order to identify and count all possible species-stages combinations of MPs that can potentially infect humans. The main final goal is to develop a system that can provide an effective pre-diagnosis of malaria to be used in medically underserved areas.

Chapter 5

Mobile-Based Analysis of Malaria-Infected Thin Blood Smears: Automated Species and Life Cycle Stage Determination

Luís Rosado, José M. Correia da Costa, Dirk Elias and Jaime S. Cardoso

Abstract

Microscopy examination has been the pillar of malaria diagnosis, being the recommended procedure when its quality can be maintained. However, the need for trained personnel and adequate equipment limits its availability and accessibility in malaria-endemic areas. Rapid, accurate, accessible diagnostic tools are increasingly required, as malaria control programs extend parasite-based diagnosis and the prevalence decreases. This chapter presents an image processing and analysis methodology using supervised classification to assess the presence of malaria parasites and determine the species and life cycle stage in Giemsa-stained thin blood smears. The main differentiation factor is the usage of microscopic images exclusively acquired with low cost and accessible tools such as smartphones, a dataset of 566 images manually annotated by an experienced parasilogist being used. Eight different species-stage combinations were considered in this work, with an automatic detection performance ranging from 73.9% to 96.2% in terms of sensitivity and from 92.6% to 99.3% in terms of specificity. These promising results attest to the potential of using this approach as a valid alternative to conventional microscopy examination, with comparable detection performances and acceptable computational times.

5.1 Introduction

Between 2010 and 2015, malaria mortality rates fell by an estimated 29% globally and by 31% in the African region due to the scale-up of malaria interventions. Despite this remarkable progress, the global tally of malaria in 2015 was still 212 million new cases and 429,000 deaths, it being estimated that malaria surveillance systems detected only 19% of the cases that occurred globally. Most of these deaths occurred in the African region (92%), but it is estimated that nearly half of the world's population is at risk of malaria, being considered endemic in 91 countries [74]. Across Africa, millions of people still lack access to the tools they need to prevent and treat the disease. Prompt diagnosis can not only prevent the development of severe malaria, but also reduce the length of time that patients carry malaria parasites (MPs) in their blood, which in turn reduces the risk of onward transmission [74].

A recent report [73] considers that current funding distribution on malaria control commodities (US $1.6 billion in 2014) is not addressing the fundamental weaknesses in health systems of developing countries, suggesting that innovative ways may be required to rapidly expand access to malaria interventions. It is worth underlining that the mobile phone is currently Africa's most important digital technology [6], and just as African telecommunications largely skipped over landline infrastructure and went straight to mobile phones, some experts say African medicine can skip over centralized labs [16]. Moreover, the combination of mobile devices with image processing for malaria diagnosis can bring several advantages, like potentially reducing the dependence of

manual microscopic examination, which is an exhaustive and time-consuming activity and requires considerable expertise of the laboratory technician.

This chapter presents an image processing methodology using supervised classification to analyze microscopic images of malaria-infected thin blood smears, by assessing the presence of MPs and determining the species and life cycle stage. One of the main contributions of this work is the usage of images acquired exclusively with smartphones. This differentiation factor is directly related with the integration of this methodology in a mobile-based framework currently being developed, which aims to support the pre-diagnosis of malaria in rural areas. Moreover, the proposed approach was designed taking deeply into account the clinical knowledge of each particular structure we aim to detect (e.g., morphology, staining behavior and expected inner structures).

5.2   Malaria Disease Characterization

This section gives an overview of essential concepts for understanding malaria, namely the characterization of MPs in terms of growth stages and species, as well as the recommended malaria diagnostic methods. In order to keep the text self-contained, we are going to revisit the characterization of the malaria disease as presented in [49].

MPs are blood parasites that are transmitted to humans through the bite of an infected mosquito, passing over three different growth stages: (i) Trophozoites: the most commonly-seen stage, which can vary from small to quite large within red blood cells (RBCs). Trophozoites have usually only one chromatin dot, but two are commonly seen in *P. falciparum* species. The cytoplasm morphology takes different shapes, ranging from demarcated fine rings to irregular and amoeboid forms; (ii) Schizonts: Trophozoites mature into schizonts through multiple divisions of the parasite into daughter cells called merozoites. Each merozoite is in fact a new parasite, with its own chromatin body and cytoplasm. The infected RBCs eventually bursts, allowing the new merozoites to travel within the bloodstream to infect new RBCs; (iii) Gametocytes: some trophozoites differentiate into sexual erythrocytic stages called gametocytes, usually about the size or bigger than RBCs. Gametocytes present variable morphologies, from round to banana-shaped, depending on the species. In terms of biological classification, MPs are protozoan parasites of the genus *Plasmodium*. Five species of *Plasmodium* can infect and be transmitted by humans: *P. falciparum*, *P. vivax*, *P. ovale*, *P. malariae* and *P. knowlesi*.

Since 2010, WHO has recommended that all persons with suspected malaria should undergo malaria diagnostic testing, by either microscopy or rapid diagnostic tests (RDTs). Microscopy examination consists of preparing a blood smear, staining it (most often with Giemsa stain) and examining it through a microscope. This process remains the mainstay of malaria diagnosis in most large health clinics and hospitals. However, microscopy-based diagnosis in rural areas is frequently non-existent or inadequate in terms of quality due to scarce resources (equipment and trained staff). When stained MPs are spotted by the microscopist, the diagnosis of malaria is confirmed by identifying the respective stage, species and infection density [71]. Microscopic

examination can be made through the usage of thin and thick blood smears. While the thin smear consists of a single layer of RBCs, the thick smear is six- to 20-times thicker, allowing for a greater volume of blood to be examined. Thus, thick smears are firstly used to check the presence of MPs, while thin smears are subsequently analyzed for the identification of MP species. The conventional flow for both quantification and species/life cycle stage identification is presented in Figure 5.1.
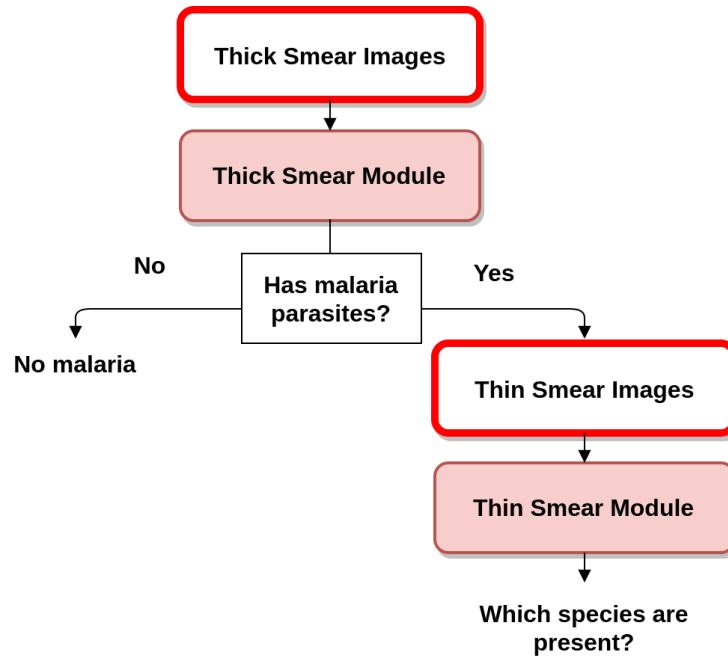
Figure 5.1: Blood smear analysis flow for both quantification and species/life cycle stage identification.

Malaria diagnosis through RDTs is accomplished by detecting specific malaria antigens in a person's blood. However, the use of the RDT does not eliminate the need for malaria microscopy for two main factors: (i) the RDT may not be able to detect some infections with low parasite density; (ii) the currently approved RDT in the U.S. only detects two different malaria antigens (one is specific for *P. falciparum*, and the other is found in all four human species of malaria). Thus, microscopy is further needed to determine the parasite species and to quantify the proportion of RBCs that are infected, which is an important prognostic indicator [10].

5.3   Related Work

Several image processing approaches have been recently proposed for the identification of MPs in thin blood smears. One of the first approaches was proposed by Zou et al., 2010 [80], through the usage of an improved circle Hough transform to detect RBCs. By analyzing the RGB (red, green, blue) color space, the authors observed that nucleated components present distinctively high intensity values in the B channel and simultaneously low intensities in the G channel. Therefore, an approach to stretch the contrast of nucleated objects was proposed based on the observed differences between these two color channels.

In order to obtain a more detailed analysis of infected RBCs, Anggraini et al., 2011 [4], proposed a methodology focused on detecting three regions inside these structures: MP nucleus, MP cytoplasm and RBC cytoplasm. For each region, image features based on area ratios and range of intensities were extracted. The detection of infected RBCs using a Bayes decision rule classifier achieved a sensitivity (SE) of 92.59% and a specificity (SP) of 99.65%, but only 60 and 20 images were used for training and testing, respectively.

A different approach for RBCs segmentation was proposed by Malihi et al., 2013 [38], which merges Otsu's segmentation with edge detection via Canny's method. After passing a hole-filling process, image features were extracted for each segmented structure, more specifically in terms of gradient, texture, histogram and area granulometry. Five different classifiers were tested, the best results being achieved by a kNN (k-nearest neighbors) with 80% of SE and 95.5% of SP.

Later on, a k-means clustering for MPs segmentation was proposed by Khan et al., 2014 [32]. This method has the particularity of being based on the usage of the b*-color channel of the CIE (Commission International de l'Élairage) L*a*b* (lightness, green/red coordinate, blue/yellow coordinate) color space. A total of 118 Leishman-stained microscopic images were used, results being reported of 76% and 60% for SE and SP, respectively. However, the proposed approach simply consists of classifying the images as infected/not infected, thus not giving information about the number of correctly-identified MPs in each image, nor the respective species and growth stage.

In another work by Nugroho et al., 2015 [44], segmentation of MPs was made through a k-means algorithm. Using histogram-based texture features, the authors aimed to detect the parasites in three different life cycle stages using a multilayer perceptron with backpropagation algorithm, with reported SE of 81.7% and SP of 90.8%. However, only *P. falciparum* was considered, with results obtained using a limited dataset of 60 manually-cropped sub-images.

Nanoti et al., 2016 [43], used k-means clustering applied on RGB, HSI and L*a*b color spaces for MPs' segmentation, followed by various textural and shape features. A total of 300 images with 386 annotated MPs were used for the classification in 13 classes (12 classes for three life cycle stage for each of the four malaria species and one class for non-infected blood samples). However, the classes distributions were not detailed, i.e., the number of parasites for each species-stage combination. Two classifiers were used, kNN and SVM (support vector machines), with the best performance for kNN with accuracy (AC) of 90.2% and SE of 90.2%. Unfortunately, only the overall performance is given, not being detailed for each species-stage combination.

More recently, Yang et al., 2017 [76], developed a low-cost image-based cytometer for scoring and classifying MPs' stages, with the innovative aspect of comparing the obtained parasitemia results with flow cytometry. The authors used an adaptive thresholding approach for segmentation and an SVM with a linear kernel for classification, with reported high specificity, sensitivity and negligible false positives (~0.0025%). However, several limitations can be identified for the proposed approach: Only 25 positive images were used to train the classifier; the classification is based on a simple three-dimensional feature space, namely the average pixel intensity; several parameters are defined in terms of the number of pixels, thus requiring manual user calibration for images with different pixel resolutions; Stage differentiation is exclusively based on the area

occupied within the RBCs, the detection of gametocytes not being considered; and finally, this study only considered *P. falciparum*.

Despite these promising results during the past few years, most of the proposed methodologies are based on two main requirements unsuitable for most malaria-endemic areas: (i) images acquired under well-controlled conditions; and (ii) the need for proper microscopic equipment. Both criteria are difficult to accomplish in those areas where this type of equipment and the know-how to maneuver it are scarce or nonexistent. As an alternative, here we present a different methodology for automated analysis of malaria-infected thin blood smears by using images exclusively acquired with low-cost and accessible tools such as smartphones. Despite not being the main focus of this chapter, it should be noted that this work represents only a component of a mobile-based framework for MPs' detection currently being developed, which will be briefly described in Section 5.4.

In terms of the selected approaches for image processing and machine learning, we go beyond the state-of-the-art and achieve a more robust and consolidated methodology that tackles the issue of identifying different MPs' species-stage combinations on the same image. For that purpose, some of the successful outcomes previously reported were tested, adapted and integrated in our methodology, along with new proposed processing steps, which will be detailed in Section 5.5. Finally, the proposed approaches are greatly inspired by the in-depth clinical knowledge of each particular species-stage combination we aim to the detect (e.g., morphology, staining behavior and expected inner structures).

5.4 Mobile-Based Framework for Malaria Parasites Detection: An Overview

The work reported in this chapter represents only a component of a mobile-based framework for MPs' detection currently being developed, which is composed by three main components (see Figure 5.2):

I μ**SmartScope**: an inexpensive alternative to the current microscopes that can easily be adapted to a smartphone and used in the field. This gadget guarantees the required $1000\times$ magnification, and the smartphone camera is used to capture images. Moreover, it uses a self-powered motorized automated stage system, in order to move the blood smear and allow the automatic capture of several snapshots of the sample [52];

II **Image processing and analysis**: consisting of the automated detection of MPs via computer vision and machine learning approaches, on microscopic blood smear images acquired using I. This component consists of two main modules, as detailed in Section 5.2:

  (a) *Thick smear module* to detect the presence of MPs on thick blood smears [50].

  (b) *Thin smear module* for the determination of MPs species and life cycle stage (main focus of this chapter).

III **Smartphone application**: envisioned to be used by technical personnel without specialized knowledge in malaria diagnosis. The user collects and prepares a blood sample of the patient, introducing it in a slot of I. Using the companion mobile application, installed in the smartphone that is coupled to I, the user can take pictures of the blood smear using the smartphone's camera, being subsequently analyzed by II, so the correct procedures and medication can be administered.

Figure 5.2: Mobile-based framework for malaria parasites's detection: (**A**) μSmartScope with smartphone attached and blood smear inserted; (**B**) smartphone application screenshots; (**C**) exemplificative usage of the solution (from left to right): (i) blood smear insertion; (ii) start image acquisition through the smartphone app; and (iii) visual feedback of the automated detection.

5.5 Methodology

The proposed methodology for the automatic determination of MPs species and life cycle stage on mobile-acquired thin smear images can be divided into 4 main blocks (see Figure 5.3): (i) pre-processing and RBC module; (ii) trophozoites module; (iii) schizonts module; and (iv) gametocytes module.

5.5.1 mThinMPs Database

The Mobile Thin Smear Malaria Parasites (mThinMPs) Image Database is an unpublished dataset acquired from 7 different thin blood smears infected with different MPs (see Figure 5.4). The blood smears were supplied by the Instituto Nacional de Saúde Dr. Ricardo Jorge, Portugal, and

Figure 5.3: Diagram of the proposed methodology for the automatic analysis of thin smear images.

the images acquired using the μSmartScope prototype coupled to a smartphone (see Section 5.4). Two different smartphones were used, an HTC One S and an LG Nexus 5, with image resolutions ranging from 1944×2592 to 1840×3264 pixels. This image database contains a total of 566 microscopic images. The images were manually annotated (bounding boxes) by an experienced parasitologist from the Infectious Diseases Department of Instituto Nacional de Saúde Dr. Ricardo Jorge, with a total of 1127 identified MPs. A detailed description of the manual annotations by species and life cycle stage is depicted in Table 5.1.

Table 5.1: MPs' manual annotations by species and life cycle stage in the mThinMPs database.

	Trophozoites	Schizonts	Gametocytes
P. falciparum	585	n.a.	58
P. ovale	122	80	62
P. malariae	164	27	29

It is worth noting that no representatives of *P. falciparum* schizonts are present in the dataset since they are rarely seen in peripheral blood. Moreover, this database does not include examples of *P. vivax*, since all specimens were obtained via African clinical partners, and *P. vivax* has practically no clinical incidence in Sub-Saharan Africa.
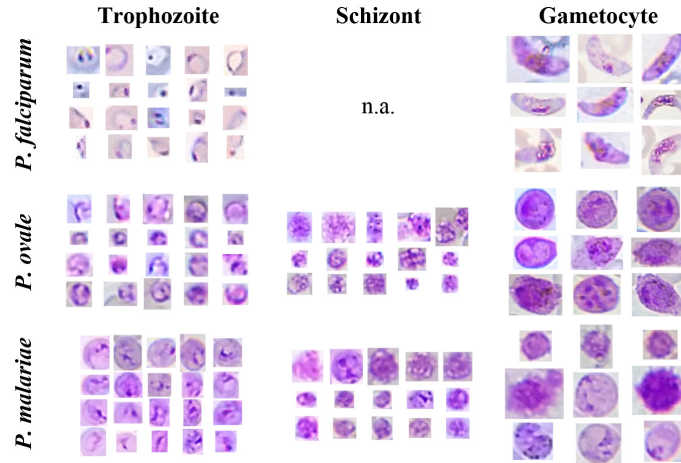
Figure 5.4: Illustrative examples of different MPs species and life cycle stages from the Mobile Thin Smear Malaria Parasites (mThinMPs) database.

5.5.2 Pre-Processing

The pre-processing procedure includes two main steps: (i) brightness and contrast adjustment and (ii) sharpening.

5.5.2.1 Brightness and Contrast Adjustment

The images acquired with the μSmartScope will have a circular region of interest (ROI) at the center of the image, a region from now on termed the optical circle (see Figure 5.5). Outside this region, the image is expected to be black, while inside the optical circle, the background is expected to be near white.
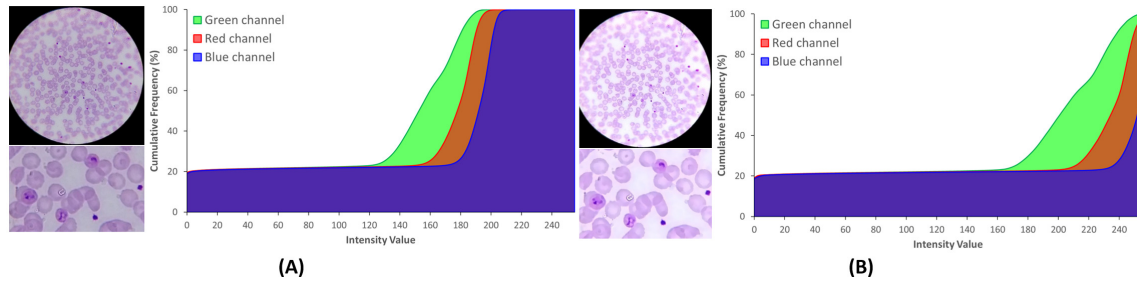
Figure 5.5: Effect of brightness and contrast adjustment, with cumulative histograms: (**A**) original image; (**B**) processed image after α and β correction, followed by mean-shift filtering.

The brightness and contrast were adjusted through a commonly-used procedure that applies a constant gain α and bias β to the original image. From the histogram perspective, α and β will operate as the color range amplifier and range shift, respectively. These parameters are computed automatically by assuming that the desired histogram range is 255, and only intensities with more than 1% frequency are considered to define the minimum and maximum intensity values used to stretch the histogram (see Figure 5.5). As a consequence of this process, in Figure 5.5B a higher range of intensities where the G channel is clearly separated is observable. This channel was

considered in previous works [80, 19] the most distinctive RGB channel for stained components, a fact that our research also confirms (see Figure 5.6C). Therefore, an increased demarcation of the G channel as a result of the contrast adjustment is a clearly positive aspect, since it will later facilitate the segmentation process of the stained components.

On the other hand, the cumulative histogram also shows that the B channel becomes much more polarized around two major clusters near 0 and 255. Previous works also confirm [80, 19] that stained components on the B channel present a significantly lower intensity demarcation, making this channel highly interesting for the optical circle segmentation. Looking at B channel image in Figure 5.6E, it becomes clear that these two major clusters represent in fact the regions inside and outside that region. To finalize, a smoothing procedure using a mean shift filtering was applied [69]. We chose this particular filter due to its edge-preserving characteristics, which was shown to greatly facilitate the following segmentation process by simultaneously preserving the edges of stained components and homogenizing the stain color intensities.
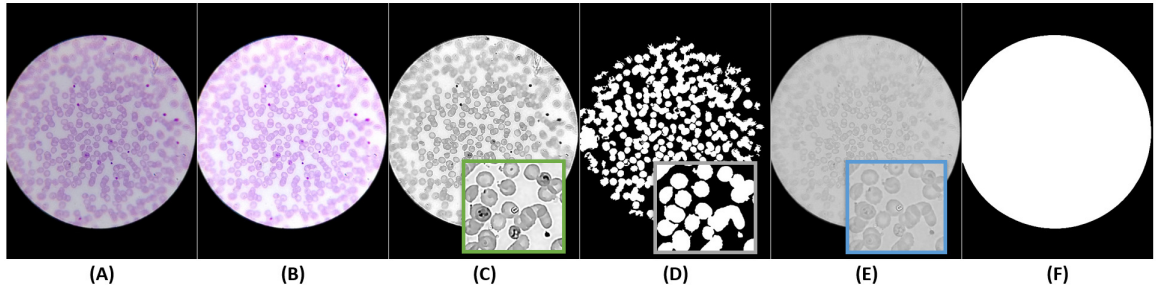
Figure 5.6: Pre-processing: (**A**) original image; (**B**) brightness and contrast adjustment; (**C**) sharpening applied over green channel of adjusted image; (**D**) RBCs segmentation applied over the sharpened image; (**E**) blue channel of the original image; (**F**) optical circle segmentation applied over the blue channel of the original image.

5.5.2.2   Sharpening

The goal of this pre-processing step is to increase the sharpness of the stained components by using an unsharp masking procedure. Particularly, the unsharped mask was obtained by blurring the target image using a Gaussian filter with a fixed window radius of 15 and combining it with the original image according to the weights of Equation (5.1):

$$I_{Shar} = 1.5 \times I_{Green} - 0.5 \times I_{Gau} - (0.75 \times I_{Green} \odot 0.2 \times I_{Lap}), \tag{5.1}$$

where the image I_{Green} is the green channel of the brightness and contrast adjustment output and I_{Shar} the sharpened image. It is worth noting that a Laplacian component was also added to the sharpening procedure. The unsharp mask can cause artifacts on edge borders, so the Laplacian component is responsible for avoiding double edges. This component was obtained through an

element-wise multiplication ($\odot$) of the original image with the Laplacian of the original image using the following kernel: $\begin{bmatrix} 0 & 1 & 0 \\ 1 & -4 & 1 \\ 0 & 1 & 0 \end{bmatrix}$.

5.5.3 Segmentation and Filtering

The segmentation and filtering component of the proposed methodology can be divided into 5 main blocks: (i) optical circle segmentation; (ii) RBCs' segmentation; (iii) trophozoites' segmentation; (iv) schizonts' segmentation; and (v) gametocytes' segmentation.

The most relevant difference between the currently most popular segmentation approaches and the adaptive thresholding approach proposed in this work is the usage of the in-depth clinical knowledge of each particular structure. Particularly, we took advantage of its known morphology, staining behavior and expected inner structures to customize the respective segmentation procedures. With that purpose, we started by mapping the expected maximum length of those structures in μm (see Table 5.2), in order to adapt the respective segmentation methods accordingly.

Table 5.2: Maximum length and respective D_{circle} relative ratios of RBCs' and MPs' structures [13].

	Length (μm)	**Approximate D_{circle} Ratio**
D_{circle}	215	-
RBCs	7~8	3^{-2}~4^{-2}
Trophozoites	1~7	4^{-3}~4^{-2}
Schizonts	5~10	2^{-2}~5^{-2}
Gametocytes	7~14	3^{-2}~7^{-2}

The optical diameter D_{circle} depicted in Table 5.2 represents the maximum diameter of the optical circle mask, for which the real size was calculated in a previous work [52]. The microscopic images have a fixed magnification of 1000×, so D_{circle} is used as a metric reference that makes this adaptive segmentation approach independent of the image resolution. Particularly, D_{circle} ratios were later used as the initial reference for tuning the window sizes of the different segmentation and area filtering algorithms.

5.5.3.1 Optical Circle Segmentation

According to the contrast analysis of Section 5.5.2.1, only the B channel of the original image was used for the optical circle segmentation (see Figure 5.6E,F). Since this is a fairly trivial segmentation task, we opted for a simple approach that allows a fast computational performance. A median filter with a large window factor was firstly applied to eliminate the inner structures, and the segmentation was performed using Otsu's method, a well-known histogram shape-based image thresholding routine. The remaining inner structures inside the optical circle were then removed using a flood fill algorithm.

5.5.3.2 RBCs Segmentation

As previously explained, the proposed segmentation methods for the different structures were independently customized according to the known clinical knowledge. However, all of the segmentation methods have the particularity of being based on the same adaptive thresholding approach. Considering the pre-processed image I_{Shar}, the corresponding segmented image I_{Seg} is obtained according to Equation (5.2):

$$I_{Seg}(x,y) = \begin{cases} 0 & \text{if } I_{Shar}(x,y) > T_{Shar}(x,y) \\ 255 & \text{otherwise} \end{cases}, \tag{5.2}$$

where T_{Sharp} is the mean intensity value of the square region centered on the pixel location (x, y) with a side value of W_{Side} minus the constant C. For the RBCs' segmentation, we used $C = 3$, and W_{Side} is given by Equation (5.3), with a scale factor $S_{Factor} = 1.5^{-1}$.

$$W_{Side} = D_{circle} \times S_{Factor} \tag{5.3}$$

The optical circle mask is then subtracted to eliminate segmented regions outside of the optical circle, and a closing morphological operation with an elliptical structuring element of size 3 is then applied. Finally, the RBC candidates pass through an area filtering process with $A_{RBC}^{Min} = D_{circle} \times 2^{-1}$ and $A_{RBC}^{Max} = D_{circle} \times 100$ used as the minimum and maximum area thresholds, respectively. As a side note, the defined value for A_{RBC}^{Max} is much higher than initially expected. This is related with the significant overlap of RBCs commonly verified, which results in agglomerated structures that should not be discarded, since the RBCs' mask will be further used to filter certain MPs candidates that develop exclusively inside RBCs.

5.5.3.3 Trophozoites' Segmentation

When merozoites infect an RBC, they develop to form ring-stage trophozoites, which then progress to mature trophozoites. While the chromatin dots usually are relatively similar along trophozoites' growth, there are significant differences in terms of cytoplasm morphology, as depicted on Figures 5.7 and 5.8. Thus, we propose a single approach to segment trophozoites chromatin dots, but the cytoplasm segmentation follows different paths for ring and mature stages.

Chromatin dots segmentation: The chromatin dot is a part of the parasite nucleus, usually round in shape, and stains red with Giemsa. It resembles to a sharp small dot, so the algorithm consists of creating a local differences mask. The I_{Shar} is blurred using a median blur filter with a W_{Side} obtained via Equation (5.3) and consistent with Table 5.2 ($S_{Factor} = 7^{-3}$). The small structures will disappear with the blurring process, among them the chromatin dots. The original image is then subtracted to the blurred image, and a 3-channel local differences mask is obtained (see Figures 5.7E and 5.8E). To binarize this mask, the maximum value in each pixel position along the 3 channel is selected, and the adaptive thresholding explained previously is applied with the same S_{Factor} used in the blur process and $C = -14$. To obtain the final chromatin dot mask, an

area filtering process is then applied using $A_{Chrom}^{Min} = D_{circle} \times 9^{-3}$ and $A_{Chrom}^{Max} = D_{circle} \times 8^{-2}$ as the minimum and maximum area thresholds, respectively (see Figures 5.7F and 5.8F).

Ring-stage cytoplasm segmentation: A preliminary cytoplasm segmentation mask is firstly obtained by tuning the threshold parameters of the adaptive thresholding approach previously explained. Since the cytoplasm stain contrast and expected dimensions are, respectively, significantly lower and higher than chromatin, the thresholding parameters were adapted accordingly ($C = 25$, $S_{Factor} = 2^{-2}$). It should be noted that this preliminary segmentation mask successfully includes most ring- and mature-stage cytoplasms, but they are usually merged with parts of RBCs. In order to refine the preliminary segmentation mask and remove these undesired RBC regions, the first consideration to be taken into account is that trophozoites have a darker stain intensity than RBCs, which is the reason why they are visible inside the RBCs. The second consideration is that stain intensity highly depends of the smear preparation procedure, as visible in Figures 5.7–5.10. Therefore, in order to obtain an enhanced version of I_{Shar} (termed I_{Shar}^{Tropho}) that is as independent as possible from the smear stain intensity and simultaneously highlights trophozoites, we start by using the previously-obtained RBCs mask and compute the mean intensity value inside RBCs structures. The regions of I_{Shar} outside the preliminary segmentation mask are then set to the computed mean value, a process that brings the background pixels intensities closer to the RBCs intensities. This image is then used to obtain the I_{Shar}^{Tropho} by subtracting the B channel from the G channel, a process that highlights the trophozoites' cytoplasm according to the contrast analysis made in Section 5.5.2.1 (see Figure 5.7C). The final ring cytoplasm binary mask (see Figure 5.7D) is then obtained via adaptive thresholding of I_{Shar}^{Tropho} ($C = -30$; $S_{Factor} = 1^{-1}$), followed by an area filtering process ($A_{Ring}^{Min} = D_{circle} \times 2^{-2}$; $A_{Ring}^{Max} = D_{circle} \times 5^{-1}$).

| (A) | (B) | (C) | (D) | (E) | (F) | (G) |

Figure 5.7: Examples of trophozoites ring stage candidates: (**A**) original image (cropped ROI); (**B**) brightness and contrast enhancement; (**C**) cytoplasm grayscale sharpening; (**D**) cytoplasm segmentation and filtering; (**E**) chromatin grayscale sharpening; (**F**) chromatin segmentation and filtering; (**G**) final candidates (cytoplasm in red; chromatin in yellow; RBC with candidate inside in green).

Mature-stage cytoplasm segmentation: The cytoplasm segmentation for the mature stage is quite similar to the one described for the ring stage, only changing the used adaptive threshold parameters and area thresholds, as a consequence of the described morphological differences. Particularly, the preliminary cytoplasm mask for the mature stage is obtained with $C = 3$ and $S_{Factor} = 1^{-1}$, while the final mature cytoplasm binary mask with $C = -40$ and the same S_{Factor}. Finally, an area-filtering process is applied ($A^{Min}_{Mature} = D_{circle} \times 1^{-1}$; $A^{Max}_{Mature} = D_{circle}$), followed by a hole-filling procedure (see Figure 5.8C,D).

| (A) | (B) | (C) | (D) | (E) | (F) | (G) |

Figure 5.8: Examples of mature trophozoite stage candidates: (**A**) original image (cropped ROI); (**B**) brightness and contrast enhancement; (**C**) cytoplasm grayscale sharpening; (**D**) cytoplasm segmentation and filtering; (**E**) chromatin grayscale sharpening; (**F**) chromatin segmentation and filtering; (**G**) final candidates (cytoplasm in red; chromatin in yellow; RBC with candidate inside in green).

Masks merging and candidates filtering: After obtaining the chromatin and cytoplasm segmentation masks separately, a mask merging process is responsible for merging these masks consistently and according to the expected morphological characteristics. Considering that trophozoites always appear inside RBCs on thin smears, the previously-generated RBCs' segmentation mask was firstly used to filter both trophozoites' segmentation masks, being only considered for further processing the candidate structures inside segmented RBCs. Moreover, all trophozoites must have at least one chromatin dot inside, so the cytoplasm candidates with no chromatin candidates inside are discarded, for both ring- and mature-stage masks. On the other hand, chromatin candidates that are not inside either a ring or mature cytoplasm candidate are also discarded. Finally, the filtered cytoplasm masks for ring and mature stages were summed into a single cytoplasm mask.

5.5.3.4 Schizonts' Segmentation

Trophozoites develop into schizonts, which divide several times to produce new merozoites. The infected RBCs eventually burst, allowing the new merozoites to travel within the bloodstream to infect

new RBCs. Thus, the proposed approach divides the schizonts segmentation task into two main steps: merozoites chromatin and schizonts cytoplasm segmentation.

Merozoites' chromatin segmentation: While the merozoites' cytoplasm is quite hard to differentiate in the acquired images, the schizonts' chromatin is very distinctive and similar to trophozoites' chromatin in terms of morphology and stain intensity. Consequently, we reused the approach described in Section 5.5.3.3 for chromatin dots' segmentation, with two small adjustments: (i) decreasing the C adaptive threshold parameter ($C = -5$), since merozoites' chromatin stain intensity can be less demarcated when compared to trophozoites' chromatin; and (ii) increasing the maximum area threshold ($A_{Chrom}^{Max} = D_{circle} \times 1.3^{-1}$), since the maximum dimension of merozoites' chromatin can be bigger (see Figure 5.9E,F).

Schizonts' cytoplasm segmentation: The maturation from trophozoite to schizont is a gradual process, so it is natural that trophozoites and schizonts share similarities in terms of visual appearance. However, since merozoites grow and duplicate inside schizonts', a bigger cytoplasm is expected for schizonts when compared with mature trophozoites. Thus, the approach described on Section 5.5.3.3 for mature trophozoites' cytoplasm segmentation was reused for schizonts' cytoplasm segmentation (see Figure 5.9C,D), the maximum area threshold only being tuned ($A_{Schizont}^{Max} = D_{circle} \times 3$).

Mask merging and candidate filtering: In order to merge the information of these two different segmentation masks, we started by using the merozoites' chromatin mask to filter the schizonts' cytoplasm candidates, i.e., only the cytoplasm candidates with at least one merozoite chromatin dot inside are considered for further processing. On the other hand, merozoites' chromatin candidates that are not inside a cytoplasm candidate are also discarded (see Figure 5.9G).
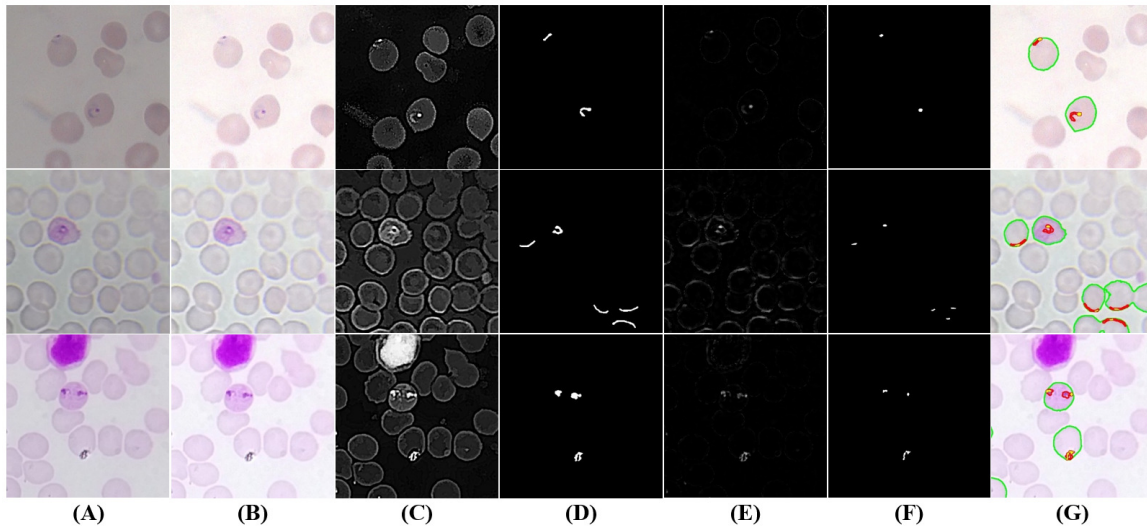

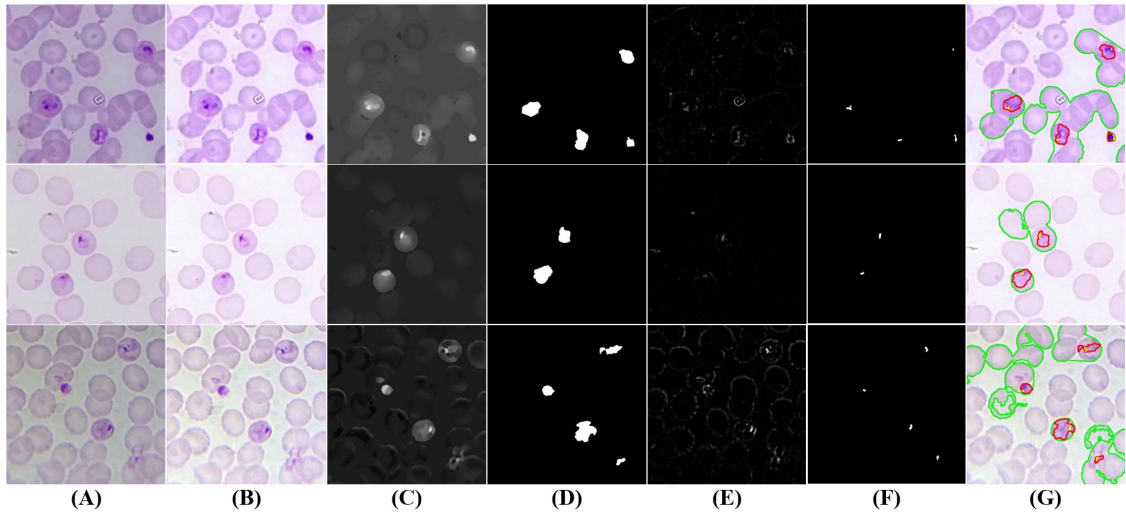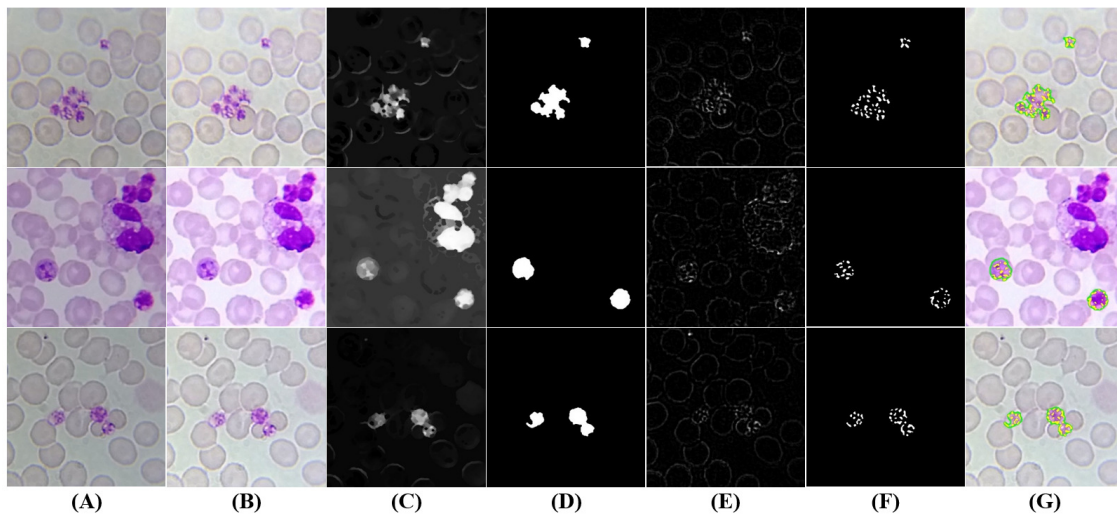Figure 5.9: Examples of schizonts candidates: (**A**) original image (cropped ROI); (**B**) brightness and contrast enhancement; (**C**) cytoplasm grayscale sharpening; (**D**) cytoplasm segmentation and filtering; (**E**) merozoites' chromatin grayscale sharpening; (**F**) Merozoites' chromatin segmentation and filtering; (**G**) final schizonts candidates (cytoplasm in green; chromatin in yellow).

5.5.3.5 Gametocytes Segmentation

Despite being originated via distinct cellular differentiation mechanisms, there are a few visual resemblances between mature schizonts and gametocytes in terms of dimensions and stain intensity. Nevertheless, two denoted differences between schizonts and gametocytes were used to adapt the approach described in Section 5.5.3.4 to segment gametocyte candidates (see Figure 5.10): (i) the average stain intensity of gametocytes is much more demarcated than schizonts, so the respective C adaptive threshold parameter in the final segmentation stage was tuned accordingly ($C = -20$); (ii) gametocytes are on average bigger than schizonts, so the minimum and maximum area thresholds were increased ($A_{Gametocyte}^{Min} = D_{circle} \times 4^{-1}$; $A_{Gametocyte}^{Max} = D_{circle} \times 4$). There is however an exception to this observation, namely the fact that *P. falciparum* banana-shaped gametocytes may be smaller than the respective schizonts, but this particular case is not relevant for our study since *P. falciparum* schizonts are rarely seen in blood samples.
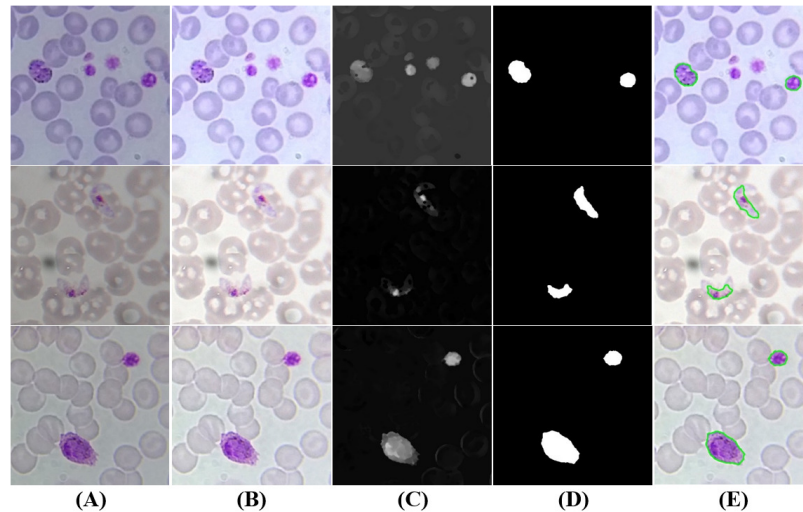
Figure 5.10: Gametocytes candidates: (**A**) original image (cropped ROI); (**B**) brightness and contrast enhancement; (**C**) grayscale sharpening; (**D**) segmentation and filtering; (**E**) final candidates (at green).

5.5.4 Feature Extraction

Instead of limiting any subsequent analysis to an initial choice of a limited set of features and since previous guidelines on high quality images may not hold for the images acquired with the proposed low-cost system, we decided to record a wide range of features. The considered list of image features was based on the outcomes of an extensive review of all of the significant features already proposed on the literature for malaria parasite detection on thin smears [49], merged with features so far not used for this purpose. We use a total of 152 image features, grouped into 3 major groups: geometry, color and texture features (see Table 5.3). The usage of the L*C*h° (lightness, chroma, hue) color space for the color group features is directly related to its particular characteristics of being device independent and designed to match human perception.

Table 5.3: Summary of the extracted image features.

Group	Family	Channels	Features
Geometry		Binary	Maximum Diameter [a], Minimum Diameter [a], Perimeter [a], Eccentricity, Convex Hull Area [a], Area [a], Elongation Bounding Box Area [a], Solidity, Extent, Circularity, Elliptical Symmetry, Principal Axis Ratio, Radial Variance, Asymmetry Indexes/ Ratios, Compactness Index, Irregularity Indexes, Bounding Box Ratio, Lengthening Index, Equivalent Diameter [a], Asymmetry Celebi.
Color		C* and h° (from L*C*h°)	Mean [b], Standard Deviation [b], L1 Norm [b], L2 Norm [b] Entropy [b], Energy [b], Skewness [b], Kurtosis. [b]
Texture	Discrete Fourier Transform	Grayscale	Mean, Standard Deviation, Maximum, Minimum.
	Gray Level Run Length Matrix	Grayscale	Short run emphasis [c], long run emphasis [c], run percentage [c], long run high grey level emphasis [c], low grey level runs emphasis [c], high grey level runs emphasis [c], short run low grey level emphasis [c], short run high grey level emphasis [c], grey level non-uniformity [c], long run low grey level emphasis [c].
	Gray Level Co-occurrence Matrix	R, G, B (from RGB)	Energy [c], Entropy [c], Contrast [c], Correlation [c], Maximum probability [c], Dissimilarity [c], Homogeneity [c].
	Laplacian	Grayscale	Mean, Standard deviation, Maximum, Minimum.

[a] Feature divided by D_{circle}, in order make it independent of image size; [b] feature computed independently for each channel, as well as for the grayscale masks that result by folding and subtracting the region of interest of each channel according the major and minor axis of inertia; [c] feature computed for the following directions: 0°, 45°, 90° and 135°.

It should be noted that another differentiation factor of our work is the usage of the clinical knowledge for each particular species-stage combination also in terms of the extracted image features. In Section 5.5.3, we described the extraction of more than one segmentation mask for some life cycle stages, for instance by separately segmenting the inner structures commonly present in that stage. In fact, the morphology and staining behavior of those inner structures can be highly relevant for the correct visual characterization of a specific species-stage combination, so we want to supply this detailed information to the classification model. The next sub-sections detail the image features extracted or each particular stage.

5.5.4.1 Trophozoites' Features

Each trophozoite candidate will be composed by a trophozoite cytoplasm candidate and one chromatin dot candidate. Despite the event of two chromatin dots associated with a specific cytoplasm candidate being uncommon, only one of those chromatin candidates will be considered for feature extraction. The selection of the representative chromatin candidate is made according to the following criterion: since chromatin dots have a demarcated circular shape, we select the chromatin candidate with the minimum elongation feature value (the ratio between the minimum and maximum distance from the center of mass to the boundary). A total of 314 features is then

extracted for each trophozoite candidate: the 152 image features referred to in Table 5.3, extracted independently for the correspondent trophozoites' cytoplasm and chromatin dot candidates; 10 ratios between specific cytoplasm and chromatin features (area, maximum and minimum diameter, perimeter, convex hull area, bounding box area, relative difference of the C* and h channels' mean values, the difference of the coefficient of variation of the C* and h channels).

5.5.4.2 Schizonts' Features

Each schizont candidate will be composed by a schizont cytoplasm candidate and at least one merozoite chromatin dot candidate. Unlike trophozoites, schizonts can present 10–36 chromatin dots in the erythrocytic stage, each one belonging to a different merozoite. Due to the high number of expected chromatin candidates, the selection of a single candidate (as described above for the trophozoites) appears to be unsuitable for the schizonts' scenario. Taking this into account, a total of 204 features is extracted for each trophozoite candidate: the 152 image features for the schizont cytoplasm; averages of the 48 color features detailed in Table 5.3 extracted for each merozoite chromatin candidates; 4 color ratios between cytoplasm and chromatin features (the difference of the C* and h channels' mean values, the difference of the coefficient of variation of the C* and h channels).

5.5.4.3 Gametocytes Features

Unlike the other life cycle stages, the gametocytes' segmentation procedure results in a single binary mask. Thus, the 152 images features referred to above are extracted for each gametocyte candidate.

5.5.5 Classification

For machine learning training purposes, each observation was labeled according to the manual annotation, i.e., labeled as MPs of that specific species-stage combination if the overlap coefficient (also known as the Szymkiewicz–Simpson coefficient) between the region of interest of the candidate and the manual annotation is higher than 0.75. For each species-stage combination, a two-class SVM classifier with an RBF kernel was used to create a classification model, with the hyperparameters γ and C tuned accordingly. The classification model workflow that is responsible for connecting the eight generated classification models is explained in Section 5.6. It should be noted that no feature selection method was applied, since the performance bounds on which the SVM maximal margin is based are independent of the feature space dimensionality. This means that a good generalization performance can be achieved with huge dimensional feature spaces, but requires a careful tuning of the hyperparameters.

5.5.5.1 Data Augmentation

Data augmentation is commonly used to prevent overfitting and improve performance in imbalanced class problems. For our dataset, we verified a significant imbalance between MP and non-MP classes for all species-stage combinations (see Table 5.4). Thus, 7 new observations were created for each candidate labeled as MP through sequential 90° rotations and respective mirroring of the RGB and binary mask images (see Figure 5.11). The feature extraction for each replica was made according to the procedure described in Section 5.5.4. It should be noted that the index of the original observation for each generated replica was saved, in order to ensure during the training process that the original candidate and all the respective replicas are included in the same train/test set after the random split of the hold outs.
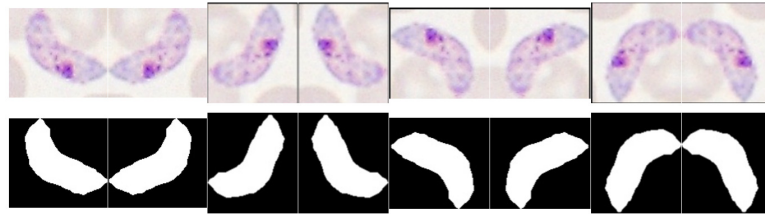
Figure 5.11: Illustrative examples of the data augmentation procedure.

5.5.5.2 SVM Hyperparameters Selection

Choosing optimal hyperparameter values is a crucial step during SVM design, usually involving the usage of specific performance metrics. The importance of the performance metric selection under this context can not be overstated, since it will greatly impact the behavior of the obtained classification model. It is worth noting that the usage of different performance metrics yields different trade-offs, so the requirements that are demanded for a specific classification scenario should always be taken into account during this process. For our particular scenario, we looked for metrics that primarily aim to improve the performance with respect to the target positive class (MP). However, due to our class-imbalanced data context, an acceptable performance to detect the non-target class (non-MP) was also required. Thus, we opted for the combination of two different metrics that weight sensitivity with specificity and precision, respectively: the informedness metric (also called Youden's index) and the F_1 score. In particular, a customized grid-search approach to obtain the best γ and C was implemented, according to the following steps:

1. All of the features were normalized between $[-1, 1]$.

2. Defining the search interval for each hyperparameter, namely $\gamma \in [2^{-15}, 2^3]$ and $C \in [2^{-5}, 2^{15}]$.

3. Defining the maximum number of rounds for the individual optimization of each hyperparameter (HP_{Round}), namely $HP_{Rounds}^{Total} = 5$. In each HP_{Round}, the target hyperparameter HP^{Target} is optimized, while the other parameter remains with a fixed value. The process starts with the γ optimization and fixed $C = 1$.

4. Defining the maximum number of rounds for the overall optimization of both hyperparameters ($Overall_{Round}$), namely $Overall_{Rounds}^{Total} = 3$. It should be noted that each $Overall_{Round}$ corresponds to the individual optimization of each HP^{Target}, as described in the previous step.

5. For each HP_{Round}, a hold out strategy is used by randomly splitting the dataset into training and test sets. A total of 20 hold outs was applied for each tested $[\gamma; C]$ combination, with 90% of the observations of both classes on the training set and the remaining used for testing purposes.

6. The best hyperparameters combination $[\gamma^{Best}; C^{Best}]$ is selected according to the performance metrics criteria described in Figure 5.12. This new proposed criteria aims to ensure that we select a classification model that has a balanced performance between the detection of both classes, even in data imbalance contexts. Particularly, this criteria allow the selection of a $[\gamma; C]$ that implies a decrease in one of the two considered metrics (when compared with the $[\gamma^{Best}; C^{Best}]$ found so far), but only if there is a performance improvement of the second metric that is twice greater than the performance loss suffered by the first.

7. At the end of each HP_{Round} and while HP_{Rounds}^{Total} is not achieved, the search interval is updated. Particularly, the search interval is updated to $HP \in [HP^{Best} \times 0.5, Hp^{Best} \times 1.5]$, being the main goal of this step the fine tuning of HP^{Target}.

8. A total number of 50 values of HP^{Target} for each search interval was tested. Due to the large value range and possible different orders of magnitude, the logarithmic scale was used to select equally-spaced values on the search interval. Considering the search interval $HP \in [HP^{Begin}, HP^{End}]$, the value on the i-th position is given by:

$$HP_i = 10^{log_{10}(HP_{Begin}) + log_{10}\left(\frac{HP_{End}}{HP_{Begin}}\right)^{i/\#HP_{values}}}, \tag{5.4}$$

where $\#HP_{values}$ is the maximum number of considered values for HP^{Target} under the considered search interval, with $i = \{0, 1, ..., \#HP_{values}\}$.

5.6 Results and Discussion

The results for the segmentation step are depicted in Table 5.4. Despite the significant imbalance between MP and non-MP classes for all stages, it should be noted that only 61 out of 1127 ground truth annotations do not have a segmented binary structure associated, thus not being considered for further SVM classification. In terms of the parameters required for the segmentation approach, the selection criteria were deeply influenced by the particularities of each stage in terms of morphology, staining behavior and expected inner structures. It worth noting that these parameters do not have a fixed value; they are automatically calculated for each new image through the extraction of the

---

Algorithm 1: Performance metrics criteria

Initializations:
INF is the *informedness* metric for the current $[\gamma, C]$ combination;
F_1 is the F_1score for the current $[\gamma, C]$ combination;
$[\gamma^{Best}; C^{Best}]$ is the best $[\gamma, C]$ combination found so far;
INF^{Best} is the *informedness* metric for $[\gamma^{Best}; C^{Best}]$;
F_1^{Best} is the F_1score for $[\gamma^{Best}; C^{Best}]$;

if $INF > INF^{Best}$
    and $F_1 > F_1^{Best}$ **then**
    | update $INF^{Best} = INF$;
    | update $F_1^{Best} = F_1$;
    | update $[\gamma^{Best}; C^{Best}]$;
else if $(INF - INF^{Best}) > 2 \times (F_1^{Best} - F_1) > 0$
    or $(F_1 - F_1^{Best}) > 2 \times (INF^{Best} - INF) > 0$ **then**
    | update $INF^{Best} = INF$;
    | update $F_1^{Best} = F_1$;
    | update $[\gamma^{Best}; C^{Best}]$;

Figure 5.12: Performance metrics criteria.

---

respective D_{circle} value. Thus, the proposed segmentation approach requires little user calibration and is independent of image size.

Table 5.4: Results after the segmentation step for each MP stage.

	True Positives	False Positives	False Negatives
Trophozoites	811	13,701	60
Schizonts	106	5733	1
Gametocytes	149	4190	0

Illustrative examples of false negatives can be consulted in Figure 5.13, where the apparent unfocus observable on several of those annotated regions can potentially explain the segmentation procedure failure. However, this does not necessarily mean that the respective entire image of those annotations was globally unfocused, since it is not possible to obtain images with maximal focus in the whole optical circle area due to the lens constraints of μSmartScope [52].

On the other hand, examples of candidates correctly segmented and labeled as MPs can be seen in Figure 5.4. At this stage, we opted to tune the adjustable segmentation and filtering parameters to catch most of the ground truth annotations, being aware that this option would certainly increase the number of false positives. Our strategy consisted of tackling the class-imbalanced problem later in the classification step, by using the previously described data augmentation and SVM hyperparameters' selection procedures.

The classification results are presented in terms of five metrics: (1) sensitivity (SE), i.e., the percentage of candidates correctly classified as MPs; (2) specificity (SP), i.e., the percentage of candidates correctly classified as non-MPs; (3) accuracy (AC), i.e., the percentage of candidates correctly classified overall; (4) informedness (INF), i.e., the arithmetic mean between sensitivity and specificity; and (5) F_1 score (F_1), i.e., the harmonic mean between sensitivity and precision. In
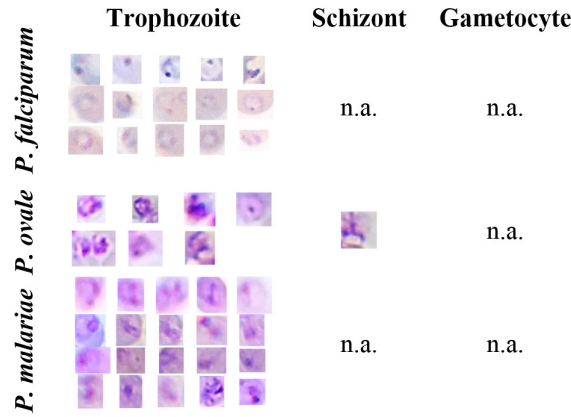
Figure 5.13: Examples of false negatives' candidates for different species and life stages after segmentation and filtering.

Table 5.5 are detailed the results after machine learning classification for the different species-stage combinations.

Table 5.5: Results after machine learning classification for each species-stage combination.

	SVM Parameters	Sensitivity	Specificity	Informedness	F_1 Score	Accuracy
P. falciparum **Trophozoites**	$\gamma = 5.46^{-2}$ $C = 2.00^{-3}$	73.9%	97.0%	70.9%	60.0%	96.1%
P. falciparum **Gametocytes**	$\gamma = 1.01^{-1}$ $C = 1$	94.8%	99.3%	94.1%	87.4%	99.2%
P. ovale **Trophozoites**	$\gamma = 1.31^{-5}$ $C = 1.01^{-3}$	84.6%	97.0%	81.6%	34.8%	96.9%
P. ovale **Schizonts**	$\gamma = 4.45^{-2}$ $C = 1.55$	82.7%	97.9%	80.6%	52.6%	97.7%
P. ovale **Gametocytes**	$\gamma = 1.08^{-1}$ $C = 1$	96.2%	99.0%	95.2%	77.1%	99.0%
P. malariae **Trophozoites**	$\gamma = 3.17^{-2}$ $C = 1$	82.0%	99.1%	81.1%	63.5%	98.9%
P. malariae **Schizonts**	$\gamma = 2.97^{-2}$ $C = 1$	87.8%	96.5%	84.3%	25.9%	96.5%
P. malariae **Gametocytes**	$\gamma = 6.33^{-2}$ $C = 8.13^{-5}$	94.9%	92.6%	87.5%	18.8%	92.6%

Considering our class-imbalanced data context, not only the acceptable performances obtained, but also a clear consistency and balance between SE, SP and AC values for the different species-stages combinations should be highlighted, which is a direct result of the implemented SVM classifier training involving data augmentation and a customized SVM hyperparameters' selection procedure. The importance of using a performance metrics criterion that merges the INF and F_1 metrics is illustrated in the heat maps of Figure 5.14. Firstly, it is noticeable that the $[\gamma; C]$ regions that boost the INF metric are clearly more demarcated when compared with the best $[\gamma; C]$ regions for the F_1 metric. However, for highly class-imbalance scenarios (such as the ones depicted for

P. malariae schizonts and gametocytes), there is an accentuated decrease in the F_1 metric caused by a precision metric decrease. In other words, this is caused by the significant increase of the false positives when compared with the number of true positives. Thus, taking into account the F_1 metric in this type of scenario might be crucial for the overall performance of the classifier, since the sacrifice of the detection of a few true positives can lead to a significant decrease of the detected false positives.

(a) Informedness.   (b) F_1 score.
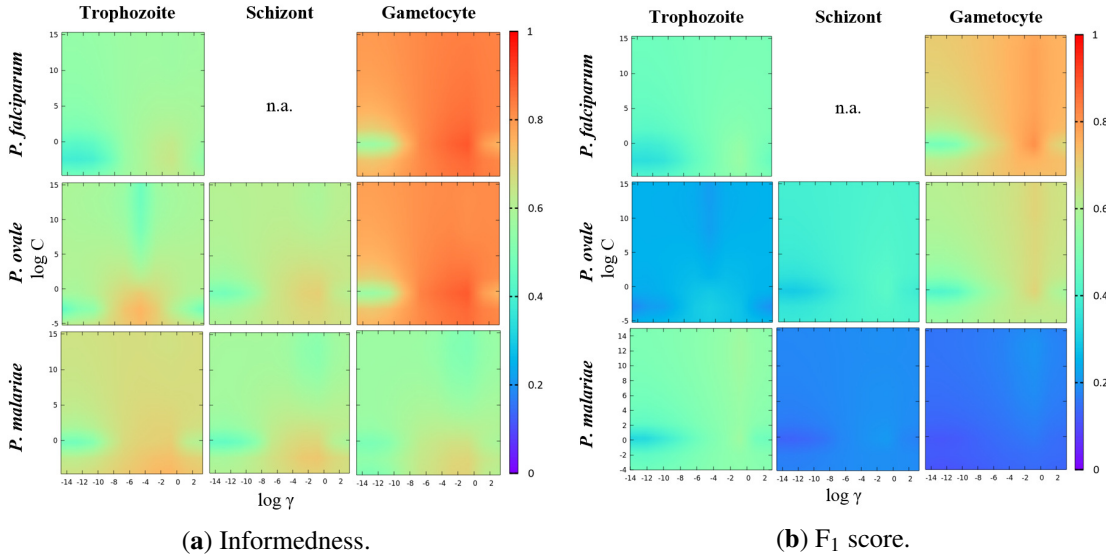
Figure 5.14: Heat maps of the SVM parameters' selection process for each species-stage combination.

It is worth mentioning that the reported classification performance has the potential to become more robust if the known limitations of the current version of the mThinMPs database are addressed, namely the imbalanced number of manual annotations for the different species-stage combinations and the lack of *P. vivax* examples.

Classification Models' Workflow

In order to allow the detection of multiple species-stage combinations in a single image, we had to design a single processing flow that connects the generated machine learning classification models. A diagrammatic representation of the process is illustrated in Figure 5.15.

In terms of overall performance by life cycle stage, the best detection results are achieved for gametocytes, being simultaneously the stage with bigger MPs structures. Thus, the designed workflow starts with the execution of the gametocytes module, with all of the candidates classified as gametocytes added to the output image. In order to avoid the classification of the same structure (or parts of it) as belonging to different species-stage combinations, the gametocytes mask is used to filter the candidates segmented in the schizonts module, i.e., if the overlap coefficient between a classified gametocyte structure and a schizont candidate is higher than 0.75, that schizont candidate is discarded. A similar procedure is applied to the trophozoites module, where the trophozoites

candidates are filtered using the structures classified as schizonts and gametocytes. In the event of a particular structure being classified as positive for different species under the same life cycle stage, the distance to the separating hyperplane is used as the tie-breaking criterion, i.e., we select the species that is further apart from the decision boundary.

(a)   (b)
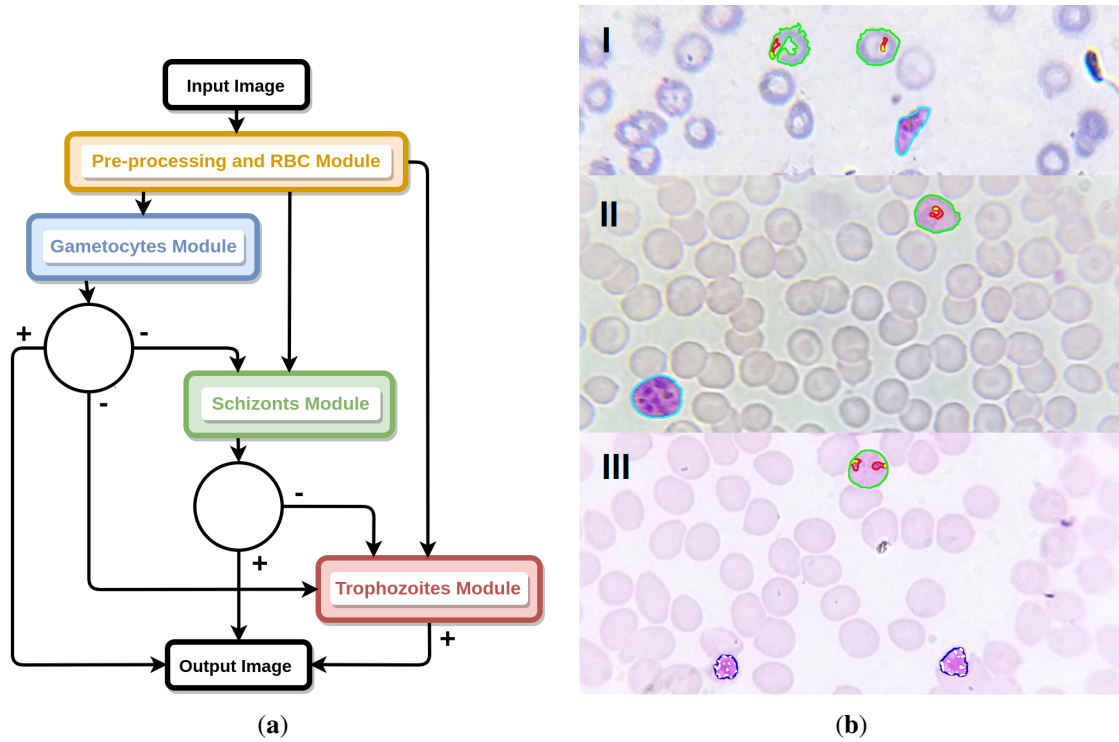
Figure 5.15: Classification models workflow. (**a**) Diagram of the classifier models workflow for the detection of multiple species-stage combinations in a single image. (**b**) Illustrative examples with detection of: (I) *P. falciparum* trophozoites and gametocyte; (II) *P. ovale* trophozoite and gametocyte; (III) *P. malariae* trophozoites and schizonts.

    The proposed methodology was implemented in C++ using the Open Source Computer Vision (OpenCV) library Version 3.2.0 [7]. In terms of performance, the registered average computational time for the classification of the 566 images included in the mThinMPs image database was 16 s per image, running on an Intel® Core™ i7-4790 CPU with 3.60 GHz (with OS Ubuntu 14.04 LTS). Moreover, the memory allocation of the proposed methodology was also analyzed using the Valgrind profiling tool, with maximum memory peaks detected always below 240 MB for the images used in this study. It should be noted that the obtained computational times and memory allocations can be considered suitable for scenarios where access to similar or better computational resources is available (including via cloud computing). On the other hand, considering the current reality of malaria-endemic rural areas, the execution of the developed image processing module exclusively on mobile devices is also currently being considered by our group. However, given the (still) comparably lower computational resources of these devices, code optimizations will certainly be required in order to obtain comparable processing times.

5.7   Conclusions and Future Work

In this work, an image processing methodology using supervised classification to analyze microscopic images of malaria-infected thin blood smears is presented. Particularly, the proposed approach assesses the presence of MPs and determines the species and life cycle stage. One of the main contributions of this work is the usage of images acquired exclusively with smartphones, with the consequent customization of the proposed methodology for images with such characteristics. This differentiation factor is directly related with its integration in a mobile-based framework currently being developed, which aims to support the pre-diagnosis of malaria in rural areas.

Given the lack of freely available image datasets, a new mobile thin smear malaria parasites (mThinMPs) image database was specifically created and used in this study. By comparing the results obtained with manual annotations of a microscopy specialist, we validated the performance and robustness of the proposed methodology to detect eight different species-stage combinations, with an automatic detection performance ranging 73.9–96.2% in terms of sensitivity and 92.6–99.3% in terms of specificity. These promising results attest to the potential of using this approach as a valid alternative to conventional microscopy examination, with comparable detection performances and acceptable computational times.

To achieve these results, the importance of a newly-proposed performance metrics criterion for SVM hyperparameters' selection should be highlighted, which merges the informedness and F_1 score metrics. Moreover, we also took into consideration the importance of providing detailed visual outputs, so another innovative aspect of this work is the identification of relevant inner structures of MPs like chromatin dots and merozoites, since we consider that useful and easily interpretable outputs are of extreme importance in the acceptance and dissemination of computer-aided diagnosis systems.

As future work, we aim to complement the mThinMPs image database with more annotations, namely: (i) add illustrative cases of *P. vivax* in all three growing stages; and (ii) increase the number of examples for the already considered species-stages combinations, with special focus on those less represented (e.g., *P. malariae* schizonts and gametocytes). The extended mThinMPs database is envisioned to support the future improvements of the proposed methodology in terms of detection performance and robustness. As a final note, this work represents only a component of a mobile-based framework for MPs' detection currently being developed. Thus, we aim to integrate this methodology into the referenced framework, with the ultimate goal of creating a system that: (i) provides an effective pre-diagnosis of malaria in medically-underserved areas; (ii) is low cost and mobile based; (iii) is easy to use, even for non-experts in microscopy.

Part III

Conclusion

Chapter 6

Conclusions and Future Work

This final chapter summarizes the main conclusions achieved as a result of the scientific contributions presented throughout this document, as well as a description of several research topics that emerged from the work done and can be pursued in future work.

6.1   Conclusions

We following present the conclusions for each research topic explored in the ambit of this thesis:

- **Fundamentals of Computer-aided Malaria Parasites Detection**: In this chapter, various image processing and analysis approaches already proposed on the literature for the detection and segmentation of malaria parasites in blood smear microscopic images were collected and reviewed. This state-of-the-art review allowed to conclude that malaria parasites detection and segmentation techniques in microscopic images are, in general, still in need of improvement and further testing. Despite the reported promising results, the great majority of the proposed computer-aided methods are based on images acquired under well controlled conditions and with proper microscopic equipment. Taking into account that 80% of malaria cases occur in Africa, where this type of equipment is scarce or even nonexistent in common healthcare facilities, the development of new microscopic devices (and ideally low cost) is an area that can greatly improve the chances of the successful deployment of computer vision CAD solutions for malaria diagnosis in the field.

  Additionally, the recent significant improvements of the new generation of mobile devices in terms of image acquisition and processing power can play a key role in future malaria control strategies. In fact, the mobile phone is currently Africa's most important digital technology, and if a reliable automatic diagnostic performance is ensured through the usage of those devices, one would dramatically reduce the effort in the exhaustive and time consuming activity of microscopic examination.

- μ**SmartScope: Towards a Fully Automated 3D-printed Smartphone Microscope with Motorized Stage**: In this chapter we reported our most recent advances towards the development of a fully automated 3D-printed smartphone microscope with a motorized stage (μSmartScope). This prototype is the first proposed smartphone-based alternative to conventional microscopy that allows autonomous acquisition of a pre-defined number of images at 1000x magnification with suitable resolution, by using a motorized automated stage fully powered and controlled by a smartphone, without any human interaction.

  All the components of the proposed device are described and properly evaluated. In terms of the optical module, a minimum resolution of 0.388 μm was determined, with a FOV of 214.38 μm and 206.87 μm for the vertical and horizontal axis that passes through the center of the visible optical circle, respectively. Regarding the illumination module, the LED light coupled to the proposed condenser demonstrated to achieve an uniform illumination suitable for brightfield microscopy. The developed motorized automated stage (μStage) achieved an average resolution of 330 ± 81 μm for the XY plane steps and an average resolution of 0.763 ± 0.098 μm for the Z-axis steps, results that validates its effective usage for microscopy analysis. Moreover, the proposed automated focus approach was evaluated on 9 different blood smears and 5 different smartphone models, achieving an average performance time of 8.31 ± 1.41 and 12.98 ± 4.20 seconds per image, for thin and thick blood smears, respectively.

  Several smears infected by different blood parasites responsible for the most relevant neglected tropical diseases were used to test the device. The acquired images showed that it was possible to detect those agents through images acquired via the μSmartScope, which clearly illustrate the huge potential of this device, specially in developing countries with limited access to healthcare services.

- **Automated Detection of Malaria Parasites on Thick Blood Smears via Mobile Devices**: In this chapter, a methodology to assess the presence of *P.falciparum* trophozoites and WBCs in Giemsa stained thick blood smears was presented. The great majority of the proposed methodologies to date are based on images acquired under well controlled conditions and with proper microscopic equipment, so the main differential factor of this work is the usage of microscopic images exclusively acquired with smartphones coupled to a low cost optical magnification device, as well as the consequent customization of the proposed methodology for images with such characteristics. Given the lack of freely available image datasets, a mobile acquired image dataset manually annotated by a specialist was specifically created and used in this study. Moreover, a wide variety of image features were used to characterize the candidates in terms of geometry, texture and color, merging significant features referred on previous works, with some never used before for this purpose. In terms of results, the automatic detection of WBCs in thick blood smears achieved 98.2% of sensitivity and 72.1% specificity, while the *P.falciparum* trophozoites detection achieved a sensitivity of 80.5% and a specificity of 93.8%.

- **Mobile-Based Analysis of Malaria-Infected Thin Blood Smears: Automated Species and Life Cycle Stage Determination**: In this chapter we presented an image processing methodology using supervised classification to analyze microscopic images of malaria-infected thin blood smears. Particularly, the proposed approach assesses the presence of malaria parasites and determines the species and life cycle stage. One of the main contributions of this work is the usage of images acquired exclusively with smartphones, with the consequent customization of the proposed methodology for images with such characteristics. This differentiation factor is directly related with its integration in a mobile-based framework currently being developed, which aims to support the pre-diagnosis of malaria in rural areas.

  Given the lack of freely available image datasets, a new mobile thin smear malaria parasites (mThinMPs) image database was specifically created and used in this study. By comparing the results obtained with manual annotations of a microscopy specialist, we validated the performance and robustness of the proposed methodology to detect eight different species-stage combinations, with an automatic detection performance ranging 73.9–96.2% in terms of sensitivity and 92.6–99.3% in terms of specificity. These promising results attest to the potential of using this approach as a valid alternative to conventional microscopy examination, with comparable detection performances and acceptable computational times.

  To achieve these results, the importance of a newly-proposed performance metrics criterion for SVM hyperparameters' selection should be highlighted, which merges the informedness and F_1 score metrics. Moreover, we also took into consideration the importance of providing detailed visual outputs, so another innovative aspect of this work is the identification of relevant inner structures of malaria parasites like chromatin dots and merozoites, since we consider that useful and easily interpretable outputs are of extreme importance in the acceptance and dissemination of computer-aided diagnosis systems.

6.2 Future Work

In this section we detail several research topics that emerged from the work done and can be pursued in the future:

- **Automated Smartphone Microscope**: Regarding this research topic, we are planning to test in the near future the developed automated smartphone microscope (termed μSmartScope) on field trials, in order to assess its performance and practical usefulness. Particularly, the μSmartScope will represent a component of a mobile-based framework for malaria parasites detection currently being developed. Thus, we aim to integrate this prototype into the referred framework, with the ultimate goal of creating a system that: (i) provides an effective pre-diagnosis of malaria in medically-underserved areas; (ii) is low cost and mobile based; (iii) is easy to use, even for non-experts in microscopy.

- **Automatic Detection of Malaria Parasites in Thick and Thin Blood Smears**: Also aligned with the field trials of the mobile-based framework described above, we aim to leverage this initiative to assess and improve the performance of our image processing and machine-learning modules. Not only we will take this opportunity to test the current version of the proposed methodologies, but also to improve its performance through the blood smears being collected during the field trials. The training image datasets of each module could then be complemented with more annotated data. For instance, in terms of the mThinMPs image database, we aim to: (i) add illustrative cases of *P. vivax* in all three growing stages; and (ii) increase the number of examples for the already considered species-stages combinations, with special focus on those less represented (e.g., *P. malariae* schizonts and gametocytes).

  In addition, we envision that the collection of significantly larger datasets will also open doors for the exploration of different machine-learning strategies. Particularly, major breakthroughs in the area of computer vision have been recently reported through the usage of deep learning approaches based on artificial neural networks algorithms, most of them for scenarios where big data is available. Therefore, we aim to access the potential of these emergent AI approaches, with the final goal of obtaining classification models for malaria parasites detection that are not only robust and reliable, but also transparent and easily interpretable for humans.

  It should be noted that, despite the increasing interest in AI-powered solutions, its usage in real environments still poses highly relevant ethical questions and concerns. Thus, in the future we intend to improve the capability of our solution to explain what triggered a particular decision, since we firmly believe that this type of self-explanatory behavior will play a key role in the user's trust on systems with intelligent behavior, and consequently on the widespread acceptance of our mobile-based framework.

As a final note, new research topics have also emerged from the work done, namely the development of similar mobile-based frameworks that supports the diagnosis of other neglected tropical diseases. In that scenario, malaria diagnosis might be just one element of a suite of diagnostic software tests running on this type of solution, and the automated detection of other hemoparasites like *Brugia malayi* or *Trypanosome cruzi* could then be performed in parallel, using the same microscopic image.

References

[1] Nasir Abdul, Salihah Aimi, Mohd Yusoff Mashor, and Zeehaida Mohamedq. Parasite detection and identification for automated thin blood film malaria diagnosis. *WSEAS Transactions on Biology & Biomedicine*, 10(1):41–55, 2013.

[2] David W. Aha, Dennis Kibler, and Marc K. Albert. Instance-Based Learning Algorithms. *Mach. Learn.*, 6(1):37–66, January 1991.

[3] E. Alpaydin and F. Bach. *Introduction to Machine Learning*. MIT Press, 2014.

[4] D. Anggraini, A.S. Nugroho, C. Pratama, I.E. Rozi, V. Pragesjvara, and M. Gunawan. Automated status identification of microscopic images obtained from malaria thin blood smears using bayes decision: A study case in plasmodium falciparum. In *2011 International Conference on Advanced Computer Science and Information System (ICACSIS)*, pages 347–352, December 2011.

[5] Aydin Arpa, Gordon Wetzstein, Douglas Lanman, and Ramesh Raskar. Single lens off-chip cellphone microscopy. pages 23–28. IEEE, June 2012.

[6] Blycroft Publishing. Africa & Middle East Mobile Factbook 2q 2014, 2014.

[7] G. Bradski. The OpenCV Library. *Dr. Dobb's Journal of Software Tools*, 2000.

[8] Richard G. Budynas and Keith J. Nisbett. *Shigley's Mechanical Engineering Design*. McGraw-Hill Education, New York, NY, 10 edition edition, January 2014.

[9] CDC. Centers for Disease Control and Prevention. http://www.cdc.gov. Accessed: 2016-03-12.

[10] CDC. Centers for Disease Control and Prevention | Malaria Diagnosis (U.S.) – Rapid Diagnostic Test. https://www.cdc.gov/malaria/diagnosis_treatment/rdt. Accessed: 2017-07-17.

[11] Chih-Chung Chang and Chih-Jen Lin. LIBSVM: A library for support vector machines. *ACM Transactions on Intelligent Systems and Technology*, 2:27:1–27:27, 2011.

[12] Y. Q. Chen, M. S. Nixon, and D. W. Thomas. Statistical Geometric Features for Texture Classification. *Pattern Recognition*, 28(4):537, 1995.

[13] James M. Crutcher and Stephen L. Hoffman. Malaria. In Samuel Baron, editor, *Medical Microbiology*. University of Texas Medical Branch at Galveston, Galveston (TX), 4th edition, 1996.

[14] James S. Cybulski, James Clements, and Manu Prakash. Foldscope: Origami-Based Paper Microscope. *PLoS ONE*, 9(6):e98781, June 2014.

[15] Sanmay Das. Filters, Wrappers and a Boosting-Based Hybrid for Feature Selection. In *Proceedings of the Eighteenth International Conference on Machine Learning*, ICML '01, pages 74–81, San Francisco, CA, USA, 2001. Morgan Kaufmann Publishers Inc.

[16] E. Dolgin. Portable pathology for Africa. *IEEE Spectrum*, 52(1):37–39, January 2015.

[17] Matthias Elter, Erik Hasslmeyer, and Thorsten Zerfass. Detection of malaria parasites in thick blood films. *Annual International Conference of the IEEE Engineering in Medicine and Biology Society*, 2011:5140–5144, 2011.

[18] Yochay Eshel, Arnon Houri-Yafin, Hagai Benkuzari, Natalie Lezmy, Mamta Soni, Malini Charles, Jayanthi Swaminathan, Hilda Solomon, Pavithra Sampathkumar, Zul Premji, Caroline Mbithi, Zaitun Nneka, Simon Onsongo, Daniel Maina, Sarah Levy-Schreier, Caitlin Lee Cohen, Dan Gluck, Joseph Joel Pollak, and Seth J. Salpeter. Evaluation of the parasight platform for malaria diagnosis. *J Clin Microbiol*, 55(3):768–775, Mar 2017.

[19] Y. Fang, W. Xiong, W. Lin, and Z. Chen. Unsupervised malaria parasite detection based on phase spectrum. In *2011 Annual International Conference of the IEEE Engineering in Medicine and Biology Society*, pages 7997–8000, Aug 2011.

[20] G. Victo Sudha George and V. Cyril Raj. Review on Feature Selection Techniques and the Impact of SVM for Cancer Classification using Gene Expression Profile. *CoRR*, abs/1109.1062, 2011.

[21] Pierre Geurts, Damien Ernst, and Louis Wehenkel. Extremely randomized trees. *Machine Learning*, 63(1):3–42, April 2006.

[22] M. Ghosh, D. Das, C. Chakraborty, and A.K. Ray. Plasmodium vivax segmentation using modified fuzzy divergence. In *2011 International Conference on Image Information Processing (ICIIP)*, pages 1–5, November 2011.

[23] N. S M M Hanif, M.Y. Mashor, and Z. Mohamed. Image enhancement and segmentation using dark stretching technique for Plasmodium Falciparum for thick blood smear. In *2011 IEEE 7th International Colloquium on Signal Processing and its Applications (CSPA)*, pages 257–260, March 2011.

[24] R.M. Haralick, K. Shanmugam, and Its'Hak Dinstein. Textural Features for Image Classification. *IEEE Transactions on Systems, Man and Cybernetics*, SMC-3(6):610–621, November 1973.

[25] T. Hastie, R. Tibshirani, and J. Friedman. *The Elements of Statistical Learning: Data Mining, Inference, and Prediction*. Springer Series in Statistics. Springer New York, 2013.

[26] Ming-Kuei Hu. Visual pattern recognition by moment invariants. *IRE Transactions on Information Theory*, 8(2):179–187, February 1962.

[27] X. Jiang. Feature extraction for image recognition and computer vision. In *2nd IEEE International Conference on Computer Science and Information Technology, 2009. ICCSIT 2009*, pages 1–15, August 2009.

[28] George H. John and Pat Langley. Estimating Continuous Distributions in Bayesian Classifiers. In *Proceedings of the Eleventh Conference on Uncertainty in Artificial Intelligence*, UAI'95, pages 338–345, San Francisco, CA, USA, 1995. Morgan Kaufmann Publishers Inc.

[29] S. Kaewkamnerd, A. Intarapanich, M. Pannarat, S. Chaotheing, C. Uthaipibull, and S. Tongsima. Detection and classification device for malaria parasites in thick-blood films. In *2011 IEEE 6th International Conference on Intelligent Data Acquisition and Advanced Computing Systems (IDAACS)*, volume 1, pages 435–438, September 2011.

[30] S. Kareem, I. Kale, and R. C S Morling. Automated P.falciparum Detection System for Post-Treatment Malaria Diagnosis Using Modified Annular Ring Ratio Method. In *2012 UKSim 14th International Conference on Computer Modelling and Simulation (UKSim)*, pages 432–436, March 2012.

[31] S. Kareem, R. C S Morling, and I. Kale. A novel method to count the red blood cells in thin blood films. In *2011 IEEE International Symposium on Circuits and Systems (ISCAS)*, pages 1021–1024, May 2011.

[32] N.A. Khan, H. Pervaz, A.K. Latif, A. Musharraf, and Saniya. Unsupervised identification of malaria parasites using computer vision. In *11th International Joint Conference on Computer Science and Software Engineering (JCSSE)*, pages 263–267, May 2014.

[33] A. Khotanzad and Yaw Hua Hong. Invariant image recognition by Zernike moments. *IEEE Transactions on Pattern Analysis and Machine Intelligence*, 12(5):489–497, May 1990.

[34] V.A. Kovalev, A.Y. Grigoriev, and Hyo-Sok Ahn. Robust recognition of white blood cell images. In *, Proceedings of the 13th International Conference on Pattern Recognition, 1996*, volume 4, pages 371–375 vol.4, August 1996.

[35] Eric Krotkov. Focusing. *International Journal of Computer Vision*, 1(3):223–237, 1988.

[36] XY Liu, WH Wang, and Y Sun. Dynamic evaluation of autofocusing for automated microscopic analysis of blood smear and pap smear. *Journal of microscopy*, 227(1):15–23, 2007.

[37] V.V. Makkapati and R.M. Rao. Segmentation of malaria parasites in peripheral blood smear images. In *IEEE International Conference on Acoustics, Speech and Signal Processing, 2009. ICASSP 2009*, pages 1361–1364, April 2009.

[38] L. Malihi, K. Ansari-Asl, and A. Behbahani. Malaria parasite detection in giemsa-stained blood cell images. In *2013 8th Iranian Conference on Machine Vision and Image Processing (MVIP)*, pages 360–365, September 2013.

[39] S. Mandal, A. Kumar, J. Chatterjee, M. Manjunatha, and A.K. Ray. Segmentation of blood smear images using normalized cuts for detection of malarial parasites. In *2010 Annual IEEE India Conference (INDICON)*, pages 1–4, December 2010.

[40] C. Mehanian, M. Jaiswal, C. Delahunt, C. Thompson, M. Horning, L. Hu, S. McGuire, T. Ostbye, M. Mehanian, B. Wilson, C. Champlin, E. Long, S. Proux, D. Gamboa, P. Chiodini, J. Carter, M. Dhorda, D. Isaboke, B. Ogutu, W. Oyibo, E. Villasis, K. M. Tun, C. Bachman, and D. Bell. Computer-automated malaria diagnosis and quantitation using convolutional neural networks. In *2017 IEEE International Conference on Computer Vision Workshops (ICCVW)*, pages 116–125, Oct 2017.

[41] Motic. EasyScan Go | Optically Intelligent Disease Scanning. http://www.easyscango.com. Accessed: 2018-04-21.

[42] T.Z.T. Muda and R.A. Salam. Blood cell image segmentation using hybrid K-means and median-cut algorithms. In *2011 IEEE International Conference on Control System, Computing and Engineering (ICCSCE)*, pages 237–243, November 2011.

[43] A. Nanoti, S. Jain, C. Gupta, and G. Vyas. Detection of malaria parasite species and life cycle stages using microscopic images of thin blood smear. In *2016 International Conference on Inventive Computation Technologies (ICICT)*, volume 1, pages 1–6, Aug 2016.

[44] H. A. Nugroho, S. A. Akbar, and E. E. H. Murhandarwati. Feature extraction and classification for detection malaria parasites in thin blood smear. In *2015 2nd International Conference on Information Technology, Computer, and Electrical Engineering (ICITACEE)*, pages 197–201, October 2015.

[45] Casey W. Pirnstill and Gerard L. Coté. Malaria Diagnosis Using a Mobile Phone Polarized Microscope. *Scientific Reports*, 5:13368, August 2015.

[46] I.K.E. Purnama, F.Z. Rahmanti, and M.H. Purnomo. Malaria parasite identification on thick blood film using genetic programming. In *3rd International Conference on Instrumentation, Communications, Information Technology, and Biomedical Engineering*, pages 194–198, November 2013.

[47] John Quinn, Alfred Andama, Ian Munabi, and Fred Kiwanuka. Automated Blood Smear Analysis for Mobile Malaria Diagnosis. In *Mobile Point-of-Care Monitors and Diagnostic Device Design*, Devices, Circuits, and Systems, pages 115–132. 2014.

[48] CTI Reviews. *Smart Data , Enterprise Performance Optimization Strategy*. Cram101, 2016.

[49] Luís Rosado, José M. Correia da Costa, Dirk Elias, and Jaime S. Cardoso. A review of automatic malaria parasites detection and segmentation in microscopic images. *Anti-Infective Agents*, 14(1):11–22, 2016.

[50] Luís Rosado, José M. Correia da Costa, Dirk Elias, and Jaime S. Cardoso. Automated Detection of Malaria Parasites on Thick Blood Smears via Mobile Devices. *Procedia Computer Science*, 90:138–144, January 2016.

[51] Luís Rosado, José M. Correia da Costa, Dirk Elias, and Jaime S. Cardoso. Mobile-based analysis of malaria-infected thin blood smears: Automated species and life cycle stage determination. *Sensors*, 17(10), 2017.

[52] Luís Rosado, João Oliveira, Maria João M. Vasconcelos, José M. Correia da Costa, Dirk Elias, and Jaime S. Cardoso. μSmartScope: 3d-printed smartphone microscope with motorized automated stage. In *Proceedings of the 10th International Joint Conference on Biomedical Engineering Systems and Technologies - Volume 1: BIODEVICES, (BIOSTEC 2017)*, pages 38–48. INSTICC, SciTePress, 2017.

[53] Luís Rosado, Paulo T. Silva, José Faria, João Oliveira, Maria João M. Vasconcelos, José M. Correia da Costa, Dirk Elias, and Jaime S. Cardoso. μSmartScope: Towards a fully automated 3d-printed smartphone microscope with motorized stage. *Communications in Computer and Information Science Book Series*, 881, 2018.

[54] Loren Shih. Autofocus survey: a comparison of algorithms. In *Electronic Imaging 2007*, pages 65020B–65020B. International Society for Optics and Photonics, 2007.

[55] Balbir Singh and Cyrus Daneshvar. Human Infections and Detection of Plasmodium knowlesi. *Clinical Microbiology Reviews*, 26(2):165–184, April 2013.

[56] Zachary J. Smith, Kaiqin Chu, Alyssa R. Espenson, Mehdi Rahimzadeh, Amy Gryshuk, Marco Molinaro, Denis M. Dwyre, Stephen Lane, Dennis Matthews, and Sebastian Wachsmann-Hogiu. Cell-Phone-Based Platform for Biomedical Device Development and Education Applications. *PLoS ONE*, 6(3):e17150, March 2011.

[57] Yu Sun, Stefan Duthaler, and Bradley J Nelson. Autofocusing algorithm selection in computer microscopy. In *2005 IEEE/RSJ International Conference on Intelligent Robots and Systems*, pages 70–76. IEEE, 2005.

[58] Colin J. Sutherland, Naowarat Tanomsing, Debbie Nolder, Mary Oguike, Charlie Jennison, Sasithon Pukrittayakamee, Christiane Dolecek, Tran Tinh Hien, Virgilio E. do Rosário, Ana Paula Arez, João Pinto, Pascal Michon, Ananias A. Escalante, Francois Nosten, Martina Burke, Rogan Lee, Marie Blaze, Thomas Dan Otto, John W. Barnwell, Arnab Pain, John Williams, Nicholas J. White, Nicholas P. J. Day, Georges Snounou, Peter J. Lockhart, Peter L. Chiodini, Mallika Imwong, and Spencer D. Polley. Two Nonrecombining Sympatric Forms of the Human Malaria Parasite Plasmodium ovale Occur Globally. *Journal of Infectious Diseases*, 201(10):1544–1550, May 2010.

[59] Neil A. Switz, Michael V. D'Ambrosio, and Daniel A. Fletcher. Low-Cost Mobile Phone Microscopy with a Reversed Mobile Phone Camera Lens. *PLoS ONE*, 9(5):e95330, May 2014.

[60] F. Boray Tek, Andrew G. Dempster, and Izzet Kale. *Malaria Parasite Detection in Peripheral Blood Images*. 2006.

[61] F. Boray Tek, Andrew G. Dempster, and İzzet Kale. Parasite detection and identification for automated thin blood film malaria diagnosis. *Computer Vision and Image Understanding*, 114(1):21–32, January 2010.

[62] Jay Martin Tenenbaum. Accommodation in computer vision. phd dissertation. Technical report, DTIC Document, 1970.

[63] The END Fund. NTD Overview. http://www.end.org/whatwedo/ntdoverview. Accessed: 2017-09-11.

[64] Derek Tseng, Onur Mudanyali, Cetin Oztoprak, Serhan O. Isikman, Ikbal Sencan, Oguzhan Yaglidere, and Aydogan Ozcan. Lensfree microscopy on a cellphone. *Lab on a Chip*, 10(14):1787–1792, July 2010.

[65] S E Umbaugh, Y Wei, and M Zuke. Feature extraction in image analysis. A program for facilitating data reduction in medical image classification. *IEEE engineering in medicine and biology magazine: the quarterly magazine of the Engineering in Medicine & Biology Society*, 16(4):62–73, August 1997.

[66] Michael Unser. Sum and Difference Histograms for Texture Classification. *IEEE Transactions on Pattern Analysis and Machine Intelligence*, PAMI-8(1):118–125, January 1986.

[67] Jürg Utzinger, Sören L. Becker, Stefanie Knopp, Johannes Blum, Andreas L. Neumayr, Jennifer Keiser, and Christoph F. Hatz. Neglected tropical diseases: diagnosis, clinical management, treatment and control. *Swiss Medical Weekly*, 142, 2012.

[68] Mike Wakerly. Usb serial for android, 2012.

[69] L. Wang, G. Liu, and Q. Dai. Optimization of Segmentation Algorithms Through Mean-Shift Filtering Preprocessing. *IEEE Geoscience and Remote Sensing Letters*, 11(3):622–626, March 2014.

[70] WHO. *Basic malaria microscopy*. Number Part 1. World Health Organization, 1991.

[71] WHO. World Health Organization | Basic malaria microscopy: Part II. Tutor's guide. Second edition, 2010.

[72] WHO. World Health Organization | World Malaria Report 2013, 2013.

[73] WHO. World Health Organization | World Malaria Report 2015, 2015.

[74] WHO. World Health Organization | World Malaria Report 2016, 2016.

[75] Qiang Wu, Fatima Aziz Merchant, and Kenneth R Castleman. *Microscope image processing*. Elsevier/Academic Press, Amsterdam; Boston, 2008.

[76] Dahou Yang, Gowtham Subramanian, Jinming Duan, Shaobing Gao, Li Bai, Rajesh Chandramohanadas, and Ye Ai. A portable image-based cytometer for rapid malaria detection and quantification. *PLOS ONE*, 12(6):1–18, 06 2017.

[77] I. T. Young, P. W. Verbeek, and B. H. Mayall. Characterization of chromatin distribution in cell nuclei. *Cytometry*, 7(5):467–474, September 1986.

[78] Leonardo Yunda, Andrés Alarcón, and Jorge Millán. Metodo automatizado de analisis de imagenes para deteccion del parasito de la malaria p-vivax en imagenes de gota gruesa. *Sistemas & Telematica*, 10(20):9–25, March 2012.

[79] G.P. Zachary. Technology alone won't improve health in Africa [Spectral lines]. *IEEE Spectrum*, 52(1):7–7, January 2015.

[80] Li-hui Zou, Jie Chen, Juan Zhang, and N. Garcia. Malaria Cell Counting Diagnosis within Large Field of View. In *2010 International Conference on Digital Image Computing: Techniques and Applications (DICTA)*, pages 172–177, December 2010.